Resonant Photonic Structures for Control of Light-Matter Interaction in Semiconductor Nanostructures

by

David Goldberg

A dissertation submitted to the Graduate Faculty in Physics
in partial fulfillment of the requirements for the degree of
Doctor of Philosophy, The City University of New York

2012

Resonant Photonic Structures for Control of Light-Matter Interaction in Semiconductor Nanostructures

This manuscript has been read and accepted for the Graduate Faculty in Physics in satisfaction of the dissertation proposal requirements for the degree of Doctor of Philosophy.

Professor Vinod M. Menon

Date

Chair of Examining Committee

Professor Steven Greenbaum

Date

Executive Officer

Professor Alexander A. Lisyansky

Professor Lev I. Deych

Professor Azriel Z. Genack

Supervisory Committee

THE CITY UNIVERSITY OF NEW YORK

Abstract

Resonant Photonic Structures for Control of Light-Matter Interaction in Semiconductor Nanostructures

by

David Goldberg

Adviser: Professor Vinod M. Menon

In this thesis, the control of light-matter interaction in semiconductor nanostructures was investigated using resonant photonic structures. This study is categorized in two parts: collective phenomena of quantum confined excitons, and quantum dots in microcavity structures.

The collective behavior of excitons is studied in a resonant multiple-quantum-well structure. In this system, the quantum-wells are separated by barrier layers such that the distance between excitons of neighboring quantum-wells is half of their resonant wavelength ($\lambda/2$), the so-called Bragg condition. The Bloch modes of the background photonic crystal introduced by the refractive index contrast between the well and barrier layers interact coherently with the ensemble of excitons forming Bloch-polaritons. These Bloch-polaritons are characterized by low-temperature angle resolved spectroscopic measurements. Large changes in reflectance are observed in response to an externally applied electric field due to the system transition between strong and weak coupling regimes.

In addition, a system of colloidal quantum-dot clusters were investigated for evidence of superradiant emission by means of time-resolved and steady state photoluminescence spectroscopy.

Microcavities incorporating quantum dots in the cavity layer were investigated under low, and high concentration regimes. With low concentrations of quantum dots, spectroscopic measurements reveal the quantum dots emit through the cavity resonance, and power dependent studies show the emission intensity has a linear

dependence on pumping fluence, with no reduction in linewidth, resulting from the system being below the gain threshold. However, a similar investigation on a system with a high quantum dot concentration reveal gain occurring at the biexciton energy accompanied by highly directional emission.

Systems of coupled-cavities were also studied where features similar to electromagnetically-induced-transparency were observed from spectroscopic measurements. Under specific coupling criteria, the photon field intensity distribution of the system exhibits a *bright* and a *dark* cavity. When incorporating quantum dots in the *bright* cavity, resonant emission is observed. However, when incorporating quantum dots in the *dark* cavity, only uncoupled emission is observed.

Acknowledgments

This thesis is a compilation the work that I have accomplished over the better half of a decade. It has been a roller coaster of ups and downs – such is the nature of research. The downs outnumber the ups; however, the ups outweigh the downs. During this time I have undergone much professional as well as personal growth. To this I owe a debt of gratitude to those who have guided and assisted me along this fantastic journey.

Firstly, I would like to thank my advisor, Professor Vinod Menon. It is to him that I attribute the bulk of my scientific and experimental knowledge. He has guided me through the years with a level of openness and patience that is uncommon, to say the least. It has been a privilege to learn under his advisement, and I am grateful for the opportunity.

I must also thank Professor Alexander Lisyansky for being a constant source of advisement since my early days as an undergraduate student. I cannot count the number of times I knocked on his door and asked if he had a minute to speak with me; to which his response was, "I'll find a few". Whether or not a particular discussion was fruitful, they were all a pleasure and a privilege. It has been an honor to have the opportunity to seek out his wisdom on a regular basis.

Experimental research is often a team effort. Therefore, I must thank my labmates Saima Husaini, Harish Krishnamoorthy, and Xiaoze Liu for their continuous counsel and friendship. Saima and I have worked together since our undergraduate days. She has a knack for bringing much needed levity to difficult situations. Harish and Xiaoze have been a constant source of support where I can always depend on their skills and expertise. I consider myself privileged to have worked alongside them.

Last, but most definitely not least, I thank my wife, Gitty, who I met along this journey. I would not have been able to complete this without her encouragement, and patience. She has been a constant source of light in my life. I am grateful to be able to share my life with her.

Contents

List of Tables

List of Figures

Chapter 1

Introduction

1.1 Excitons in Semiconductor Systems

Semiconductors are loosely defined as a material with electrical conductivity in the range of $10^{-2} - 10^{9}$ Ω·cm. They are more commonly described by their electronic bandgap which ranges between $0 - 4$ eV [1]. Materials with zero energy bandgap are known as metals or semimetals.

In semiconductor material systems, electrons may be excited from the valance band to the conduction band, leaving a hole in the valance band. Under the Coulomb interaction, the motion of these two particles become correlated, resulting in a quasi-particle know as an *exciton*. There are two classes of excitons, Frenkel excitons, and Wannier-Mott excitons (or simply Wannier excitons), depending on the material system [2–5]. Frenkel excitons occur in semiconductor systems where the electron-hole

interaction is strong due to their close proximity. The exciton size is on the order of unit cell, in molecular systems. Wannier-Mott excitons occur in semiconductor systems with high dielectric constants that reduce the Coulomb interaction between the electron and the hole due to screening. Compared to Frenkel excitons, Wannier-Mott excitons have smaller binding energies, and larger size. In this work, the material systems studied have Wannier-Mott excitons; therefore, the following discussion will be limited to excitons of that type.

The time-independent Schrödinger's equation for an exciton can be written as:

$$\widehat{\mathbf{H}}\Phi(\mathbf{r_e}, \mathbf{r_h}) = E\Phi(\mathbf{r_e}, \mathbf{r_h}) \tag{1.1}$$

where the Hamiltonian operator, $\widehat{\mathbf{H}}$, in a semiconducting material with a zero-frequency dielectric constant of ε, can be written as:

$$\widehat{\mathbf{H}} = -\frac{\hat{\mathbf{p}}_\mathbf{h}^2}{2m_h} - \frac{\hat{\mathbf{p}}_\mathbf{e}^2}{2m_e} - \frac{e^2}{\varepsilon\,|\mathbf{r_e} - \mathbf{r_h}|} \tag{1.2}$$

where e is the charge of an electron, and $\hat{\mathbf{p}}_{\mathbf{e(h)}}$, $m_{e(h)}$, $\mathbf{r}_{\mathbf{e(h)}}$, are the momentum operator, mass[1] and position vector of the electron (hole).

The Hamiltonian is similar to that of the hydrogen atom; therefore, the exciton is said to be a hydrogen-like particle. By applying the center-of-mass, and relative

[1] In the case of the hole, m_h is the effective mass.

coordinate transformation:

$$\mathbf{R} = \frac{m_e \mathbf{r_e} + m_h \mathbf{r_h}}{m_e + m_h} \tag{1.3a}$$

$$\mathbf{r} = \mathbf{r_e} - \mathbf{r_h} \tag{1.3b}$$

the Schrödinger's equation in equation 1.1 transforms into two equations where the center-of-mass, and relative coordinates are decoupled:

$$-\frac{\hbar^2}{2M}\nabla^2_{\mathbf{R}}\psi(\mathbf{R}) = E_R\psi(\mathbf{R}) \tag{1.4a}$$

$$\left(-\frac{\hbar^2}{2\mu}\nabla^2_{\mathbf{r}} - \frac{e^2}{\varepsilon r}\right)\phi(\mathbf{r}) = E_r\phi(\mathbf{r}) \tag{1.4b}$$

where μ is the reduced mass defined by, $\mu^{-1} = m_e^{-1} + m_h^{-1}$. Equation 1.4a is the Schrödinger's equation for a free particle giving energies:

$$E_R = \frac{\hbar^2 k^2}{2M} \tag{1.5}$$

where k is the wave number of the exciton. Equation 1.4b leads to energy quantization giving the total exciton energy as:

$$E_n = E_{gap} + \frac{\hbar^2 k^2}{2M} - \frac{R^*}{n^2} \tag{1.6}$$

where R^* is the Rydberg constant for the exciton defined by $R^* = \mu e^4/2\hbar^2\varepsilon^2$. A schematic of the energies is shown in figure 1.1.

In bulk semiconductors, the exciton wave number is not quantized due to the lack of quantum confinement. However, excitons in confined systems will have a component of the wave vector quantized for each direction of confinement.

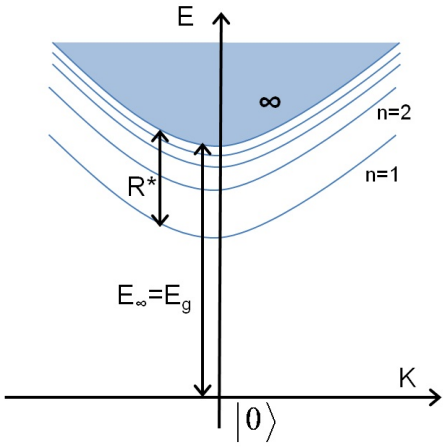

Figure 1.1: Schematic of the energies of an exciton from its ground to an uncoupled electron-hole pair. The energy levels are parabolic due to the unrestricted kinetic energy of the center-of-mass motion of the exciton. E_∞ is equal to E_g, the electronic bandgap of the material, where the electron-hole pair no longer interact through the Coulomb potential, and their motion is uncorrelated.

1.2 Effects of Quantum Confinement

In order to demonstrate the effects of quantum confinement, the case of an electron in a type I quantum well will be considered. For a quantum well of height V, and length L, along the z-direction, the Schrödinger's equation for the particle is:

$$\left[-\left(\frac{\hbar^2}{2m_w}\right)\nabla^2_{\mathbf{R}}\right]\Psi_w(\mathbf{R}) = E\Psi_w(\mathbf{R}) \qquad \text{for } |z| \leq L/2 \tag{1.7a}$$

$$\left[-\left(\frac{\hbar^2}{2m_b}\right)\nabla^2_{\mathbf{R}} + V\right]\Psi_b(\mathbf{R}) = E\Psi_b(\mathbf{R}) \qquad \text{for } |z| > L/2 \tag{1.7b}$$

where m_w and m_b are the effective masses in the well and barrier materials (which need not be the same). With confinement in only the z-direction, the solution may be expressed as:

$$\Psi_{w(b)}(\mathbf{R}) = \phi_{w(b)}(x,y)\psi_{w(b)}(z) \tag{1.8}$$

where $\phi_{w(b)}(x,y)$ describes a free particle having plane wave solutions:

$$\phi_{w(b)}(x,y) = e^{i(k_x x + k_y y)} \tag{1.9}$$

Therefore, equations 1.7a and 1.7b can be rewritten as:

$$-\left(\frac{\hbar^2}{2m_w}\right)\left(\frac{d^2}{dz^2} - k_x^2 - k_y^2\right)\psi_w(z) = E\psi_w(z) \qquad \text{for } |z| \le L/2 \tag{1.10a}$$

$$\left[-\left(\frac{\hbar^2}{2m_b}\right)\left(\frac{d^2}{dz^2} - k_x^2 - k_y^2\right) + V\right]\psi_b(z) = E\psi_b(z) \qquad \text{for } |z| > L/2 \tag{1.10b}$$

For bounded solutions, the energy must satisfy the condition:

$$E - \frac{\hbar^2}{2m_b}(k_x^2 + k_y^2) < V \tag{1.11}$$

allowing the wavefunction to exponentially decay in the barriers. In general, there is no analytical solution for this problem with boundary conditions:

$$\psi_w(z) = \psi_b(z) \qquad \text{at } z = \pm L/2 \tag{1.12a}$$

$$\frac{1}{m_w}\frac{d}{dz}\psi_w(z) = \frac{1}{m_b}\frac{d}{dz}\psi_b(z) \qquad \text{at } z = \pm L/2 \tag{1.12b}$$

However, for the infinite well, analytical solutions exists with quantized energies,

$$E_n = \left(\frac{\hbar^2}{2m_w}\right)\left[\left(\frac{n\pi}{L}\right)^2 + k_x^2 + k_y^2\right] \tag{1.13}$$

showing that confinement increases the minimum energy of the particle by $\hbar^2\pi^2/2m_w L^2$. Similarly if the confinement is extended to other directions, i.e., two directions for quantum wires, and all three directions for quantum dots, the energy will be modified even further.

Although the one-dimensional example of the quantum well is a very basic one, equations 1.7a and 1.7b are very general equations and can be rewritten in cylindrical coordinates for quantum rods, and spherical coordinates for quantum dots. The boundary condition in equations 1.12a and 1.12b written for this specific example can be generalized to the following form:

$$\Psi_w(\mathbf{R}) = \Psi_b(\mathbf{R}) \qquad \text{for } \mathbf{R} \in \partial V \tag{1.14a}$$

$$\frac{1}{m_w}\hat{\mathbf{n}} \cdot \nabla\Psi_w(\mathbf{R}) = \frac{1}{m_b}\hat{\mathbf{n}} \cdot \nabla\Psi_b(\mathbf{R}) \qquad \text{for } \mathbf{R} \in \partial V \tag{1.14b}$$

The boundary condition in equation 1.14a requires the wavefunction to be continuous at the interface (∂V) between the "well" and barrier materials, and equation 1.14b requires the derivative (modified by a factor of $1/m_{w(b)}$) in the direction normal to the interface to be continuous at the interface.

1.3 Photonic Crystals

Optical properties of structures with periodic modulation of dielectric constant has been of great interest in past quarter-century when the concept of light-localization was developed for photonic crystals [6, 7]. One-dimensional photonic structures have been studied a century earlier [8]. Photonic crystals have been instrumental in the enhancement of light-matter interaction, modifying the emission from a gain medium [9–12]. In this work, one-dimensional resonant or active photonic crystals are utilized to manipulate light-matter interaction.

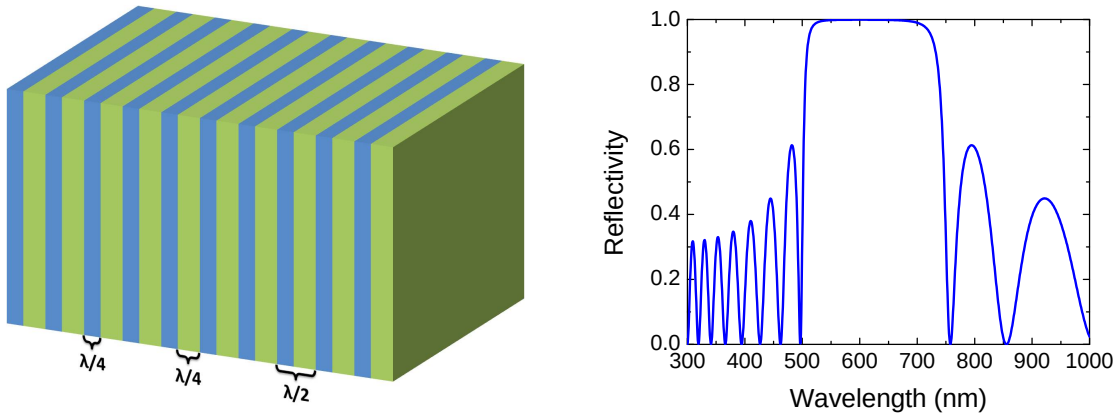

(a) (b)

Figure 1.2: (a) Schematic of a DBR structure showing the multiple bilayers, each of optical thickness $\lambda/4$ for the reflection band centered at λ. (b) Reflection spectrum of an eight period SiO_2/TiO_2 DBR structure. The refractive index for SiO_2, and TiO_2 were taken as 1.45, and 2.47, respectively. The thickness of each layer was set to $\lambda/4n$, where $\lambda = 600$ nm, and n the refractive index of the layer.

The simplest example of a one-dimensional photonic crystal (PC) is the so-called distributed-Bragg-reflector (DBR), where the structure is composed of multiple pairs of bilayers of differing refractive index. For the DBR to have a photonic bandgap centered at λ_0, each of the bilayers are to have optical thickness $\lambda_0/4$. The period of the structure is $\lambda_0/2$ which is the Bragg condition. Under these conditions, the reflection at each of the interfaces will be in phase, resulting in a strong reflection band. A schematic of a DBR structure is shown in figure 1.2a and the reflectivity spectrum is shown in figure 1.2b for eight pairs of SiO_2, and TiO_2 with refractive indices of 1.45, and 2.47, respectively.

A defect introduced in a photonic crystal produces a transmission window in the

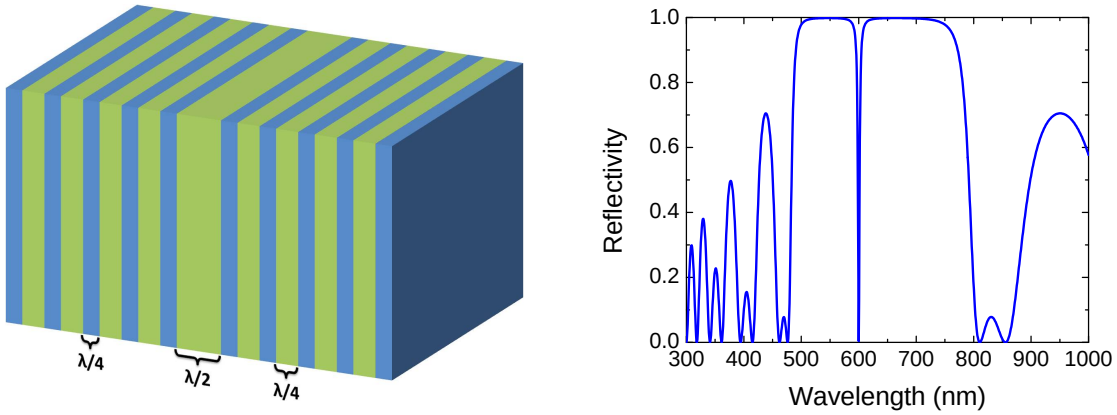

(a) (b)

Figure 1.3: (a) Schematic of a microcavity structure showing the multiple bilayers, each of optical thickness $\lambda/4$, however, the center layer is of thickness $\lambda/2$. (b) Reflection spectrum of a microcavity with SiO_2/TiO_2 DBRs on both side of the cavity layer. Each DBR has five TiO_2 layers and four SiO_2 layers, and the cavity itself is composed of SiO_2. The refractive indices for SiO_2, and TiO_2 were taken as 1.45, and 2.47, respectively. The thickness of each layer was set to $\lambda/4n$, where $\lambda = 600$ nm, and n the refractive index of the layer.

photonic bandgap much like how defects in semiconductors introduce a *defect* state in the electronic bandgap. By changing the thickness of one of the $\lambda/4$ layers to $\lambda/2$, there is now a defect in the photonic crystal. An alternative approach to view this *defect* is to view it as a spacer or *cavity* layer. This cavity layer serves as a means trapping light between the two DBRs. Such a structure is known as a *microcavity*. A schematic of a microcavity structure is shown in figure 1.3a and its reflection spectrum is shown in figure 1.3b.

A comparison of the optical field intensity at the center of a DBR and a MC are shown in figure 1.4a and figure 1.4c, respectively. The optical field intensity map over

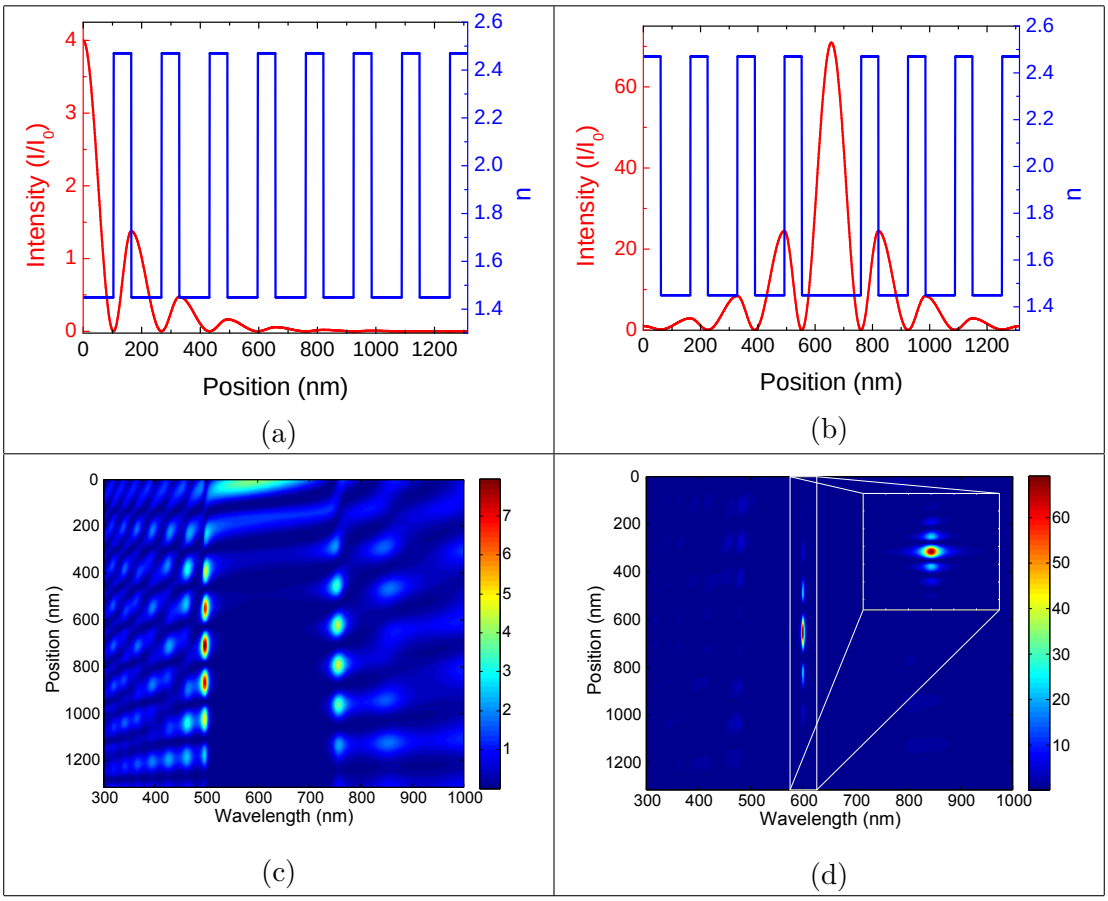

Figure 1.4: Optical field intensity inside the (a) DBR and (b) microcavtiy at $\lambda =$ 600 nm. Th field in the DBR drops rather quickly, while the field in the microcavty is enhanced by a factor $\approx$75 at the center of the cavity. (c) Intensity map of across a spectral region from 300 nm to 1000 nm showing the field quickly becomes dark in the DBR, although there is slight enhancement at the bandedges. (d) The intensity map for the same spectral region of the microcavity, showing a large enhancement in the cavity layer only when on resonance with the transmission window. The field elsewhere is dark in comparison. The DBR and microcavity structures used are the same as for figures 1.2b and 1.3b, respectively.

a wide spectral region of a DBR that shows the field drops inside the bandgap rather quickly. There are regions of high field intensity at the bandedges of the DBR. The intensity map is shown in figure 1.4b. In contrast, the intensity map of a microcavity

shows a large field enhancement in the cavity layer and only on resonance with the transmission window (seen in figure 1.3b). This intensity map of the microcavity is shown in figure 1.4d.

In this work, a periodic arrangement of quantum confined excitons will be made to interact coherently with a one-dimensional photonic crystal to highlight the exciton-photon interaction. Microcavity structures will be used to enhance the emission of colloidal quantum dots as well as to provide a mechanism to tune the coupling strength between coupled microcavity structures.

Chapter 2

Experimental Setup

2.1 Fabrication Tools and Techniques

2.1.1 Spin-Coating

Spin-coating is a widely used technique for coating thin, and uniform films on a substrate. The operating principle of the apparatus is rather simple. A vacuum chuck is used to keep the sample fixed in place while spinning, and a motor is used rotate the chuck (and sample) at a controlled speed. The model used is a Laurell® 400-series spin-coater. It has a maximum spin speed of 10,000 rpm, and is capable of multi-step processes. The apparatus is shown in figure 2.1a.

The spin-coating process starts by preparing a substrate to be used and placing on the chuck. A dropper is then used to dispense the solution on the substrate. After the

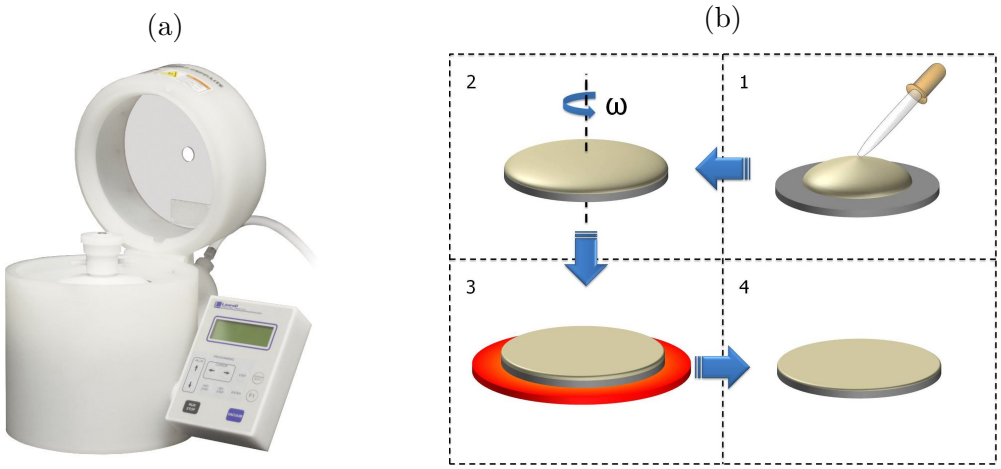

Figure 2.1: (a) Laurell® 400-series spin coater. (b) Flow chart of the spin-coating process: (1) Liquid is dispensed on the substrate. (2) Substrate is rotated at a predetermined speed and time. (3) The film is thin and uniform; however, some solvent still remains. The remaining solvent is removed by heating on a hotplate. (4) The resulting film is the desired thickness and solvent-free.

solution has been dispensed, the spinning begins at a predetermined rate and time. At the end of the spinning step, the polymer is thin and uniform. The remaining solvent is then removed by placing the sample on a hotplate. The entire process is outlined in figure 2.1b.

The spinning step is usually carried out in at least two steps, a slow speed to distribute the polymer across the entire substrate, and a fast speed to reduce the thickness of the polymer film. The thickness is controlled by the spin speed; generally, the faster the spin speed, the thinner the resulting film. The chemical used in many photonic applications are photoresists. SU8 is one such chemical manufactured by MicroChem Corporation. SU8 is produced in a number of variations to cover a range of thicknesses $< 1 - 100\mu m$. Spin speed curves for some variants in the the SU8-2000

series is shown in figure 2.2.[1]

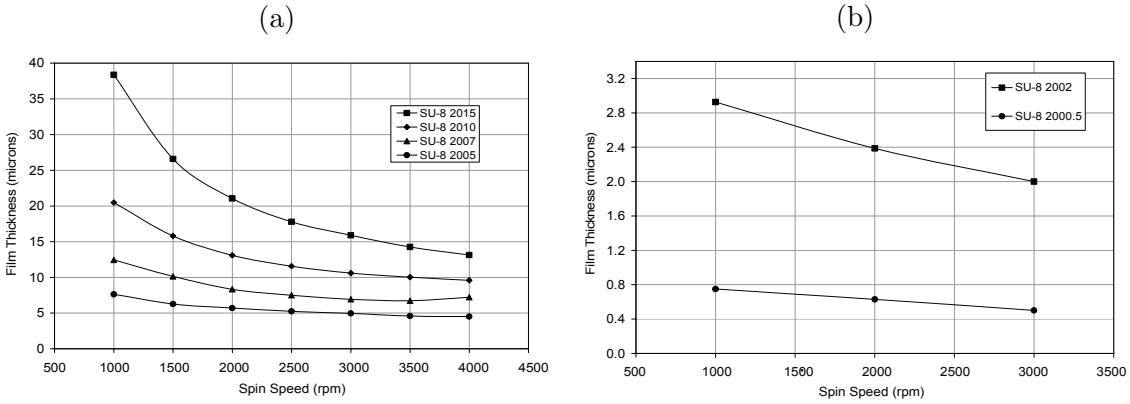

Figure 2.2: Spin speed curves for SU8 photoresists in the 2000-series. For spin speeds of 3000 rpm (a) film thicknesses from $15\mu m$ down to $5\mu m$. (b) films of $2\mu m$ and $500nm$.

2.1.2 Dip-Coating

Dip-coating is another technique used to deposit thin films, specifically for nanoparticles. This technique is similar to the LangmuirBlodgett technique, however, it may be used to deposits thicker films than a single monolayer at once. This technique relies on the immiscibility of solvent of the nanoparticles (hexane or toluene) and a denser liquid (water). The process begins by filling a basin with water and partially submerging the substrate while the other end is attached to a linear motorized translation stage. The nanoparticle solution is then dispensed on top of the water while taking care not to agitate the water-solvent interface. After the solvent settles on top of the water, the substrate is pulled up at a controlled speed by the motor causing

[1]MicroChem Corp. - `http://www.microchem.com`

the nanoparticles to adhere to the substrate, resulting in a film of nanoparticles on the surface of substrate. The thickness and uniformity of the film is controlled by the pulling speed and concentration of nanoparticles. The stages of the dip-coating process is shown in figure 2.3.

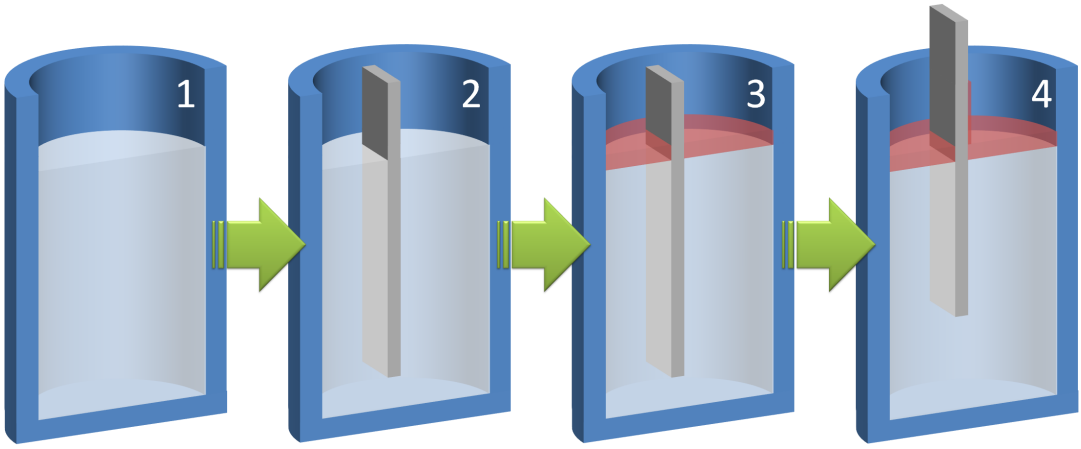

Figure 2.3: Dip-coating procedure: (1) Container is filled with water. (2) One end of the substrate is attached to a linear motor and the other is partially submerged in the water. (3) Nanoparticle solution is carefully dropped on the surface of the water. (4) The substrate is slowly pulled out at a controlled speed leaving a thin film of nanoparticles on the surface.

2.1.3 Plasma-Enhanced Chemical Vapor Deposition (PECVD)

To fabricate high quality and optically uniform dielectric films, plasma-enhanced-chemical-vapor-deposition (PECVD) is a commonly used technique. Gases flow into the system where they are mixed, and enter the process chamber. The pressure of in the chamber is controlled by a vacuum pump which serves as an exhaust outlet for the processed gas. A plasma is generated by an RF-signal apply between the

top and bottom plates of the chamber. The ions from the plasma deposit on the surface of the sample and form a film at a uniform rate. The composition of the film is determined by the gases being processed in the chamber, and the quality is optimized by temperature, RF power, and chamber pressure. A schematic of the PECVD system is shown in figure 2.4.

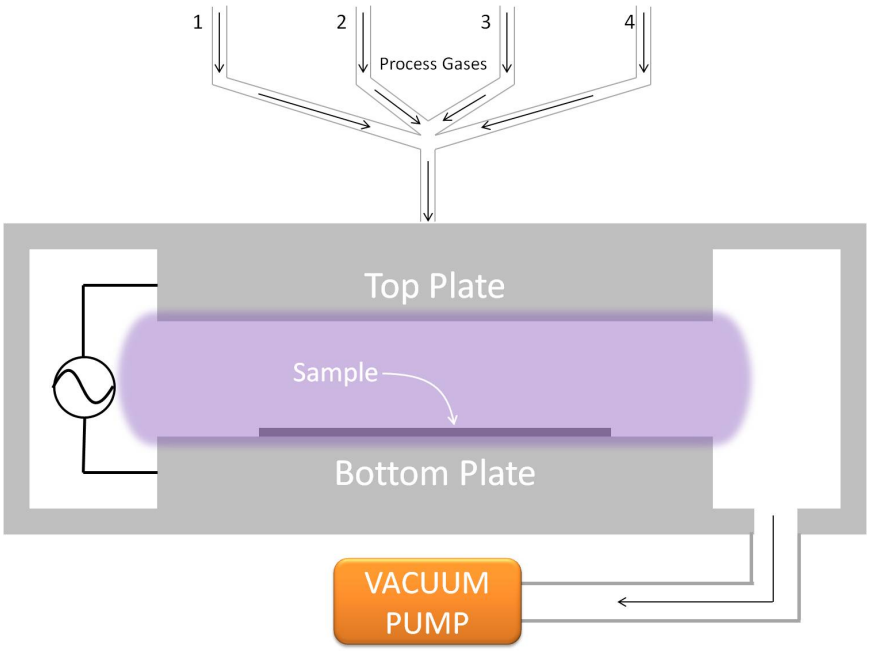

Figure 2.4: Schematic of PECVD system. Different gases flow and are mixed before entering the chamber. A sample substrate is placed on the bottom plate of the chamber which is at a preset temperature. The gases flow into the chamber through the top plate where a plasma is created by the applied RF signal applied across the top and bottom plates. The chamber pressure is controlled by a vacuum pump which serves as an exhaust for the processed gases.

2.2 Characterization Tools and Techniques

2.2.1 Thin-Films

In section 2.1, we have seen how different materials can be deposited on substrates. Characterizing these films is an essential part of the fabrication process. The simplest form of characterization is a film-thickness measurement. Although film-thickness is a very basic characteristic, it is one of the most important. For most of the structures we use, the optical thickness, nl (where n is the refractive index, and l film thickness), is needed in order to design the phontonic structure of interest.

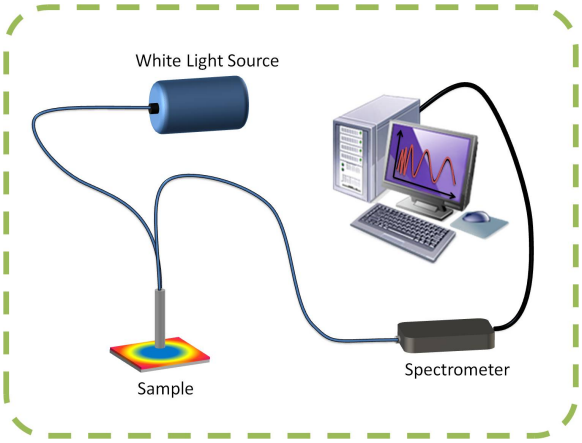

Figure 2.5: A schematic of a reflectance measurement setup

There are two widely used non-destructive methods used to calculate the thickness of thin-film: ellipsometry, and reflectance. For characterizing ordinary dielectric films, we use the reflectance method, due to its simplicity. The method involves using a white-light source to illuminate the film, and the reflected light is sent to a spec-

trometer to measure the reflectance spectrum. The reflection spectrum is then fitted to a single layer think-film model. A schematic of the setup is shown in figure 2.5.

To simulate the reflectance, a three-medium model is used. Medium 1 with refractive index n_1, is where the light originates, medium 2 (n_2), which has thickness l, is used as the thin-film, and medium 3 (n_3), is with substrate and is considered to have infinite thickness. Considering all possible multiple reflections between the two interfaces, one can construct the infinite sum of all the reflected waves. For the incident E-field amplitude of E_0, the amplitude of the reflected wave can be written as the sum of all the reflected waves:

$$E_{reflected} = E_0 \left(r_{12} + t_{21} r_{23} t_{12} e^{2ikl} + t_{21} r_{23} r_{21} r_{23} t_{12} e^{4ikl} + t_{12} r_{23} \left(r_{21} r_{23} \right)^2 t_{12} e^{6ikl} \cdots \right) \tag{2.1}$$

Where r_{ij} (t_{ij}) is the reflection (transmission) coefficient from medium n_i to n_j, and k is the wave number. A schematic of examples of the multiple reflection process is shown in figure 2.6. The terms on the right-hand-side of equation 2.1 can be expressed as a geometric series:

$$E_{reflected} = E_0 \left[r_{12} + t_{12} r_{23} t_{21} e^{2ikl} \sum_{m=0}^{\infty} \left(r_{21} r_{23} e^{2ikl} \right)^m \right] \tag{2.2a}$$

$$= E_0 \left[r_{12} + \frac{t_{12} t_{21} r_{23} e^{2ikl}}{1 - r_{21} r_{23} e^{2ikl}} \right] \tag{2.2b}$$

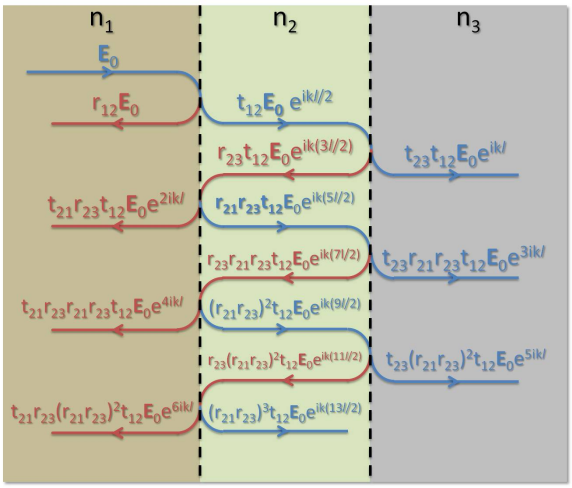

Figure 2.6: A schematic of an EM-wave originating in medium with refractive index n_1, traveling to the right (color blue), and incident on a medium with refractive index n_2, which is on a substrate of refractive index n_3. The first few reflections and transmissions at the two interfaces are shown. The blue colored lines represents waves traveling to the right, and red (reflected waves) traveling to the left.

The reflectance (R) can be written as:

$$R = \left| r_{12} + \frac{t_{12}t_{21}r_{23}e^{2ikl}}{1 - r_{21}r_{23}e^{2ikl}} \right|^2 \tag{2.3}$$

At normal incidence, the reflection and transmission coefficients can be expressed in terms of the refractive indices by:

$$r_{ij} = \frac{n_i - n_j}{n_1 + n_j} \tag{2.4a}$$

$$t_{ij} = \frac{2n_i}{n_i + n_j} \tag{2.4b}$$

By noticing the relation, $t_{ij} - r_{ij} = 1$, we can rewrite equation 2.3 as:

$$R = \left| \frac{r_{12} + r_{23}e^{2ikl}}{1 - r_{21}r_{23}e^{2ikl}} \right|^2 \tag{2.5}$$

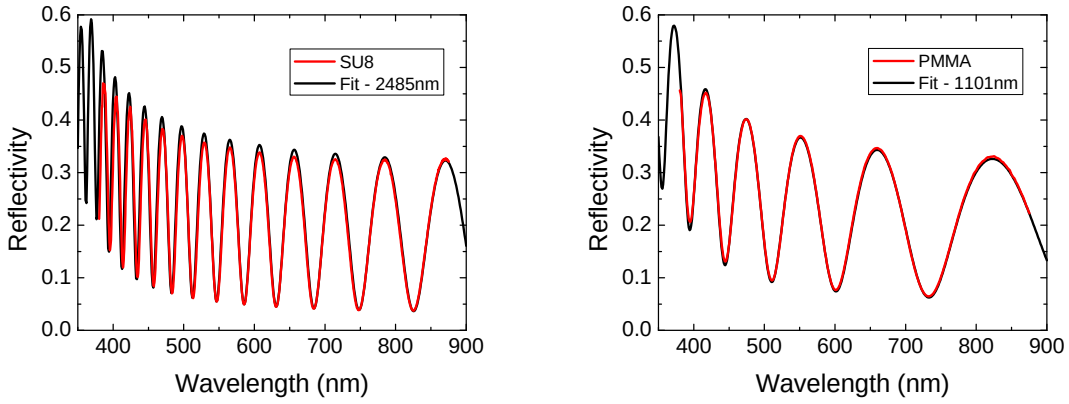

(a) (b)

Figure 2.7: Examples of polymer films spin-coated (see section 2.1.1 for further details) on a silicon substrate. (a) The reflectance of SU8 and (b) PMMA.

In a similar fashion, we can sum the transmitted terms to get the following:

$$E_{transmitted} = E_0 t_{23} t_{12} e^{ikl} \sum_{m=0}^{\infty} \left(r_{21} r_{23} e^{2ikl}\right)^m \tag{2.6a}$$

$$= E_0 \left[\frac{t_{23} t_{12} e^{ikl}}{1 - r_{21} r_{23} e^{2ikl}}\right] \tag{2.6b}$$

The transmittance (T) can be written as:[2]

$$T = Re\left\{\left(\frac{t_{32}}{t_{23}}\right)\left(\frac{t_{21}}{t_{12}}\right)\right\}\left|\frac{t_{23} t_{12} e^{ikl}}{1 - r_{21} r_{23} e^{2ikl}}\right|^2 \tag{2.7}$$

Although modeling the reflectivity by equation 2.5 works rather well, there are limitations. There are two parameters that are taken as an input for the model, (1) thickness, l, and (2) refractive index, n. The fitting procedure works best when one of these parameters are known, and equation 2.5 is used to fit the data for the

[2]The difference between the indices in the numerator of equation 2.6b and 2.7 is due to the prefactor in the Poynting vector, $|S| \sim n\,|E|^2$. The transmittance will add a prefactor of n_3/n_1, which can be expressed as $(t_{32}/t_{23})(t_{21}/t_{12})$. This prefactor does not appear in the reflectance because the incident and reflected media, n_1 and n_3, are identical.

other. Typically, the refractive index of the material is known and the thickness is calculated. Figure 2.7 shows examples of such fitting. Figure 2.7a and 2.7b show two different polymer films, SU8, and PMMA, respectively, where the refractive index is given by the manufacturer and the thickness varies depending on the deposition process. A common method for obtaining highly uniform films is the spin-coating process. In this process, the thickness is a function of the spin-speed; faster speeds yield thinner films. See section 2.1.1 for further details on the spin-coating process. The MATLAB code for the reflectance, transmittance, and absorbance spectra is included in appendix A.[3]

2.2.2 Multi-Layer Structures and the Transfer Matrix Method

In section 2.2.1, we saw how to characterize a single layer on a substrate by modeling the reflectance. We started by writing the sum of the amplitudes of reflected waves in equation 2.1. However, if we attempt to generalize that approach to a two-layer system, writing the multiply reflected terms would be extremely difficult, and even more so for an arbitrary number of layers. Therefore, we use a different approach to calculate the scattering spectra for a multi-layer structure.

The transfer-matrix-method (TMM) is the general approach taken for systems such as this. The concept of the TMM is to *'transfer'* the field (or field amplitudes)

[3]The code is written to account for an arbitrary angle of incidence and different polarization directions. The reflection and transmission coefficients used to account for these additional variables is shown in equation 2.16.

from one point in space to another. For linear systems the relationship between the fields at location z_0 is related to the fields at a location $z_0 + z$ by a matrix equation:

$$\begin{pmatrix} E^+(z_0+z) \\ E^-(z_0+z) \end{pmatrix} = \begin{pmatrix} t_{11} & t_{12} \\ t_{21} & t_{22} \end{pmatrix} \begin{pmatrix} E^+(z_0) \\ E^-(z_0) \end{pmatrix} = \mathbf{T} \begin{pmatrix} E^+(z_0) \\ E^-(z_0) \end{pmatrix} \tag{2.8}$$

where the $(+)$, and $(-)$, superscripts denote positive and negative directions of propagation, respectively. Using this notation, the reflection and transmission coefficients are found to be:

$$r = -\frac{t_{21}}{t_{22}} \tag{2.9a}$$

$$t = \frac{\det(\mathbf{T})}{t_{22}} \tag{2.9b}$$

The full power of the TMM is in extending the *transfer* process. If we have a general expression for transfer-matrix between points i, and j;

$$\begin{pmatrix} E_j^+ \\ E_j^- \end{pmatrix} = \mathbf{T}_{ij} \begin{pmatrix} E_i^+ \\ E_i^- \end{pmatrix} \tag{2.10}$$

We can see that we would like to transfer the field from $1 \to 2 \to \ldots \to (N-1) \to N$,

the transfer matrix equation can be expressed as:

$$\begin{pmatrix} E_N^+ \\ \\ E_N^- \end{pmatrix} = \mathbf{T}_{(N-1)N}\mathbf{T}_{(N-2)(N-1)}\cdots\mathbf{T}_{23}\mathbf{T}_{12}\begin{pmatrix} E_1^+ \\ \\ E_1^- \end{pmatrix} \tag{2.11a}$$

$$\begin{pmatrix} E_N^+ \\ \\ E_N^- \end{pmatrix} = \mathbf{T}_{total}\begin{pmatrix} E_1^+ \\ \\ E_1^- \end{pmatrix} \tag{2.11b}$$

where the total transfer matrix, $\mathbf{T}_{total}$, the the product of all the individual matrices. The reflection and transmission coefficients still have the form of equation 2.9, however, the t_{ij}'s are now the elements of $\mathbf{T}_{total}$.

For wave propagation through uniform media of length l and refractive index n, the transfer matrix takes the form:

$$\mathbf{T} = \begin{pmatrix} e^{i\phi} & 0 \\ \\ 0 & e^{-i\phi} \end{pmatrix} \tag{2.12}$$

where $\phi = 2\pi nl/\lambda$ is the phase gained (lost) by the wave propagating in the forward (backward) direction. The transfer matrix at an interface between two media of refractive index n_i and n_j can be expressed in terms of the reflection coefficient as:

$$\mathbf{T}_{ij} = \frac{1}{t_{ji}}\begin{pmatrix} 1 & -r_{ij} \\ \\ -r_{ij} & 1 \end{pmatrix} \tag{2.13}$$

For the case of a single film on a substrate as shown on section 2.2.1, the total

transfer matrix can be expressed as:

$$\mathbf{T}_{total} = \frac{1}{1-r_{23}} \begin{pmatrix} 1 & -r_{23} \\ -r_{23} & 1 \end{pmatrix} \begin{pmatrix} e^{i\phi_2} & 0 \\ 0 & e^{-i\phi_2} \end{pmatrix} \frac{1}{1-r_{12}} \begin{pmatrix} 1 & -r_{12} \\ -r_{12} & 1 \end{pmatrix} \tag{2.14a}$$

$$= \left(\frac{1}{1-r_{23}}\right)\left(\frac{1}{1-r_{12}}\right) \begin{pmatrix} e^{i\phi_2} + r_{12}r_{23}e^{-i\phi_2} & -r_{12}e^{i\phi_2} - r_{23}e^{-i\phi_2} \\ -r_{23}e^{i\phi_2} - r_{12}e^{-i\phi_2} & e^{-i\phi_2} + r_{12}r_{23}e^{i\phi_2} \end{pmatrix} \tag{2.14b}$$

When using the expression from equation 2.9 to compute the reflectance, we obtain:

$$R = \left| \frac{r_{12} + r_{23}e^{2i\phi}}{1 + r_{12}r_{23}e^{2i\phi}} \right|^2 \tag{2.15}$$

which is identical[4] to the expression in equation 2.5

Equations 2.12 and 2.13 can be generalized for an arbitrary angle of incidence, θ. The phase, ϕ, through the medium will be modified to account for the phase perpendicular to the interface such that $\phi = 2\pi nl\cos\theta/\lambda$, where θ is the angle between the direction of propagation inside the medium and normal to the interface. The reflection coefficients will change for different directions of polarization as:

$$r_{ij}^S = \frac{n_i\cos\theta_i - n_j\cos\theta_j}{n_i\cos\theta_i + n_j\cos\theta_j} \qquad t_{ij}^S = \frac{2n_i\cos\theta_i}{n_i\cos\theta_i + n_j\cos\theta_j} \tag{2.16a}$$

$$r_{ij}^P = \frac{n_i\cos\theta_j - n_j\cos\theta_i}{n_i\cos\theta_j + n_j\cos\theta_i} \qquad t_{ij}^P = \frac{2n_i\cos\theta_i}{n_i\cos\theta_j + n_j\cos\theta_i} \tag{2.16b}$$

[4]The expression are identical when noting that $r_{ij} = -r_{ji}$, as seen from equation 2.16.

Where the S (P) superscript denotes S (P)-polarization.[5] One should note from equation 2.16a that $t_{ij}^{S} - r_{ij}^{S} = 1$, however, from equation 2.16b, $t_{ij}^{P} - r_{ij}^{P} \neq 1$. Therefore, the substitution made in equations 2.5 and 2.14 is only valid for S-polarization and normal incidence.

2.2.3 Angle-Dependent Spectroscopy

Often in experiments it is necessary to measure optical spectra at an angle. In order to accomplish this, we use an optical fiber coupled Tungsten Halogen white light source attached to one arm of a goniometer where a system of two lenses is used to focus light on the sample. The second arm of the goniometer has an identical set of lenses to focus the reflected light into a fiber coupled CCD based spectrometer. The arms can be moved to measure reflection from $\sim 12^{\circ}$ to $\sim 80^{\circ}$. The setup is schematically shown in figure 2.8a.

Angle dependent photoluminescence (PL) measurements are typical in order to characterize the dispersive properties of the system. To this end, a similar setup it used, however with only the collection arm of the goniometer. A laser is incident on the sample as a pump source at a glancing angle, and the emission is collected, as mentioned previously. A schematic is shown in figure 2.8b.

In semiconductor samples, it is often advantageous to carry out spectroscopic

[5] S-polarization is for the electric field is perpendicular the the plane of incidence, and P-polarization is for the electric field is parallel to the plane of incidence.

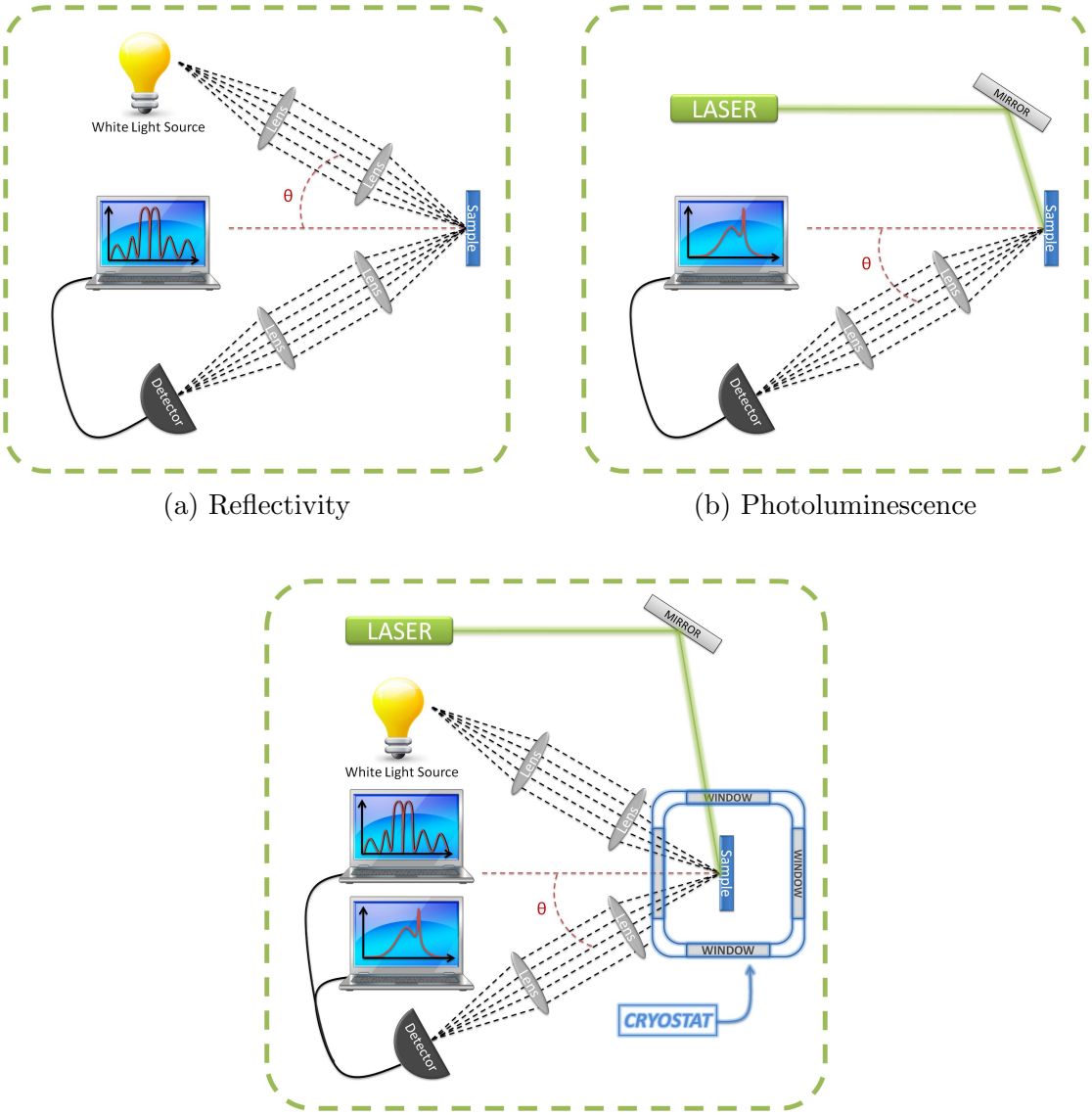

(a) Reflectivity

(b) Photoluminescence

(c) Low-temperature setup

Figure 2.8: (a) Schematic of angle dependent reflection setup. Reflection can be measured from an angle as small as ∼12° up to ∼80°. The lower limit is a physical constraint when the arms of the goniometer touch each other. The upper limit, however, is due to the highly elliptical cross-section of the beam at large incident angles. (b) Similar setup for measuring PL at angle between $\sim -80° - 80°$. The lower angular limit is removed due to the necessity of a single arm of the goniometer. (c) For low-temperature measurements, the sample is placed in a cryostat which has the capability to carry out both reflectivity and PL measurements simultaneously.

measurements at low temperatures in order to reduce the exciton-phonon scattering. In order to accomplish this, we place the sample in a closed cycle liquid Helium cooled cryostat and placed the necessary optics around it to be able to simultaneously measure reflectivity and PL. A schematic of the setup is sketched in figure 2.8c.

2.2.4 Time-Correlated Single Photon Counting

Time-correlated single-photon counting (TCSPC) is a widely used technique to measure the lifetimes of emitters [13, 14]. The technique relies on the principle that intensity verses time profile of all the photons emitted is equivalent to the probability distribution of the emission of a single photon. In this way, it is possible to perform many measurements by detecting single photons, and obtain a statistical lifetime of the emitter. To this end, a FluoroMax system from Horiba is used to measure the emission lifetime is this work.

The details of a typical TCSPS system involves a pulsed excitation excitation source and a fast detector. The excitation source is required to have a narrow pulse width compared to the lifetime of the emitter in order to obtain meaningful lifetimes from the instrument. It is best to have fast electronics and detectors in order to reduce a broadening effect of the excitation pulse. The limiting factor in lifetime resolution in sophisticate experimental apparatus is the pulse width of the excitation source.

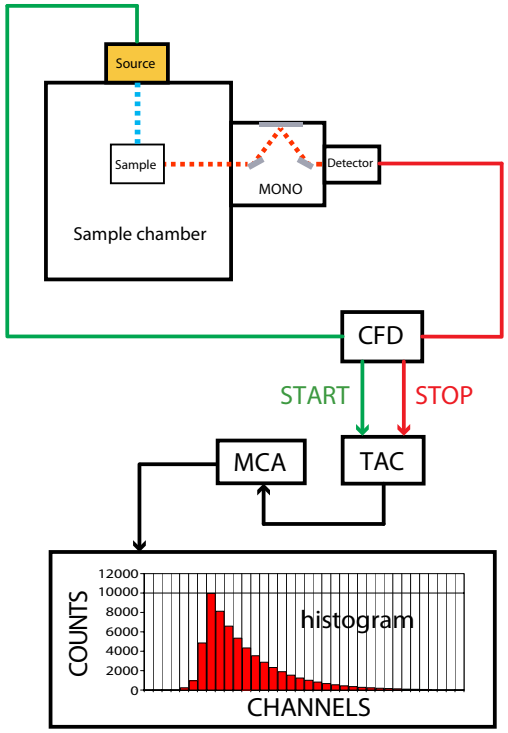

Figure 2.9: A pulse is emitted from the source which signals the constant-fraction discriminator (CFD) to start the voltage ramp on the time-to-amplitude converter (TAC). After the CFD registers the first emitted photon, it signals the TAC to stop. The resulting information is then sent to a multichannel analyzer (MCA) which is then displayed on a histogram. The process is repeated until one channel reaches a preset number of counts (10,000 shown in the histogram).

The basic TCSPC functioning process is as follows. A pulse is emitted from the source which signals the constant-fraction discriminator (CFD) to start the voltage ramp on the time-to-amplitude converter (TAC). After the CFD registers the first photon from the detector, it signals the TAC to stop. The resulting information is then sent to a multichannel analyzer (MCA) which is then displayed on a histogram. The process is repeated until one channel reaches a preset number of counts. The stop count is usually a large number, considering the statistical nature of the technique. A

typical value used is 10,000 counts. A schematic of this process is shown in figure 2.9. This mode of operation is known as the "forward TAC mode". The "reverse TAC mode" is very similar, the only difference being the *start* and *stop* of the TAC are reversed; i.e., the TAC is started by the detector, and stopped by the excitation source.

The ideal excitation pulse is a delta pulse; however, in many samples this cannot be assumed because the pulse width, Δt_{pulse}, is not orders of magnitude smaller than the decay. In this case, the measured decay is modeled by the convolution of the excitation pulse (prompt) and a decay model:

$$D(t) = \int_0^t P(\tau)M(t-\tau)d\tau \tag{2.17}$$

where $P(t)$ is the prompt profile, and $M(t)$ is the model used for the decay. The most common models used are either single or double exponential decay. To illustrate this effect, the convolution in equation 2.17 for a Gaussian pulse with a single, and double exponential model are shown in figures 2.10 and 2.10b, respectively. The Gaussian pulses used in the convolution in figure 2.10 have a pulse width, $\sigma = 0.1$, 0.5, and 1, where σ is the standard deviation of of the Gaussian distribution.

The lifetime of semiconductor quantum dots (QDs) often exhibit a double exponential decay, where the fast lifetime (τ_1) is $\sim$10 ns, and the long lifetime (τ_2) is $\sim$30 ns. In type I semiconductor quantum dots, there is Auger recombination, which is a fast nonradiative process (see section 5.5.5 for further details), typically

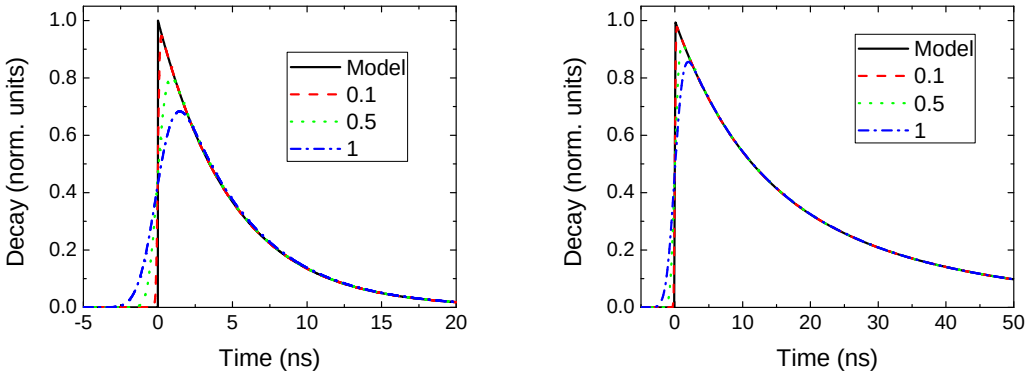

Figure 2.10: The convolution in equation 2.17 for a Gaussian pulse with (a) single exponential model with a lifetime of 5 ns, and (b) double exponential model with a lifetime of 10 ns, and 30 ns. The Gaussian pulses used for the convolution have a pulse width, $\sigma = 0.1$, 0.5, and 1, where σ is the standard deviation of of the Gaussian distribution.

with a lifetime of ∼100 ps. The TCSPC technique measures total lifetime, however, many systems, including the system used in this work, does not have a high enough resolution to measure such fast processes.

At times a multi-exponential fit is not suitable for the emitter, and a stretch exponential function is taken as the model where the decay is of the form:

$$D(t) = e^{-(t/\tau)^{\beta}} \tag{2.18}$$

where β, and τ are the stretching parameter, and decay parameters, respectively. For stretching, $0 < \beta < 1$, and compress is for $\beta > 1$. Notably, when $\beta = 2$ is Gaussian decay. The stretching regime is more commonly used for modeling decays that do not fit well to multi-exponential forms. A plot of the stretch exponential function is

shown in figure 2.11 for various β values, notably, $\beta = 1$, is the usual exponential, and $\beta = 2$ is the Gaussian exponential. This model is used when a decay has faster than exponential decay at short time scales, and slower decay at longer timescales.

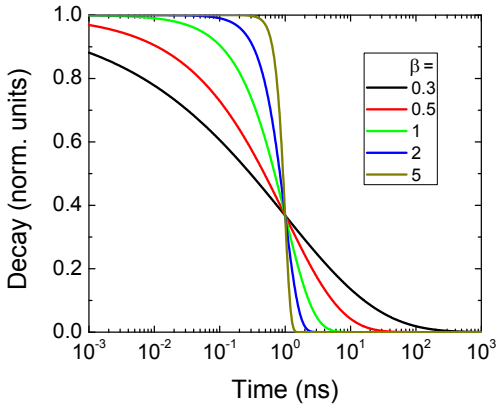

Figure 2.11: The stretch exponential function shown for $\tau = 1$ ns, and $\beta = 0.5$, 1, 2, and 5. The usual exponential is for $\beta = 1$, for $\beta < 1$ the function appears to be stretched, while for $\beta > 1$ the function is compressed.

For the fitting of decay models, an iterative method to find the smallest "goodness of fit" parameter χ^2, where $\chi^2 \leq 1.2$ is generally accepted as a good fit [15].

2.2.5 Photoluminescence and Absorption

In addition to the photoluminescence (PL) setup mentioned in section 2.2.3, a more sensitive setup that can be used for both solid and solution samples. The setup makes use of a high powered white-light source which enters into a monochromator and used as an excitation source. The emission from the sample is then through an aperture before at the opening of a second monochromator which scans through

different wavelengths and finally reaches a single-photon detector. A schematic of this setup is shown in figure 2.12. The advantages of this system is the ability to measure PL for weakly fluorescent samples, and the resolution is determined by the aperture spacing.

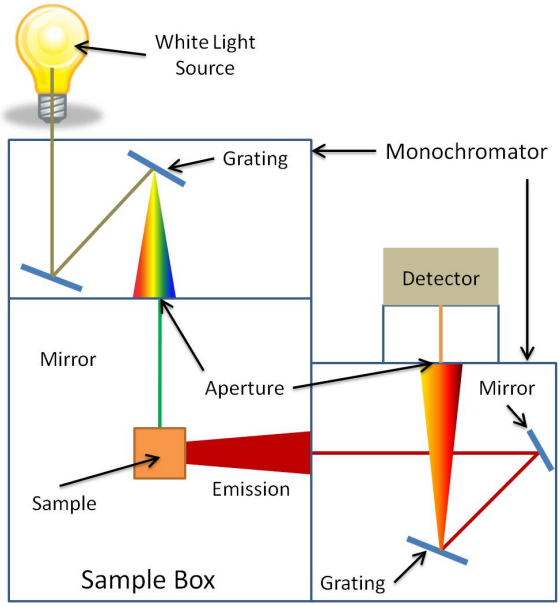

Figure 2.12: A white-light source enters through a monochromator to be used as the excitation source. The emission from the sample is then through an aperture before at the opening of a second monochromator which scans through different wavelengths and finally reaches a single-photon detector, which records the PL emission intensity by photon counts.

This system does have its advantages, however, the disadvantages limit its usage. Angle dependent PL measurements are possible with solid samples; however, the angular range is quite limited due to the fixed components in the system. For angle dependent steady-state PL measurement, the setup described in section 2.2.3 is more preferable than this one, due to the ease of reconfigurability of all the components.

A similar setup is used for absorption measurements. Here, white-light enters a monochromator which scans the range of wavelength; there is no second monochromator. Figure 2.13 shows a schematic of the light emitted from a white-light source where it enters a monochromator which scans through different wavelengths. This light now enters the sample chamber where it passes through the sample and is finally detected.

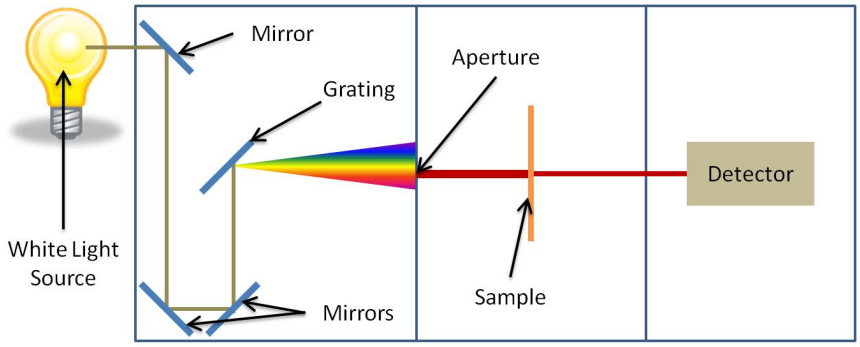

Figure 2.13: White-light enters the system through a monochromator which scans a range of wavelengths, and there is no second monochromator. After entering the sample chamber, it passes through the sample and is finally detected. The intensity data is then processed to show the absorbance spectrum.

The measurement is done in two different steps where the first involves collecting a reference spectrum. For this, either the substrate or the cuvette (for solid and solution samples, respectively) alone is placed in the sample chamber and the reference transmission spectrum, I_{ref}, is measured. It is important to know the absorption spectrum of solvents used in order to interpret the measurements form solution samples.[6] The sample of interest is then placed in the chamber where the transmission,

[6]Some will place the cuvette with the solvent being used as the reference sample in order to "subtract" the solvent from the absorption.

I_{total}, is measured. The absorbance is then calculated by:

$$A = \log_{10}\left(\frac{I_{total}}{I_{ref}}\right) \tag{2.19}$$

It should be noted that this is not a *true* absorption measurement because the reflectivity off the sample is not measured. This method is only valid when the reflection off the sample is negligibly small.

Part I

Collective Excitonic Phenomena

The enhancement of light-matter interaction in an ensemble of emitters has been of interest since it was proposed by Dicke in 1954 [16]. In Dicke's pioneering work, he considered an ensemble of dipole active atoms geometrically arranged such that the spacing is much less than the emission wavelength of the atom. In this geometry, the atoms emit coherently in a so-called "superradiant" emission, resulting in an increase in the radiative rate, Γ_0, by a factor of the number of atoms in the system, N, such that $\Gamma = N\Gamma_0$.

The work presented here can be viewed as an extension of superradiance in atomic system into semiconductor systems. This work is separated into two sections. The first section, chapter 3, discusses one dimensional quantum well structures where the interquantum well spacing is on the order of the resonant wavelength, while the second, chapter 4, discusses clusters of colloidal quantum dots.

Chapter 3

Resonant Excitonic Lattice

3.1 Introduction

In this chapter, the properties of excitons in a one dimensional periodic arrangement of quantum wells (QWs), excitonic lattice, are described. The effects of incorporating an excitonic lattice in a background photonic crystal is studied as well, and is shown to result in a unique hybrid exciton-polaritons.

3.2 Multiple-Quntum-Well Structures

Optical properties of excitons in QWs can be modified by having a periodic arrangement of identical QWs, or multiple-quantum-well structures (MQWs), with the period equal to the half of the resonant wavelength, $\lambda/2$, the so-called Bragg con-

dition. The optical properties of such systems have been studied both theoretically and experimantaly [17–20]. A schematic of a MQWs with a few periods is shown in figure 3.1.

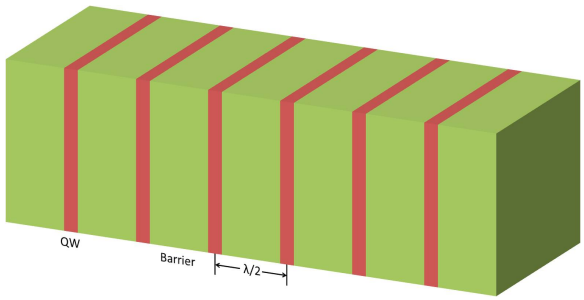

Figure 3.1: Schematic of a MQWs. Each of the QWs are separated by a barrier making the period of the structure equal to $\lambda/2$, the Bragg condition.

In order to understand the properties of MQWs, it is beneficial to understand the optical properties as a function of the number of periods. For this analysis, it is convenient to utilize the transfer matrix method described in detail in section 2.2.2. However, in the case of MQWs, one needs to account for the long-range exciton interaction which is not considered in the case of dielectric media. In order to account for the long-range exciton interaction, the matrix associated with propagation through the QW layer in equation 2.12 needs to be modified to have the form [21]:

$$\mathbf{T} = \begin{pmatrix} e^{i\phi}\,(1 - iS) & -iS \\ iS & e^{-i\phi}\,(1 + iS) \end{pmatrix} \tag{3.1}$$

where ϕ is the normal phase accumulated through propagating across the layer and S is the excitonic contribution to light scattering. This can be described by a function

of the form:

$$S = \frac{\Gamma_0}{\omega - \omega_0 - i\gamma} \tag{3.2}$$

where Γ_0 is the radiative decay rate, and γ is the nonradiative decay rate.

Using the above expression, it is possible to calculate the reflection spectra for any number of periods in a MQW structure. The reflectivity spectrum of a single QW shows a small peak at the resonant wavelength. However, as the number of periods increases, the peak grows larger and eventually develops into a bandgap. The reflectivity spectra of MQWs with various periods ranging from 1 (a single QW) to 150 is shown in figure 3.2. It is important to note that this bandgap is not due

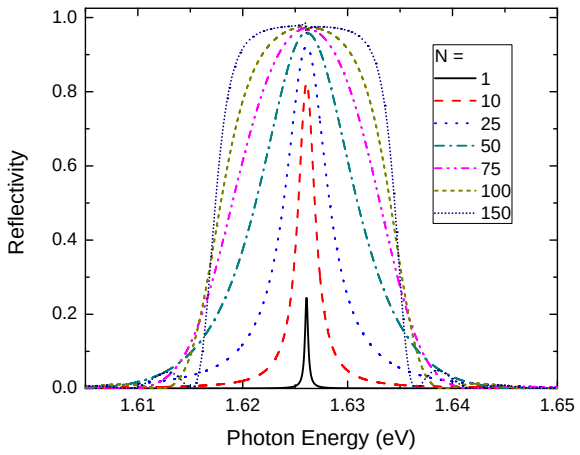

Figure 3.2: Reflectivity of a MQW structure for various periods ranging from 1 to 150. For one period, the refelction spectra show a spike at the resonant energy (1.627 eV) and grows into a band as the number of periods increases. Spectra is calculated using an exciton radiative rate, $\Gamma = 88\ \mu eV$, and non-radiative rate of $\gamma = 90\ \mu eV$.

to the refractive index contrast of the QW and barrier materials. The refractive index contrast, Δn, between the QW and barrier materials is taken to be zero in these calculations. This is a reasonable approximation for InGaAs/GaAs [20]. The

appearance of this bandgap is solely due to the periodic arrangement of excitons under the Bragg condition.

The evolution of the bandgap shown in figure 3.2 is when the resonant wavelength of the QWs is twice the period of the MQWs. If this condition is satisfied, the MQWs is said to be in resonance. It is useful to understand the off-resonance spectra of MQWs as well as the resonant case. If the exciton energy is highly detuned from resonance, the reflectivity is a narrow peak at the exciton energy. As the exciton energy is brought into resonance, the excitons begin to interact coherently, and the narrow peak develops into a band. This is shown in figure 3.3. It should be noted that there are peculiar features near resonance, reminiscent of an anticrossing behavior. This property will be discussed in detail in section 3.4

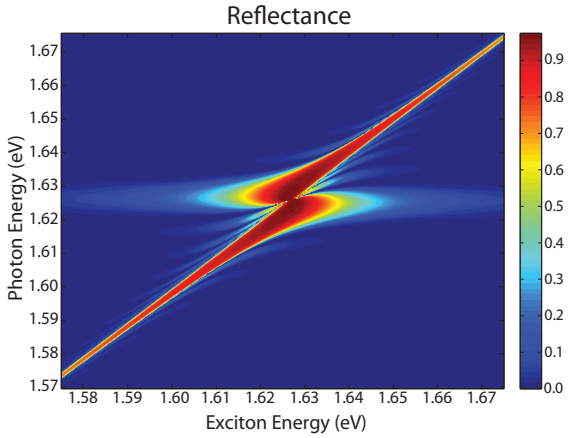

Figure 3.3: Reflection spectra of a set of 150 QWs evenly spaced to create the exciton lattice. For exciton energies highly detuned from the Bragg energy, the reflection shows a narrow peak at the exciton energy. As the exciton energy is tuned into resonance with the Bragg energy, the narrow peak broadens into a reflection band.

3.3 Resonant Photonic Crystals

As shown in section 3.2, a photonic bandgap can arise without an refractive index contrast, but rather with a periodic arrangement of QWs with the period in resonance with the Bragg condition. However, interesting dispersive properties can arise when there is a refractive index contrast between QW and barrier materials. It is important to note there is a change in refractive index in a medium due to the presence of excitons. However, in this discussion, when referring to the refractive index of a material, the concern is with the *background* refractive index, i.e., the refractive index of the material without the excitonic contribution.

Consider again the MQWs schematically shown in figure 3.1, where the background refractive index of the structure is negligible. Detuning the exciton energy from the Bragg resonance was already shown in figure 3.3, it is also important to consider the angular dispersion of the structure. The reflectivity of a MQW on resonance at normal incidence has a bandgap at the exciton resonance, however, as the angle of incidence increases, the Bragg resonance is effectively detuned from the exciton energy, resulting in the formation of a narrow reflection band at the exciton frequency. This effect is shown in figure 3.4.

MQWs with a background refractive index contrast, or a background photonic crystal (PC), have been theoretically considered in the past [22–24]. An ordinary (nonresonant) PC has the familiar Bragg dispersion, and an example of such a PC

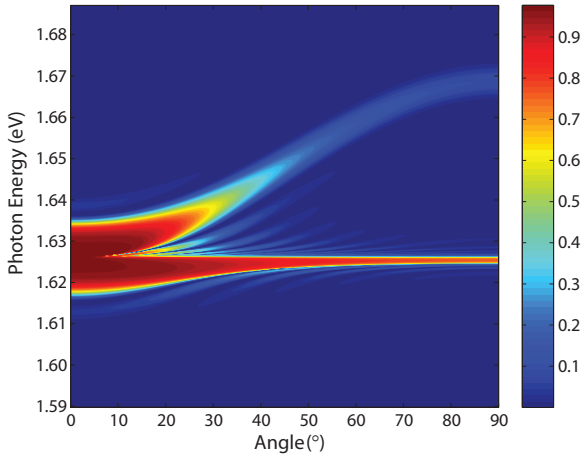

Figure 3.4: Reflection spectra of set of 150 QWs evenly spaced to create the exciton lattice. At small angles of incidence, a photonic bandgap is observed. As the angle increases, the Bragg resonance is detuned from the exciton energy and the bandgap narrows into a peak at the exciton energy.

with $\Delta n = 0.3$ is shown in figure 3.5a. This ordinary PC can be compared to a resonant PC (RPC), i.e., a PC incorporating a material resonant excitation (excitons in this case). For the same MWQs shown in figure 3.4, by changing the refractive index of the QWs to create the background PC, the MQWs properties combine with the Bragg dispersion, yielding the interesting dispersion shown in figure 3.5b.

The reflectivity of the combined structure shows a large bandgap with a narrow propagation window dividing the band in two. The two bands have a combined four bandedges, two of which appear to anticross with each other. This will be discussed in great detail in section 3.4 where the analysis of experimental results is performed.

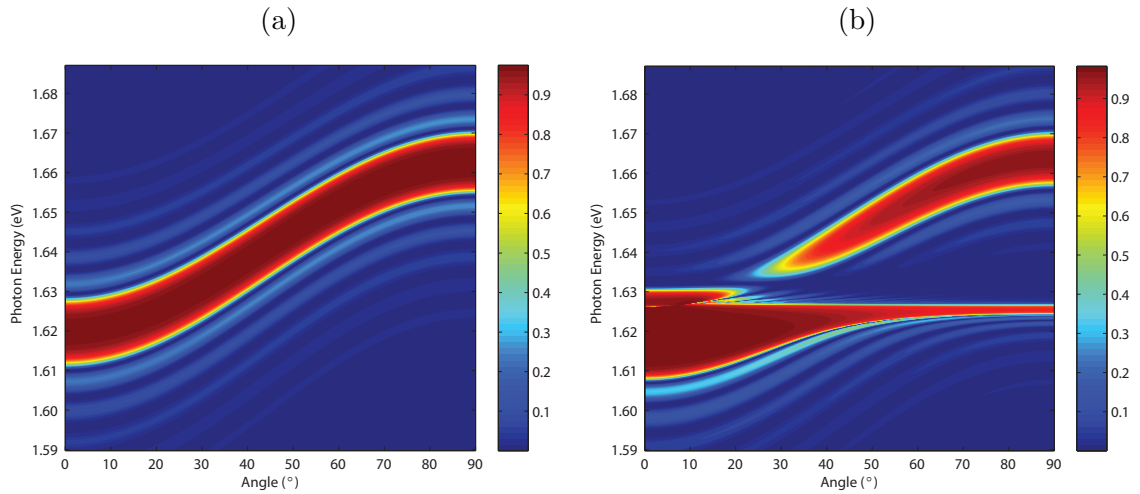

Figure 3.5: (a) Dispersion of a PC with $\Delta n = 0.3$. (b) Dispersion of an RPC with a background $\Delta n = 0.3$.

3.4 Bloch–Polaritons

3.4.1 Introduction

Modification of the optical properties of emitters by confining the emitted electromagnetic field in structures such as microcavities and photonic crystals (PCs) have been studied extensively in the past. Another method of manipulation of optical properties is based on the possibility of coherent radiative coupling between a collection of emissive species. R. H. Dicke showed [16] that if the spacing between the emitters was much smaller than their emission wavelength, the emitters became coherently coupled by the common radiative field. As a result, new collective states are formed with one of them exhibiting the effect of super-radiance. A similar phenomenon can also be realized when the emitters are arranged periodically in a uniform dielectric back-

ground or vacuum with the period equal to half of the emission wavelength [17]. In this geometry, the radiative enhancement is due to the Bragg resonance and has been observed in optical lattices of cold atoms [25] and their semiconductor analog – Bragg multiple-quantum-well (MQW) structures with negligible dielectric contrast [18]. If the number of periods of such a structure exceeds certain value, the character of the light-matter interaction further changes, transforming the super-radiant mode into a photonic bandgap [19, 26]. More recently, similar effects have also been observed in quasi-periodic structures [27].

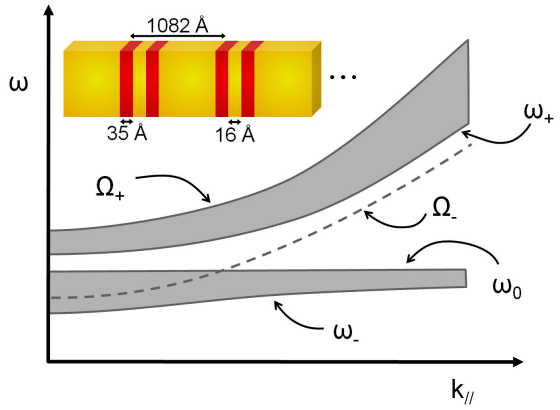

Figure 3.6: The dispersion diagram for a Bragg MQW structure when the excitonic frequency (ω_0) lies between the two PC band edges (Ω_+ and Ω_-) at normal incidence. The coherent interaction between the excitons and the PC Bloch modes results in a modified photonic band structure consisting of two bandgaps whose lower frequency band edges (ω_+ and ω_-) anticross. The inset shows a schematic of the Bragg MQW structure used in the present study. The structure consists of 70 periods of a double-quantum-well (DQW) basis with 35 Å thick $GaAs$ quantum wells separated by a 16 Å $Al_{0.22}Ga_{0.78}As$ barrier. A 996 Å thick $Al_{0.22}Ga_{0.78}As$ barrier separates each pair of the DQWs, resulting in a structure with a period of 1082 Å.

In the case of Bragg MQW structures, the interaction between the excitons and their emitted photons form hybrid excitations, called exciton-lattice-polaritons (ELPs).

If one replaces vacuum photons with Bloch modes of a PC as mediators of radiative coupling between excitons, the properties of resulting Bloch-exciton-lattice-polaritons (Bloch-ELPs) will significantly change. The combination of the PC effect with the ELP effect provides two powerful tools to control the light-matter interaction. Similar control can be implemented in other systems such as atomic lattice and organic materials, where coherently coupled emissive species can be made to interact with an underlying PC. Although theoretical consideration of such systems have been explored in detail [21, 24, 28–31], much less experimental work has been carried out in this context [32, 33]. In the presence of two excitonic species (heavy-hole and light-hole excitons, in our case), the radiation may coherently couple to both of them, producing exotic hybrid polariton states that has contributions from two material excitations and the photon. The hybrid and collective nature of these polariton states, along with their dispersive properties, make them attractive for slow-light enhanced nonlinear optical applications and for studying macroscopic coherence in solid-state systems [30, 34–38].

What is presented here is the first experimental observation of coherent interaction between two excitonic lattices and a PC. Interaction between the PC and a single excitonic lattice manifests itself as a combination of two effects: (i) anticrossing of the exciton mode and the *lower* frequency band edge mode of the PC, and (ii) the formation of an enhanced PC-polariton bandgap with a propagation band,[24, 28, 29] as shown schematically in figure 3.6. In the presence of a second excitonic resonance,

the interaction is further modified, resulting in a second anticrossing between this excitonic mode and the modified low frequency bandedge. This results in the formation of an even larger hybrid bandgap with a second propagating mode. Experimentally, this is demonstrated using angle dependent reflectivity measurements carried out on a 70 period $GaAs/Al_{0.22}Ga_{0.78}As$ MQW structure with a refractive index difference of 0.22. Schematic drawing of the structure is shown in the inset of figure 3.6. Details of the structure investigated is discussed in section 3.4.2. The period of the structure is such that the excitonic lattice formed by *light-hole* (lh) excitons is in the proximity of the band-gap of the PC. The modification of reflectivity, however, was observed also in the vicinity of *heavy-hole* (hh) excitons. These observations are interpreted in terms of coherent coupling between the excitonic lattice of MQW and PC and formation of hybrid Bloch-lh-hh-ELPs. The experimental results are complemented by theoretical modeling of the structure under investigation using a coupled oscillator model [39] and the more rigorous formalism developed in references [21, 29].

3.4.2 Design Structure and Characterization

The Bragg MQW sample studied in the present work was grown using solid-source molecular beam expitaxy and consisted of 70 periods of a double-quantum-well (DQW) basis consisting of 35 Å GaAs QWs separated by 16 Å $Al_{0.22}Ga_{0.78}As$ barrier. This thin barrier causes the hybridization of excitons in the adjacent QWs, resulting

in splitting of lh- and hh-excitons into two doublets [40, 41]. Temperature dependent photoluminescence (PL) measurements were carried out on a single DQW structure to identify the excitonic resonances. The dispersion of the exciton energies are shown in figure 3.7.

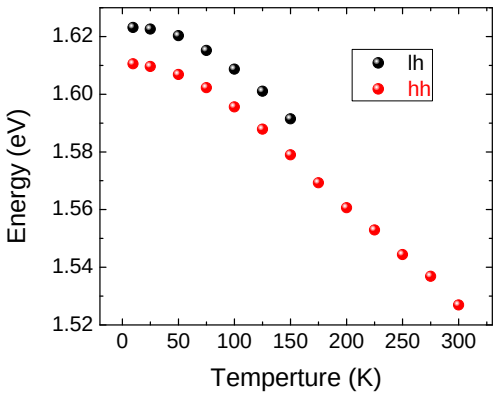

Figure 3.7: Temperature dependent dispersion of the two excitons energies (lh–*light-hole*, hh–*heavy-hole*) observed in the MWQ structure. The dispersion shows a nearly parabolic dependence.

In the Bragg structure, the DQWs are separated from each other by a 996 Å $Al_{0.22}Ga_{0.78}As$ layer. The concentration of Al in the barriers was chosen to create a structure with a non-negligible refractive index difference of 0.22 giving rise to the PC aspect of the structure, while maintaining the contribution from the excitonic lattice introduced by the periodic arrangement of QWs.

Measurements were carried out with the sample placed inside a temperature controlled closed cycle cryostat. A tungsten halogen lamp was used as the light source in the reflectivity measurements, and an Argon ion laser (488 nm) was used as the

excitation source in PL measurements. A CCD based fiber coupled spectrometer was used to collect the optical signal in both the reflectivity and PL measurements. For further details, refer to section 2.2.3.

3.4.3 Theory

We simulated the reflection spectra of our structure using the theoretical approach developed in reference [21] based on non-local treatment of excitons while addressing the exciton-photon interaction that occurs in a system of an excitonic lattice in the presence of refractive index contrast. The effects due to refractive index contrast can be described by introducing an effective exciton susceptibility, S, which has the following form:

$$S = \frac{\Gamma}{\omega - \omega_0 + i\gamma} + \Delta S(\omega), \tag{3.3}$$

where ω_0 and γ are the exciton frequency and non-radiative relaxation rate, ΔS, whose dependence on frequency ω is non-singular, reflects the presence of the index contrast and Γ is effective radiative decay rate of excitons, also modified by the refractive index contrast. The reflection coefficient for the structure with N periods is given by the following formula

$$R_N = \left| \frac{S}{\cot(NKd)\sin(Kd) + i\left(S\cos\phi - \sin\phi\right)} \right|^2, \tag{3.4}$$

where K is the Bloch vector describing electromagnetic excitations of the structure, d is its period, and ϕ is the effective phase of excitations taking into account multiple

reflection from the well-barrier interfaces [21]. As one can see, the reflection spectrum is determined by the form of S and also the Bloch number K, whose properties define the band structure of our system. In the frequency region of interest it is characterized by four bandedges, which are solutions of the following equation [29]

$$(\omega - \omega_0)(\omega - \Omega_+)\left[(\omega - \omega_0)(\omega - \Omega_-) - \frac{\Delta_\Gamma^2}{4}\right] = 0, \tag{3.5}$$

where Δ_Γ^2 is an effective coupling parameter proportional to Γ, and Ω_+ and Ω_- are the high and low frequency bandedges of the pure photonic crystal respectively. This equation describes coupling between the exciton and the low frequency bandedge state of the PC, while the high-frequency bandedge state remains uncoupled. These bandedges, two of which anti-cross under the strong coupling condition, form two photonic bandgaps separated by a propagation band.

The results of these calculations can also be used to interpret the Fano like reflectivity spectra (figure **??**b) in the vicinity of the hh-excitons, which interact with propagating Bloch modes of the PC rather than with bandedge states. An approximate expression for reflectivity having a Fano form can be derived from equation 3.3 for the case where the exciton interacts with propagating modes of the PC given by:

$$R_N \approx |R_{PC}|^2 \frac{(\omega - \omega_0 - \Gamma/\Delta S)^2 + \gamma^2}{(\omega - \omega_0)^2 + \gamma^2} \tag{3.6}$$

where R_{PC} is the reflection coefficient of the corresponding PC structure. This expression is valid in the limit $R_{PC} \ll 1$, which is a reasonable assumption in the region of propagating Bloch wave.

However, in order to explain the spectra in the region of coupled lh-hh excitation, the theory of reference [21] should be modified to include the presence of the second excitons. This can be done by adding a second resonance term in the effective susceptibility (equation 3.3). This approach was used to simulate the reflectivity spectra in figure 3.10. We also fit the experimental data to a three coupled oscillator model. By doing so, we obtain values for the exciton parameter $\Gamma = 17.9$ μeV, corresponding to a coupling strength of 4.3 meV for the lh-excitons, and $\Gamma = 37.5$ μeV for the hh-excitons which corresponds to a 6.2 meV coupling strength.

3.4.4 Results

Reflectivity

Results of angle dependent reflectivity measurements at 10K are shown in figure 3.8a. For large angles, where the excitons are detuned from the Bragg peak, a small exciton related feature consisting of a peak and a dip is visible in the vicinity of the frequency of the hh-exciton, as shown in figure 3.8c. The excitonic nature of this feature at large angles ($> 40°$) is confirmed by its Fano-like asymmetric shape, which is characteristic of electromagnetic Bloch modes scattering off excitons. We do not observe a similar feature at the position of the lh-exciton, which can be explained by its smaller oscillator strength. However, we do see a significant increase in the reflectivity accompanied by a change in the shape of the reflection band when the

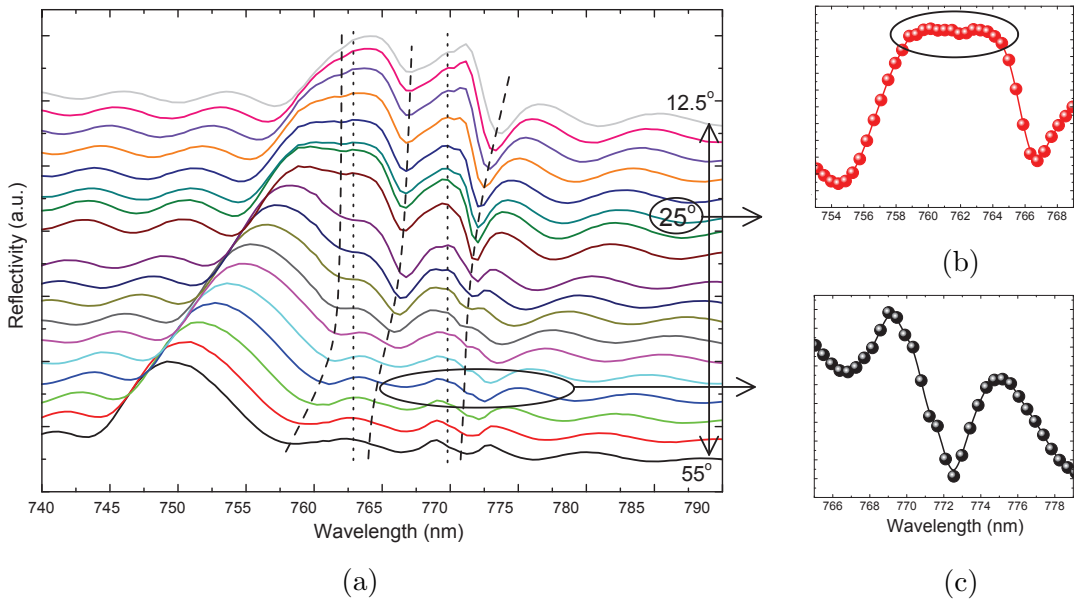

Figure 3.8: (a) Reflectivity for varying angle of incidence starting from 12.5° (top curve), and increasing by increments 2.5° until 55° (bottom curve). The two vertical dotted lines indicate the spectral position of the two excitons and the three dashed lines identify the coupled exciton lattice polariton features that appear as dips in reflectivity. Expanded views showing three notable spectral features in reflectivity: (b) Formation of a lh-ELP bandgap at 25° with the gap having flatter top and steeper edges. In addition, there is a shallow dip present in the middle of the bandgap which is characteristic of the coherent interaction between the excitons and the PC Bloch modes. (c) Fano-like asymmetric spectral feature observed at the hh-exciton frequency when the Bragg peak is sufficiently detuned. coupling.

PC bandgap moves closer to the lh-excitonic frequency. At 25° we observe the modified bandgap formed by the Bloch-lh-ELPs. This bandgap is much flatter, wider, and has steeper edges compared to a pure PC bandgap (figure 3.8b); in addition, it has a shallow dip inside it. This dip, which is clearly seen, despite being smeared by non-radiative linewidth of excitons, is a manifestation of the Bloch-lh-ELPs. At even smaller angles the low frequency bandedge of this modified bandgap interacts

with the hh-excitons, resulting in a strong enhancement in reflection in its spectral vicinity forming a hybrid Bloch-lh-hh-ELP bandgap. For angles between 12.5° and 27.5°, another much more pronounced dip between the lh- and hh-exciton frequencies is observed. It has a slow dispersion, indicative of the photon-lh-hh-exciton hybrid composition of this state. The dispersion of the bandedge features observed in angle dependent reflectivity measurements along with theoretical fits obtained using a coupled oscillator model [39] is shown in figure 3.9a. Three polariton branches, accompanied by two anticrossings are observed with the first anticrossing occurring approximately at 45° between the long-wavelength edge of the PC bandgap and the lh-exciton. The second anticrossing is observed around 25° in the vicinity of the hh-exciton. Estimated strength for the interaction between the excitons and the photons are 4.3 meV and 6.2 meV for the lh- and hh-excitons, respectively.

Coupled Oscillator Model

Contributions from the *lh*, *hh*, and photonic components are obtained by fitting the experimentally observed dispersion to a three coupled oscillator model, and are shown in figure 3.9b. The coupled oscillator model is based on the solutions to the eigenvalue problem shown in equation 3.7. The 3×3 matrix is the Hamiltonian of the coupled systems (photons and heavy/light excitons), and coefficients represent the contributions each of the particle constituents. The solution yields three polariton energies, E_{UB}, E_{CB}, and E_{LB}, corresponding to the upper, central, and lower

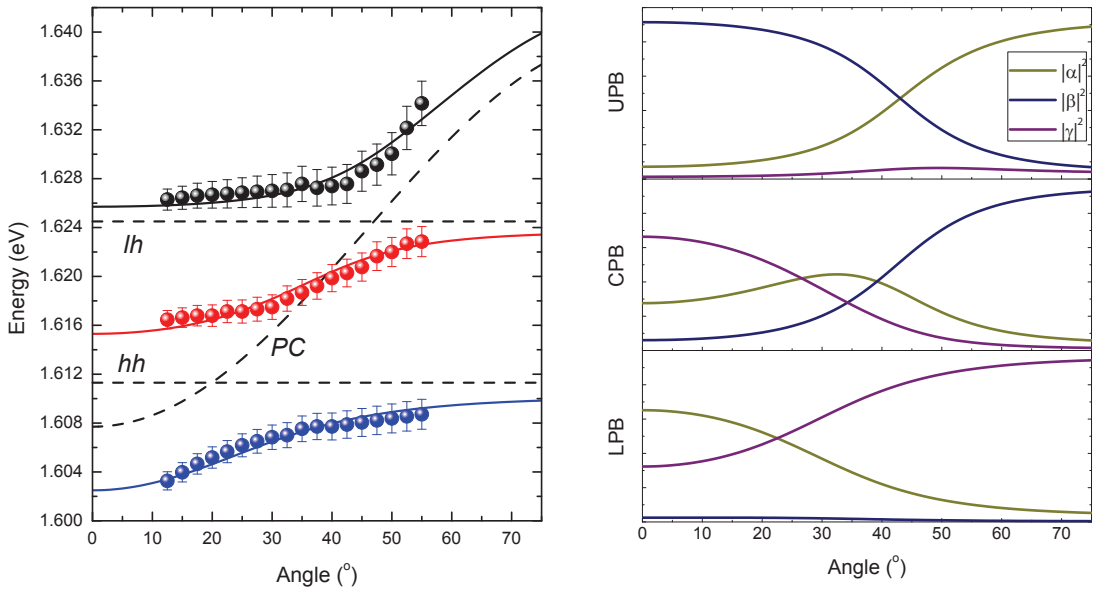

(a) (b)

Figure 3.9: (a) Resonant dips observed in reflectivity plotted as a function of angle indicates the presence of three polariton branches exhibiting characteristic anticrossing behavior. The solid lines are fits obtained using a three coupled harmonic oscillator model yielding exciton-photon interaction strengths of 4.3 meV and 6.2 meV for the lh- and hh-excitons, respectively. The dashed lines correspond to the bare exciton frequencies. (b) Mixing coefficients calculated using the coupled oscillator model shows the photonic ($|\alpha|^2$), lh ($|\beta|^2$) and hh ($|\gamma|^2$) excitonic contribution to the upper, central, and lower polariton branches (labeled UPB, CPB, and LPB, respectively). At 35°, the CPB shows maximum mixing between the excitons and the photons and the coefficients are calculated to be $|\alpha|^2 = 0.4$, $|\beta|^2 = |\gamma|^2$=0.3.

branches, respectively. The central polariton branch in the dispersion diagram can be interpreted as having contributions from all three components, while the upper and lower polariton branches have contributions primarily from the photons and one of the excitonic species. At 35°, the central polariton branch has approximately 30% contribution from each of the excitonic species, and 40% from the photons. This

demonstrates the formation of a hybrid Bloch-lh-hh-ELP.

$$\begin{pmatrix} E_{ph} & V_{ph-hh} & V_{ph-lh} \\ V_{ph-hh} & E_{hh} & 0 \\ V_{ph-lh} & 0 & E_{lh} \end{pmatrix} \begin{pmatrix} \alpha \\ \beta \\ \gamma \end{pmatrix} = E \begin{pmatrix} \alpha \\ \beta \\ \gamma \end{pmatrix} \tag{3.7}$$

The calculations for fitting the polariton branches to a three-coupled oscillator model were carried out in MATLAB and the codes used are included in appendix D.

Discussion

In addition to the coupled oscillator model, the dispersion characteristics of the polariton branches were calculated using the rigorous theoretical model developed in reference [21] (see section 3.4.3).

The results of these calculations, together with the experimental dispersion are shown in figure 3.10. At large angles, when the PC bandgap is significantly detuned from the excitonic resonances, the bandedges follow the expected Bragg dispersion. At smaller angles ($35^\circ - 45^\circ$), the low frequency bandedge strongly couples with the lh-excitonic lattice, resulting in the anticrossing between these modes, along with the formation of the Bloch-lh-ELP bandgap. At even smaller angles ($< 35^\circ$), the low frequency bandedge of the modified bandgap interacts with the hh-excitonic lattice. This results in the formation of Bloch-lh-hh-ELPs with its associated anticrossing and an additional propagation band inside a now further enhanced bandgap.

Although the theoretical estimates derived from experiments of the non-radiative

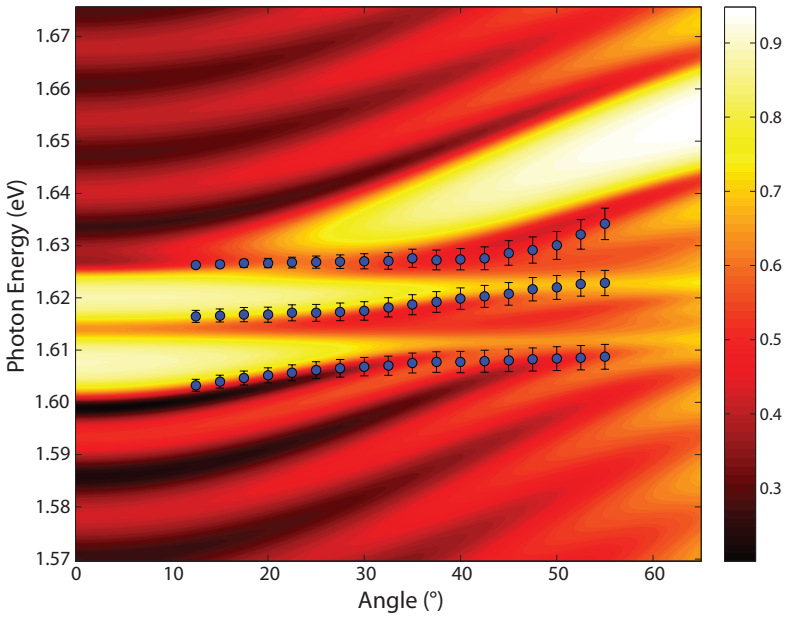

Figure 3.10: (a) Calculated reflectivity at 10K for various angles of incidence with only lh-exciton taken into account following the theoretical formulation of reference [21]. The vertical dotted lines indicate the position of the lh and hh-excitons. Anticrossing is observed between the two low frequency bandedges at 40°. It is also observed that the low frequency edge of the modified bandgap crosses the hh-exciton frequency at 25°. (b) Reflectivity calculations performed for exciton non-radiative relaxation rates varying from 0 to 25 meV at a fixed angle of 20°. As the relaxation rate increases, the sharp propagating band observed in the middle of the enhanced stop-band becomes shallower. Based on the fits to experimental data, we estimate the exciton non-radiative relaxation rate to be 4.5 meV.

lifetime (4.5 meV) and the interaction strength (4.3 meV) are comparable, the observation of anticrossing and the formation of the propagation band confirms our assertion that we indeed have observed strong coupling between the excitonic lattice and PC Bloch modes.

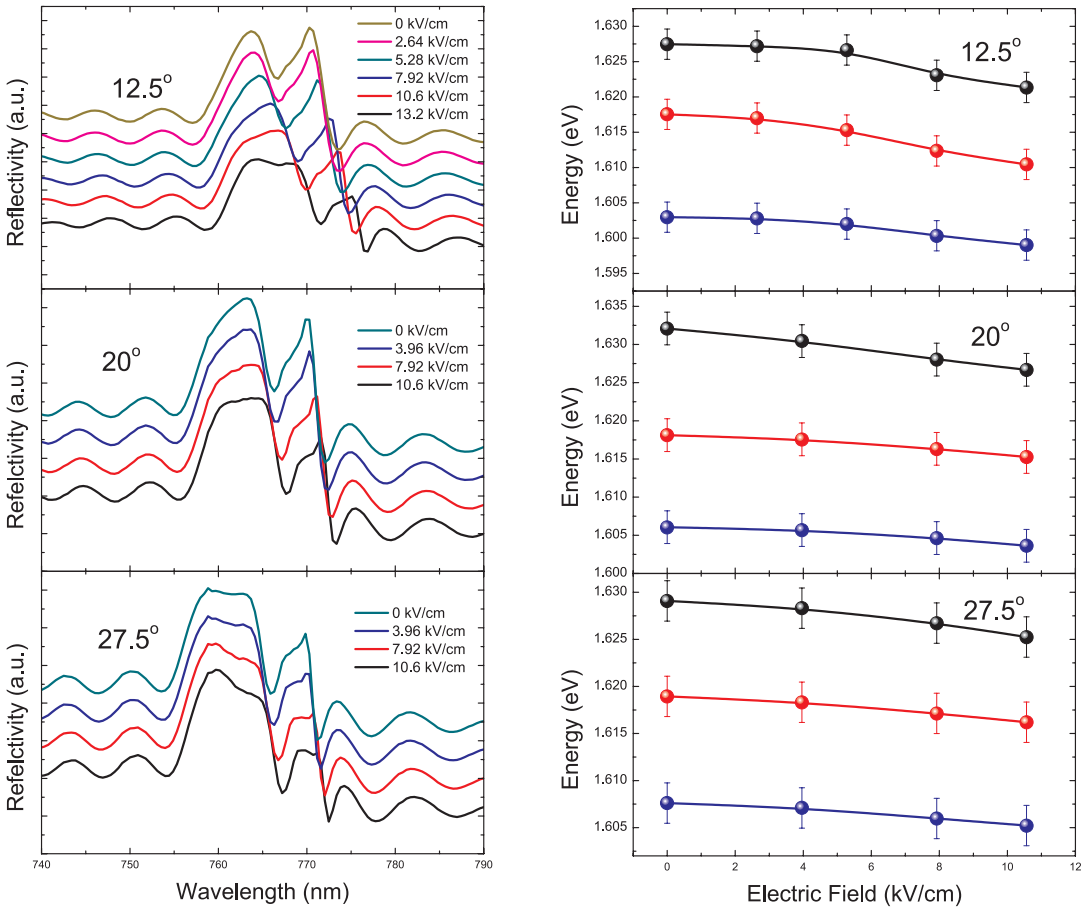

(a) (b)

Figure 3.11: (a) Demonstration of polariton tuning using electric field for reflectivity measurements at 12.5°, 20°, and 27.5°. At 12.5°, the top curve shows the reflection spectrum with no electric field. With increasing electric field (lower curves), we are able to manipulate the polaritonic nature of the central branch by decreasing its hh-excitonic component and increasing its photonic and lh-excitonic components. At 20°, a similar tunability is possible where the hh-excitonic component becomes comparable to the photonic component. For a slightly greater angle of 27.5°, it is now possible to tune the contributions such that the two excitonic species play equal roles. In addition, large changes in reflectivity are observed. (b) Dispersion of the three polariton branches as a function of electric field. Error bars correspond to the standard deviation of polariton energies.

Effects of Electric Field

An important advantage of the considered structures is the possibility to manipulate the optical properties by tuning the excitonic frequency; for instance, using an electric field. In order to enhance this property, we designed our structures with double-quantum well basis taking advantage of enhanced quantum confined Stark effect in double well structures [42]. In the presence of an electric field, excitonic resonances shift to longer wavelength – thereby altering the interaction strength of the excitons and the Bloch modes which also alter the reflectivity profile. We show the reflectivity spectra obtained with varying the electric field at three different angles in figure 3.11a and the corresponding dispersion of these polaritons in figure 3.11b. Besides tuning the polariton contributions, we also observe significant change in reflectivity ($\sim$100%). Since these large changes in reflection can be induced by varying electric field as well as angle of incidence, which transitions the system between the strongly coupled regime, and the weakly regime, such systems can be useful for optical switching applications.

3.4.5 Conclusion

In summary, we demonstrate coherent interaction between PC bandedge photons and excitons of the excitonic lattice. This is inferred from the significant reconstruction and enhancement of the reflection spectrum when the stop-band of the underlying

PC moves across the lh-excitonic frequency. A large enhancement of reflectivity is observed when the low frequency edge of the modified bandgap crosses the hh-exciton frequency. This increase in reflectivity is accompanied by a dip between the lh- and hh-exciton frequencies. These effects are explained by coupling between hh-excitons and Bloch-lh-ELP, which results in formation of a new bandgap in the vicinity of hh-excitons, and hybrid Bloch-lh-hh-ELP propagating excitations responsible for the dip in reflectivity. In addition, we show the tuning of coherent interaction between the excitons and the Bloch modes of the PC using an electric field. The unique dispersion of these polaritons, (the central branch in particular) can be exploited for slow-light enhanced nonlinear optics due its shallow dispersion. Furthermore, the collective nature of the hybrid excitations demonstrated here, open up the possibility to observe macroscopic coherence phenomena in solid-state systems.

Chapter 4

Colloidal Quantum-Dot Clusters

4.1 Motivation

In section 3.2, excitons in a one-dimensional lattice were found to exhibit collective behavior due to their periodic spacing under the Bragg condition ($\lambda/2$ emission wavelength). These effects are due to the coherence under the phase matching condition. Dicke "superradiance" is a coherent emission from dipole active atoms that are closely spaced, $d \ll \lambda$, where d is the distance between the particles [16]. In addition to the constraint of the interparticle distance, the physical dimension of the entire ensemble must also be less than than order of the emission wavelength. Under these conditions, all the particles in the ensemble emit coherently under a common radiation field. This yields a greatly enhanced emission intensity in addition to an enhanced radiative rate such that $\Gamma = N\Gamma_0$, where N is the number of particles in

the ensemble, and Γ_0 is the radiative rate of a single emitter. In this chapter, cluster of self-assembled colloidal quantum dots linked with DNA will be studied in this context.

4.2 Synthesis

Nanoparticle self-assembly has been of great interest in recent years [43–51]. In particular, there has been much work carried out using DNA linker for the nanoparticles [43–45, 47, 48, 52–54]. In a study carried out in collaboration with Gang's group at the Center for Functional Nanomaterial at Brookhaven National Laboratory, colloidal quantum dot (QD) self-assemblies were fabricated and optically characterized. The role of Gang's group was limited to the synthesis of the QD clusters. A schematic of the QD cluster is shown in figure 4.1.

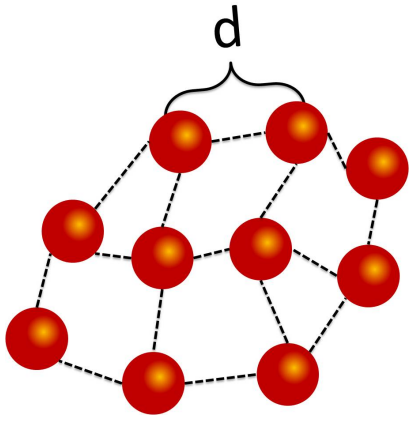

Figure 4.1: Schematic of the QD cluster linked together by DNA linkers of a predetermined length. The distance between the QDs, d, is set by the linker used.

The synthesis involves adding strands of DNA to the colloidal water based suspension of CdSe/ZnS (core/shell) QDs where the DNA attaches to the surface of the QDs. DNA linkers are then added to the suspension which link two QDs together by each end attaching to the DNA on a QD. As the process continues, clusters of QDs form where the distance between the QD is determined by the length of the linker. This method was used successfully to make a gold nanoparticle three-dimensional superlattice [53, 54].

4.3 Time-Resolved Photoluminescence

There were two cluster samples prepared for this study: one a short linker ($\sim$30 nm) denoted by $L30$, and a longer linker ($\sim$60 nm), denoted by $L130$. A reference sample was prepared as well, containing no linkers, making it a simple QD suspension. The lifetime measurements were carried out using a time-correlated single photon counting setup. A 467 nm pulsed diode laser with a pulse with of < 200 ps was used as the excitation source (see section 2.2.4 for further details). A sample comparison of the time-resolved photoluminescence (PL) collected at the steady-state emission peak (605 nm) is shown in figure 4.2a. The figure shows that the lifetime does indeed decrease slightly as the QD spacing decreases.

After repeated measurements, however, the statistics show that there is no observable change in lifetime among all the samples. Time-resolved PL was collected a

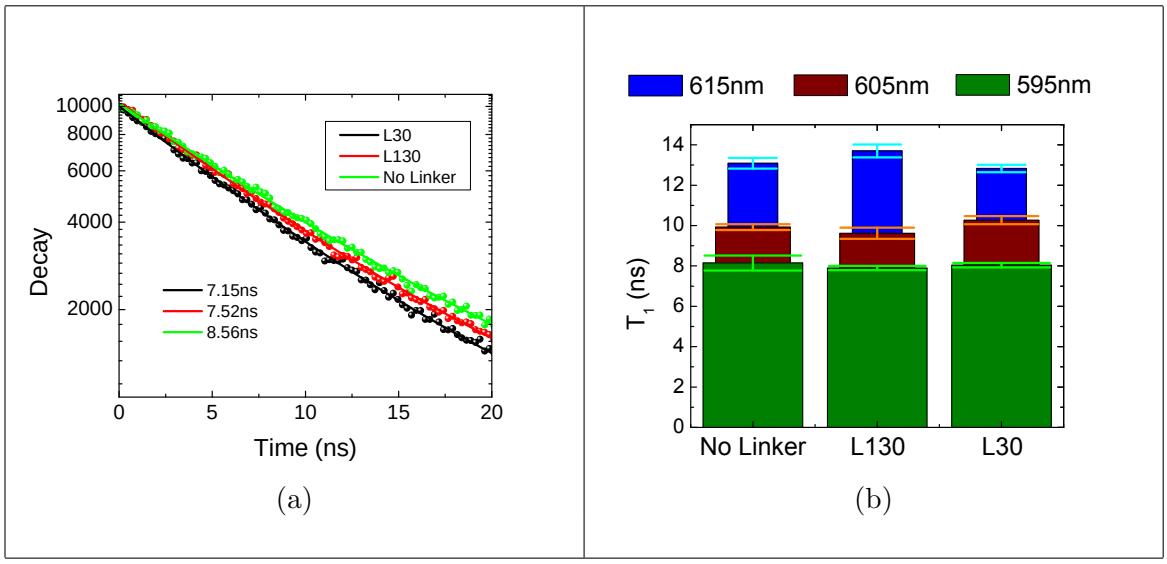

Figure 4.2: (a) Time-resolved PL for the two cluster samples and the reference. A slight decrease in lifetime is observed with decrease QD spacing. (b) Statistical mean of the lifetimes of the of the three samples show no clear trend. The error bars represent the standard deviation of five PL measurements.

total of five times for each sample, at the steady-state PL emission peak, and ±10 nm from the peak. The measurements show an increase in lifetime for longer collection wavelengths, which is typical for these kind of QDs due to the size dependence of oscillator strength [55]. The resulting lifetimes are shown in figure 4.2b with error bars representing the standard deviation of the lifetimes, showing no clear tend in the lifetime with respect to QD spacing.

4.4 Steady-State Photoluminescence

We carried out steady state PL measurements to look for possible explanations for the lack of radiative enhancement observed in time-resolved PL experiments. Using

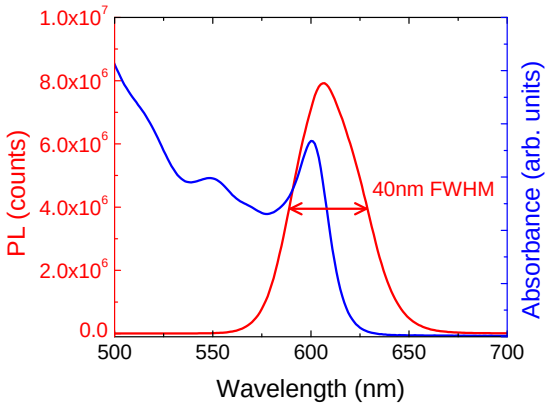

Figure 4.3: Steady state PL and absorption spectra of the QDs without linkers. The PL spectrum shows a a broad width (FWHM $\sim$ 40 nm), due to inhomogeneous broadening.

a white light source to excite the "no linker" sample at a wavelength of 400 nm, the PL peak is found to be at 605 nm. However, the full-width half-maximum (FWHM) is 40 nm. The steady-state PL is shown together with the absorption spectrum in figure 4.3. This width indicates a large amount of inhomogeneous broadening in the QDs. One of the conditions for superradiance is that the particles need to be close to each other, $d \ll \lambda$. The particles considered need to be co-resonant, i.e., have the same resonant frequency. In the samples dealt with in this study, the particles are sufficiently close; however, the inhomogeneous broadening greatly reduces the probability that co-resonant QDs will be linked directly together. This alone is enough to interfere with the superradiant effect. Furthermore, dynamic light scattering measurements estimate the cluster size to be 300-500 nm large. The cluster size is on the same order of magnitude as the resonant wavelength, therefore, the

photons emitted from one QD will not be in phase with the photons emitted from a distant QD, therein spoiling the superradiance further.

4.5 Conclusions

Two samples containing clusters of colloidal QDs were linked with DNA and were investigated for signs of coherent radiative coupling. Numerous time-resolved PL measurements were carried out and the statistics showed no evidence of radiative enhancement. Steady-state PL indicate that there is large inhomogeneous broadening of the QDs which is detrimental to coherent radiation. Furthermore, dynamic light scattering measurements indicate that the cluster size is on the order of magnitude of the emission wavelength. Meaning photons emitted from one QD would not be in phase with a an emitted photon of a distant QD. Colloidal QDs with large inhomogeneous broadening in not a good choice of emitter for superradiant emission. In order to observe coherent emission in QD clusters, the inhomogeneous broadening needs to be small, and the cluster size should be smaller than the wavelength.

Part II

Quantum-Dots in Planar Microcavities

Chapter 5

Single-Cavity Structures

5.1 Introduction

Microcavity structures (MCs) have been of great interest in recent years owing to their ability to create large optical intensities within the structure. The physics of MC structures can be thought of in two ways:

1. A photonic crystal (PC) with a ($\lambda/4$) defect.

2. A Fabry-Perot resonator using distributed-Bragg-reflectors[1] (DBRs) as mirrors.

Thinking of MCs as PCs with a defect is analogous to semiconductor physics where electronic states arise in a bandgap due to a defect in the crystal. As will be shown

[1]Distributed-Bragg-reflectors are one dimensional multilayer structures consisting of pairs of two optically differing materials resulting in a structure with photonic bandgap centered at wavelength, $\lambda = 2d$, where d is the optical thickness of the pair. DBRs have reflectance related to the number of pairs, N, where a half-integer number of pair refers to a structure terminating with the the first layer of the pair. The greater N, the higher the reflectance.

below, a similar defect state appears in PCs with a defect. Although this mode of thought is useful, and can lead to interesting insight in more complicated structures (see chapter 6), the latter description is used more widely because the applications of such structures are similar to well known laser cavity systems, and therefore it is convenient to use the same language.

A schematic of the one dimensional microcavity considered in this work is shown in figure 5.1a. The reflectance of such a structure exhibits a photonic bandgap with a narrow transmission window (defect state). Figure 5.1b shows the reflection spectrum of a MC with 20.5 pair bottom DBR, $\lambda/2$ cavity, and 19.5 pair top DBR. The refractive index of the bilayers was set to 1.77, and 1.45 corresponding to SiO_2 and Si_3N_4, respectively. The reflectivity calculations for this structure were carried out in MATLAB software and the code is included in appendix B.

In addition to the spectral location of the MC resonance, it is important to know how the optical field intensity is distributed within the structure. At the resonance of the MC the electric field intensity exponentially grows within the structure, and peaks at the center of the cavity, where after it exponentially decreases to the end of the structure. An example of this behavior, where the field intensity increases by a factor of $\sim$150, is shown in figure 5.2a. This behavior is only on resonance, where the large optical density exists in the transmission window shown in figure 5.1b. The optical intensity in the structure as a function of wavelength is shown in figure 5.2b. The MATLAB code for the electric field intensity profiles are included in appendix C.

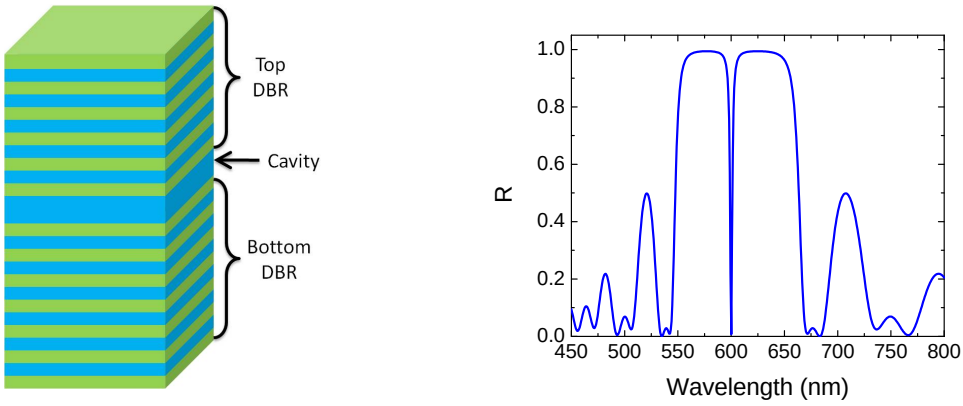

(a) (b)

Figure 5.1: (a) Schematic of the microcavity structure consisting of a bottom and top DBR, separated by a cavity (defect) layer. (b) The normal incidence reflectivity of a MC consisting of a 20.5 pair, and 19.5 pair SiO_2/Si_3N_4 ($\text{layer}_2/\text{layer}_1$) bottom and top DBR (600 nm center wavelength), respectively. The two DBRs are separated by a $\lambda/2$ thickness cavity layer. The entire structure is set on a silicon substrate.

5.2 Motivation

It is well known that modifying the optical environment surrounding a light emitter alters its emission properties [56]. In this context, microcavities have been used extensively to modify spontaneous emission rates from a variety of emitters [57–61]. The optical field in the cavity is enhanced by constructive interference, and the strength of the enhancement is typically quantified by quality factor (Q). In the past, there has been much success with structures fabricated using molecular beam epitaxy (MBE) and metalorganic chemical vapor deposition (MOCVD) techniques [60, 62, 63]. While

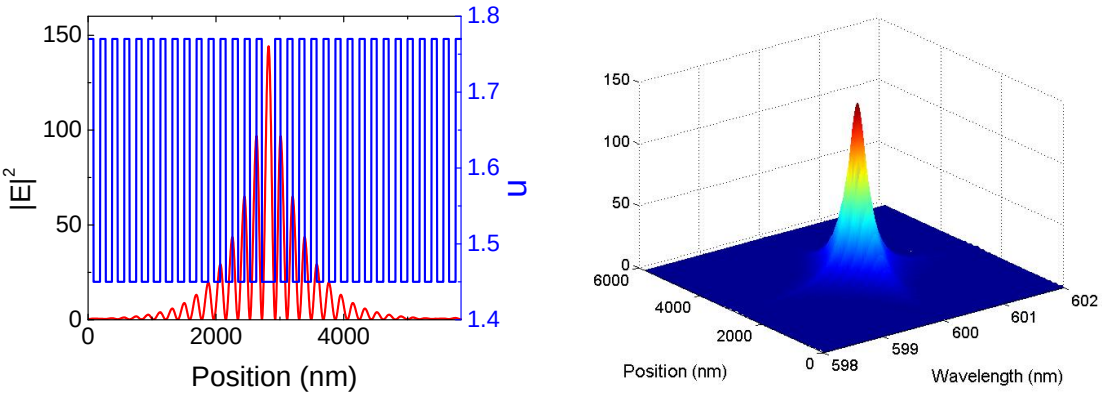

(a) (b)

Figure 5.2: (a) Schematic of the microcavity structure consisting of a half wavelength thick QD layer (red) sandwiched between a ten pair bottom DBR and a nine pair top DBR. The DBRs consist of alternating layers of Si_3N_4 and SiO_2. The structure is deposited on a glass substrate (not shown). (b) The normal incidence reflectivity of the MC is plotted together with the PL spectrum of a solution of CdSe/ZnS core-shell QDs in toluene.

the quality of the semiconductor structures fabricated using these techniques are high, the process is complex, and expensive. A simpler and cost effective method is to use dielectric materials for the structure, while incorporating a semiconductor material in the cavity to serve as an active medium. Colloidal semiconductor quantum dots (QDs) are a viable option for the optically active medium. These QDs are synthesized using low-cost wet chemistry techniques, and can be spectrally tuned by varying their size. The challenge however has been to incorporate colloidal QDs into photonic structures without affecting their optical properties using standard microfabrication techniques.

Whispering-gallery-mode (WGM) lasing from colloidal QDs has been demon-

strated using a wide variety of structures such as microspheres, and microrings [59, 64, 65]. However, WGM geometries typically result in multi-mode lasing and require precise tapered fiber coupling and hence cannot be monolithically integrated. Much work has been carried out on one dimensional microcavity systems [66–71]. Lasing has also been reported using an all polymer microcavity structure realized via spin coating [71]. However, it is difficult to realize polymer layers thinner than $\sim$100 nm via spin coating, and the polymer structures also suffer from long term stability issues. Very recently, lasing from pyramidal shaped colloidal QDs have been reported in a wedge sandwich-like structure where the QDs were drop-coated between two pre-fabricated reflective surfaces and held together with mechanical pressure [72]. Monolithic microcavity structures are highly desirable for integrated photonic systems. Although there have been reports using monolithic all-dielectric microcavity structures for mode confinement [69], and enhanced photoluminescence (PL) from colloidal QDs [66], there have not been any reports of enhancement of gain using such systems. Here we report enhancement of gain from colloidal QDs in a monolithic all-dielectric one dimensional microcavity that can easily be scaled to different resonant wavelengths.

5.3 Spin-Coated Quantum Dots – Low Concentration Regime

5.3.1 Fabrication Methods

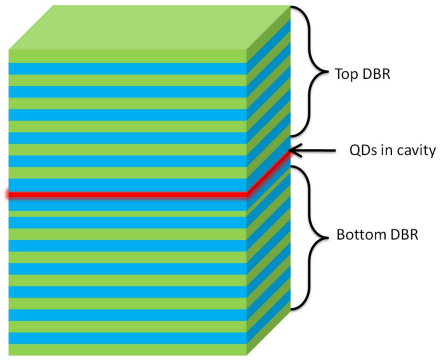

Figure 5.3: Schematic of a MC structure with QDs incorporated in the cavity layer. The cavity consists of three layers in total: (1) An SiO_2 layer with thickness slightly less than $\lambda/4$. (2) A film of spin coated QDs. (3) A capping layer of SiO_2 with thickness slightly less than $\lambda/4$. The reason for layers (1) and (3) having slightly less than $\lambda/2$ thickness is to ensure that the entire cavity (including the QD layer) has thickness of $\sim \lambda/2$.

The dielectric layers of the MC structure was fabricated using a plasma enhanced chemical vapor deposition (PECVD) system. The MC consists of two distributed Bragg reflectors (DBRs) separated by a thin layer of CdSe/ZnS (core/shell) QDs. The DBRs consisted of alternating layers SiO_2 and Si_3N_4 of quarter wavelength thickness. The SiO_2 was deposited with a flow of N_2O at 180 sccm and 2% Si_3H_4 diluted in N_2 at 52 sccm, at a pressure of 400 mT. The Si_3N_4 layers was deposited with a flow of N_2 at 180 sccm, NH_3 at 20 sccm, and 2% SiH_4 diluted in N_2 at 88 sccm,

at a pressure of 800 mT. For both layers, the substrate temperature was 180C, and RF power of 100 W. The bottom DBR consisted of 12.5 pairs of Si_3N_4/SiO_2 deposited on a silicon substrate. The cavity layer consisted of a QDs layer sandwiched between two SiO_2 layers yielding an effective $\lambda/2$ cavity length. The QD film was spin coated from a solution of QDs in toluene of 0.1 mg/ml concentration, yielding a QD film of thickness $\sim$ 30 nm. The QD film was spin coated on the bottom DBR and the first SiO_2 cavity layer, and the remainder of the structure was grown by PECVD after the solvent evaporated.

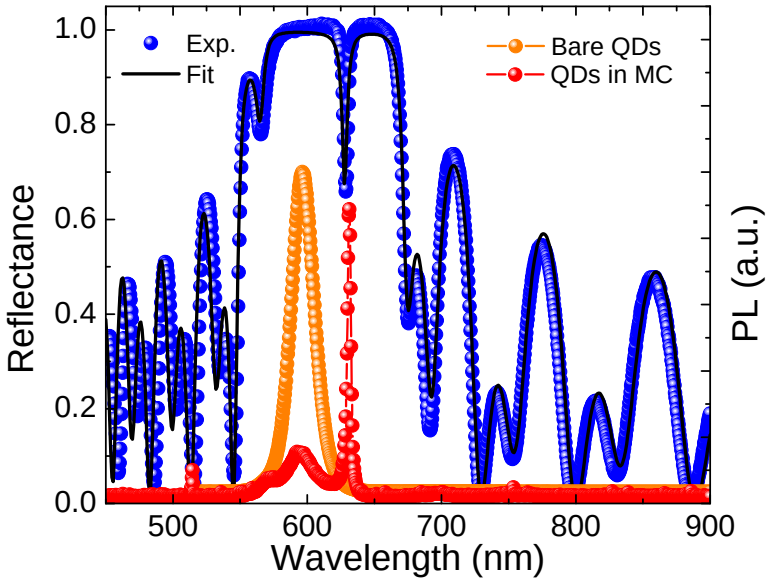

Figure 5.4: (a) Schematic of the microcavity structure consisting of a half wavelength thick QD layer (red) sandwiched between a ten pair bottom DBR and a nine pair top DBR. The DBRs consist of alternating layers of Si_3N_4 and SiO_2. The structure is deposited on a glass substrate (not shown). (b) The normal incidence reflectivity of the MC is plotted together with the PL spectrum of a solution of CdSe/ZnS core-shell QDs in toluene.

The layers deposited on top of the QDs, which include the SiO_2 partial cavity and 11.5 pair DBR, are done at low processing temperature of 180°C in order to preserve the integrity of the QDs. A schematic of the structure is shown in figure 5.3. The reflectivity spectrum of the resulting MC at normal incidence was measured using a tungsten-halogen light source coupled to an optical fiber and was collected using a fiber coupled CCD based spectrometer. The reflectivity spectrum consists of a stop-band with a transmission window centered at 630 nm and a full-width-half-maximum (FWHM) of $\sim$ 4 nm, which spectrally overlaps with tail of the photoluminescence (PL) spectrum of bare QDs, as shown in figure 5.4.

Although the normal incidence reflectivity shows the cavity resonance overlapping with the long wavelength tail of the PL of the QDs, this is often done deliberately. The growth rate during the fabrication process often drifts, and if the MC resonance is red-shifted compared to the the PL peak, it can be tuned into resonance by changing the collection angle, where the cavity dispersion blue-shifts with increasing angle.

5.3.2 Power Dependent Photoluminescence

In order to characterize the MC to determine if there is an amplification of emission, power dependent PL measurements need to be performed. To this end, a continuous wave (CW) argon-ion laser was used as an excitation source for the QDs. Further details of the experiment are described in section 2.2.3.

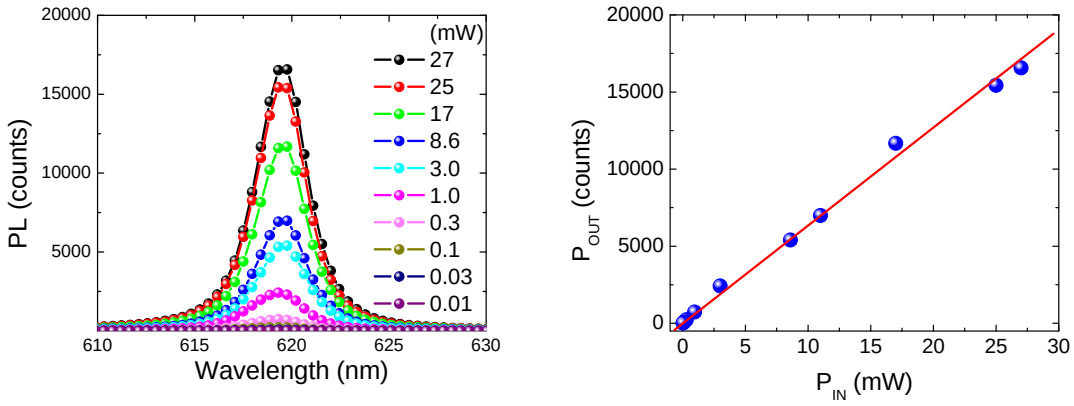

(a) (b)

Figure 5.5: (a) Power dependent photoluminescence under continuous wave excitation showing the increase of the emission intensity with increasing excitation power. Although the intensity increases, there is no observable change in linewidth. (b) The peak power is plotted against the input power clearly showing linear dependence indicating the absence of any threshold behavior.

PL was collected at various pumping intensities up to 27 mW, at a collection angle of ∼20°, where the intensity was found to be maximum. The various spectra are plotted in figure 5.5a. The FWHM of the PL does not narrow with increasing pump intensity. Furthermore, the PL peak intensity increases linearly with pump power, as seen in figure 5.5b.

The effects of the MC on the QDs are clear from the PL spectra. The PL spectra are narrower and more intense for the MC sample compared to the bare QDs, as seen in figure 5.4. However, there is no threshold behavior observed. This is due to the low concentration of QDs in the MC. The spin-coated layer of QDs is ∼30 nm thick, which may not be enough to observe gain in the system. In section 5.5, a different method of depositing QDs is employed to yield films of greater thickness.

5.4 Single–Photon Source

Quantum dots (QDs) in microcavity (MC) structures are a good candidate for single-photon sources. The radiative enhancement that the MCs provide are beneficial in single-photon applications due to the possibility of achieving high bit-rates. In collaboration with Luke J. Bissell of Professor Svetlana G. Lukishova's Photonic Quantum Information Systems Group at The Institute of Optics at the University of Rochester, QDs in an all dielectric MC were characterized for single-photon emission.

5.4.1 Antibunching Experiment

Single-photons exhibit antibunching behavior, i.e., emitted photons are temporally separated. The degree of antibunching is measured by the second-order coherence function, which measures the correlation of photons detected at two different detectors separated in time by time τ [73]:

$$g^{(2)}(\tau) = \frac{\langle \hat{a}^\dagger(t)\hat{a}^\dagger(t+\tau)\hat{a}(t)\hat{a}(t+\tau)\rangle}{\langle \hat{a}^\dagger(t)\hat{a}(t)\rangle^2} \tag{5.1}$$

where $\hat{a}^\dagger$, and $\hat{a}$ are the photon creation and annihilation operators, respectively. Antibunched light has the property that $g^{(2)}(0) < g^{(2)}(\tau \neq 0)$. For pure single-photon emission, $g^{(2)}(0) = 0$, i.e., photons are separated temporally. For coherent light, $g^{(2)}(\tau) = 1$, for all τ, and for bunched light or incoherent sources, $1 \leq g^{(2)}(\tau \neq 0) < g^{(2)}(0)$. The measure of $g^{(2)}(0)$ is an indicator for the purity of the single photon source.

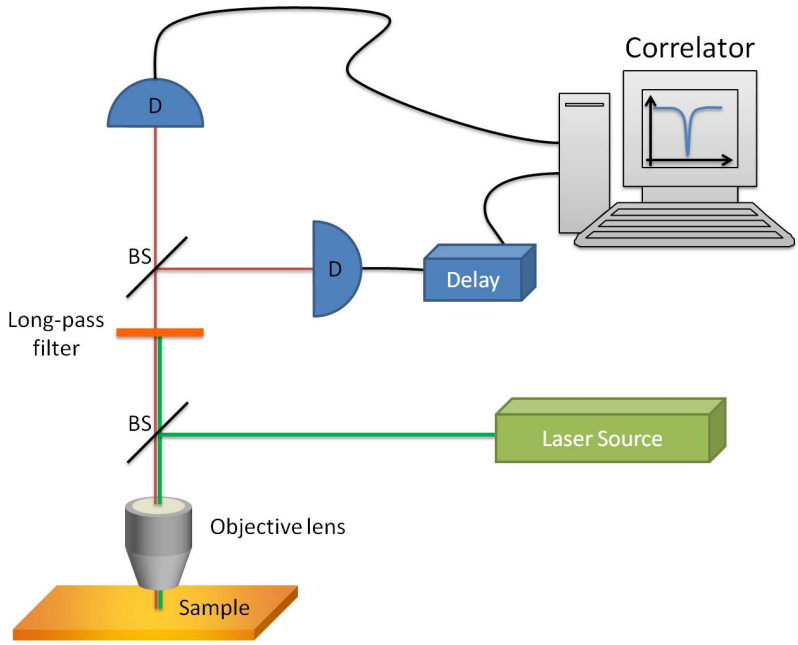

Figure 5.6: Schematic of confocal imaging system used to measure $g^{(2)}(t)$. A laser is used as an excitation source and emission is collected with a microscope objective lens. The laser is filtered out of the signal before impinging on a 50:50 beam splitter where the photons can be detected by two spacial separated detectors.

In order to experimentally measure $g^{(2)}(\tau)$, a Hanbury Brown-Twiss interferometer is used to measure temporal correlations of photons [74]. The setup takes photons from a source and passes it to a 50:50 beam splitter where a detector is placed at each of the two paths. A correlator records the time between the two detectors. A histogram of the interphoton times can then be constructed in order obtain $g^{(2)}(\tau)$ [75, 76]. An electronic delay is usually placed along thepath of one of the detectors in order to measure $g^{(2)}(\tau < 0)$. A schematic of the setup is shown figure 5.6.

5.4.2 Results

A MC structure was fabricated through plasma enhanced chemical vapor deposition (PECVD) (see section 2.1.3 for details), and colloidal quantum dots (QDs) were incorporated in the cavity layer by spin coating (see section 2.1.1 for details). Similar structures have already been discussed in section 5.3. The DBR layers comprised of $\lambda/4$ thickness SiO_2 and Si_3N_4 with refractive index 1.45 and 1.77, respectively. The bottom DBR consisted of 15 pairs of Si_3N_4/SiO_2, while the top DBR consisted of 14.5 pairs of SiO_2/Si_3N_4 (note that the base pair are opposite in the bottom and top DBRs). Separating the two DBRs is a $\lambda/2$ thickness SiO_2 cavity with spin coated QDs in the center. A schematic of the structure is shown in figure 5.7a. The reflectivity spectrum along with the photoluminescence (PL) spectra of bare QDs compared to those inside the MC are shown in figure 5.7b. The MC PL shows a very narrow emission of $\approx$2 nm full-width-half-maximum (FWHM) that aligns with the cavity resonance with a similar FWHM. The spectra shown are from a sample fabricated on a silicon substrate. For the antibunching experiment, an identical structure was fabricated on a thin glass substrate ($\sim$ 1 mm thick) and the QD concentration was chosen to be extremely low in order to increase the probability of isolating single QDs.

The PL from the low QD concentration microcavity was measured using a confocal fluorescence microscope with a 1.35 N.A. objective. The microcavity was excited with light from a pulsed 532 nm laser at a repetition rate of 76 MHz, and a pulse

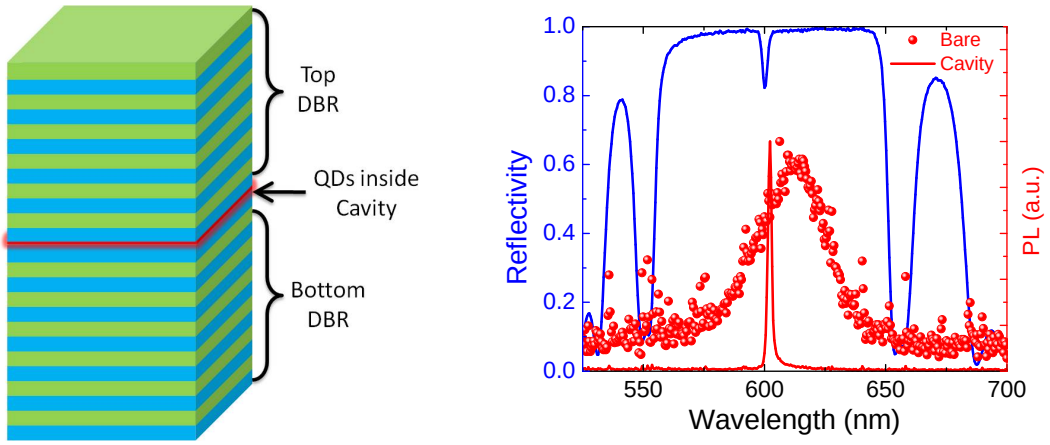

(a) (b)

Figure 5.7: (a) Schematic of the MC similar to the one used for this investigation, showing QDs in the center of the cavity layer. (b) Reflectivity of the MC structure showing a dip corresponding to the resonant wavelength at 600 nm. The PL emission from the QDs in the MC (solid line) shows a narrow linewidth of ∼2 nm corresponding to cavity emission. The PL spectra of bare QDs is shown for comparison (spheres).

width of 6 ps. The peak intensity at the focus of the objective was 6.5 kW/cm^2 with a spot size of 0.5 μm. For further details of the experimental setup, see reference [77]. The confocal fluorescence image shown in figure 5.8a displays multiple areas with low QD density. When single QDs were illuminated to look at the fluorescence autocorrelation, they were found not to be very photostable. For each QD we investigated, photo-blinking was observed, and a steady decrease in the duration and intensity of on-times. The time trace PL intensity of one such single QD is shown in figure 5.8b.

Due to the poor photostability, the coincidence counts histogram of single QDs were too noisy to show any antibunching behavior. However, the sum of six different single QD coincidence count histograms does shows a dip $t = 0$, indicating photon

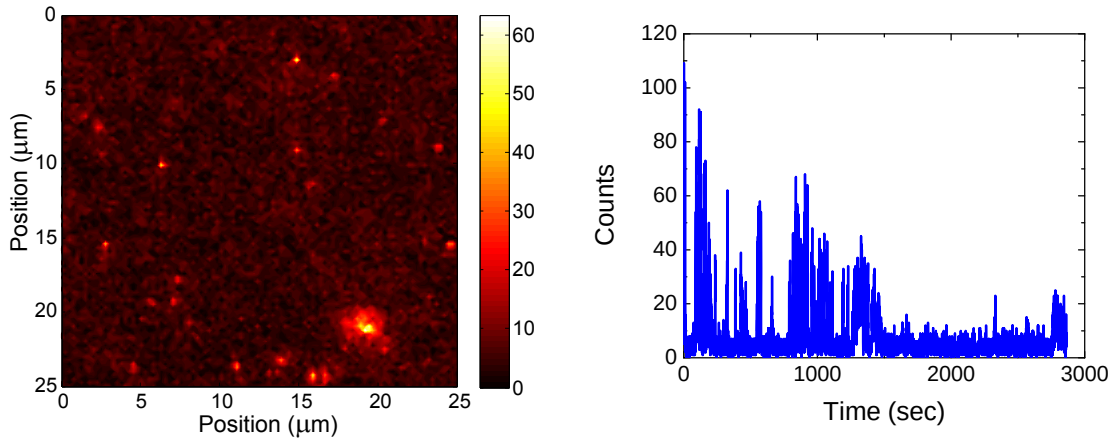

(a) (b)

Figure 5.8: (a) Fluorescence confocal imaging of the QDs in the MC, showing single QDs along with a large cluster (bottom right). (b) Time trace of a single QD showing poor photostability, few counts are detected with the passage of time.

antibunching. The plot for $g^{(2)}(t)$ along with a fitted model[2] is shown in figure 5.9.

Although the the graph of $g^{(2)}(t)$ is still noisy, the dip at $t = 0$ is clearly visible. As mentioned earlier, the noise is due to the poor photostability in the QDs. This is likely due to the PECVD deposition of the DBR above the QD defect layer. At temperatures above 100°C the ZnS shell sustains damage, which could create additional trap states and lead to longer dark-times. Results could be improved by decreasing the deposition temperature; however, the quality of the dielectric layers will decrease as a result. Alternative growth methods such as sputtering, which is carried out at lower temperature, may be utilized to deposit the top layers. Nevertheless, these results indicate that all-dielectric microcavities incorporating colloidal QDs are promising systems for cavity enhanced single photon sources.

[2]The model used is of the form, $g^{(2)}(t) = c_1(1 - c_2 \exp[-c_3|t|])$. See reference [78] for details.

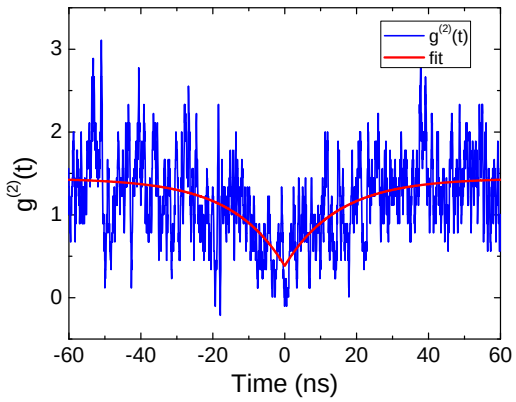

Figure 5.9: $g^{(2)}(t)$ for the sum of six single QD coincidence histograms showing a dip at $t = 0$. A fit to the experiment data is displayed as well.

5.5 Dip-Coated Quantum Dots – High Concentration Regime

In section 5.3 QDs were successfully incorporated in a MC structure, however, no threshold behavior was observed. The method used may not have yielded a thick enough QD film in order to observe gain in the system. Here a different method of QD deposition, dip-coating, is used to incorporate thicker films in the MC structures.

5.5.1 Fabrication Methods

The dielectric layers of the MC structure was fabricated using a plasma enhanced chemical vapor deposition (PECVD) system. The MC consists of two distributed Bragg reflectors (DBRs) separated by a thin layer of CdSe/ZnS (core/shell) QDs. The DBRs consisted of alternating layers SiO_2 and Si_3N_4 of quarter wavelength

thickness. The SiO_2 was deposited with a flow of N_2O at 180 sccm and 2% Si_3H_4 diluted in N_2 at 52 sccm, at a pressure of 400 mT. The Si_3N_4 layers was deposited with a flow of N2 at 180 sccm, NH_3 at 20 sccm, and 2% SiH_4 diluted in N_2 at 88 sccm, at a pressure of 800 mT. For both layers, the substrate temperature was 180C, and RF power of 100 W. The bottom DBR consisted of 10 pairs of Si_3N_4/SiO_2 deposited on a glass substrate. The cavity layer consisting of a QD film was then deposited by dip coating in a solution of QDs in toluene of 10 mg/ml concentration, and pulled at a rate of 1 mm/min.

The resulting film was estimated to be ∼200 nm thick, which corresponds to a half wavelength thick cavity. The top DBR consisting of 9 pairs was then deposited on top of the QD layer at a low processing temperature of 180°C in order to preserve the integrity of the QDs. A schematic of the structure is shown in figure 5.10a. The reflectivity spectrum of the resulting MC at normal incidence was measured using a tungsten-halogen light source coupled to an optical fiber and was collected using a fiber coupled CCD based spectrometer. The reflectivity spectrum consists of a stopband with a transmission window centered at 630 nm and a full-width-half-maximum (FWHM) of ∼10 nm, which spectrally overlaps with the photoluminescence (PL) spectrum of the QDs, as shown in figure 5.10b. A sample consisting of a QD layer of similar thickness sandwiched between two SiO_2 layers was used as the control sample for comparing the spontaneous emission rates.

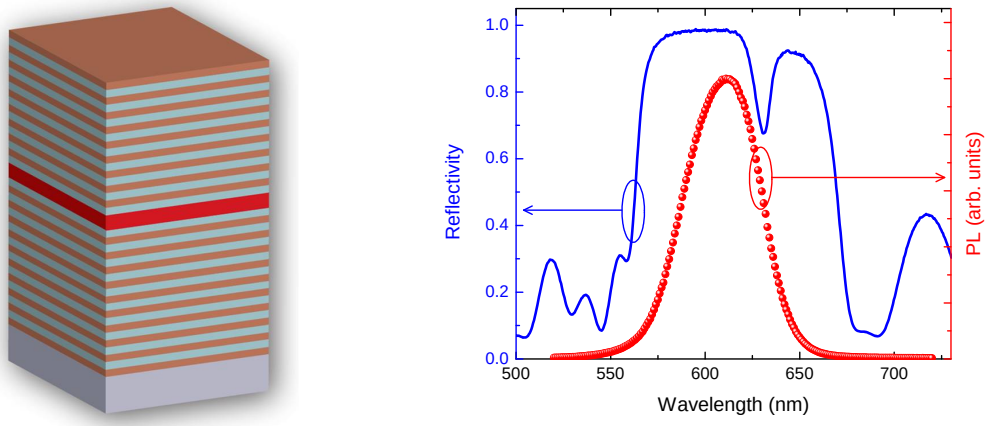

(a) (b)

Figure 5.10: (a) Schematic of the microcavity structure consisting of a half wavelength thick QD layer (red) sandwiched between a ten pair bottom DBR and a nine pair top DBR. The DBRs consist of alternating layers of Si_3N_4 and SiO_2. The structure is deposited on a glass substrate (not shown). (b) The normal incidence reflectivity of the MC is plotted together with the PL spectrum of a solution of CdSe/ZnS core-shell QDs in toluene.

5.5.2 Photoluminescence - Low Pumping Regime

Steady-state and time resolved PL measurements were used to determine the effects of the cavity on the QD spontaneous emission. In the steady state experiments, the QDs were optically pumped with a CW argon-ion laser, and the spectra were collected using a fiber-coupled CCD based spectrometer. The FWHM of the PL narrows to 10 nm compared to the control sample linewidth of 32 nm, as shown in figure 5.11a. The PL peak wavelength of the MC is slightly red-shifted compared to the control sample due to the cavity resonance being at a higher wavelength than the bare QDs (see figure 5.10b). We observe the PL is cavity linewidth limited (10 nm) and peak emission is at the spectral location ($\sim$ 625 nm) of the cavity resonance (see

figure 5.10b) indicating the coupling of the QD emission to the cavity mode.

To demonstrate enhancement of spontaneous emission, optical power dependent measurements were performed. The PL peak intensity for the MC is higher than the control for all input powers, however, no threshold behavior is observed, as seen in figure 5.11b. Time-resolved PL measurements were also carried out to determine the modification in radiative lifetime of the QDs confined in the MC. To this end, a time-correlated single photon counting technique using a pulsed 467 nm pump laser, with pulsewidth < 200 ps was used. Results of the time resolved PL measurements are shown in figure 5.11c. The lifetime of the QDs in the MC was found to be 8.9 ± 0.3 ns, while the control sample was measured to be 11.8 ± 0.6 ns. The Purcell enhancement factor (τ_0/τ_{cav}) observed in the MC structure was $\sim$1.3. The Purcell enhancement can be increased by providing lateral confinement by making the one-dimensional microcavities into micropillar structures [69].

5.5.3 Photoluminescence - High Pumping Regime

To demonstrate optical gain from the QDs embedded in the MC structure, power dependent PL measurements were repeated at higher intensities using the second harmonic (532 nm) of a Nd:YAG laser with a pulse repetition rate of 10 Hz. A sharp emission peak due to amplified spontaneous emission (ASE) begins to appear at higher pump powers as shown in figure 5.12a. The ASE peak is red shifted with

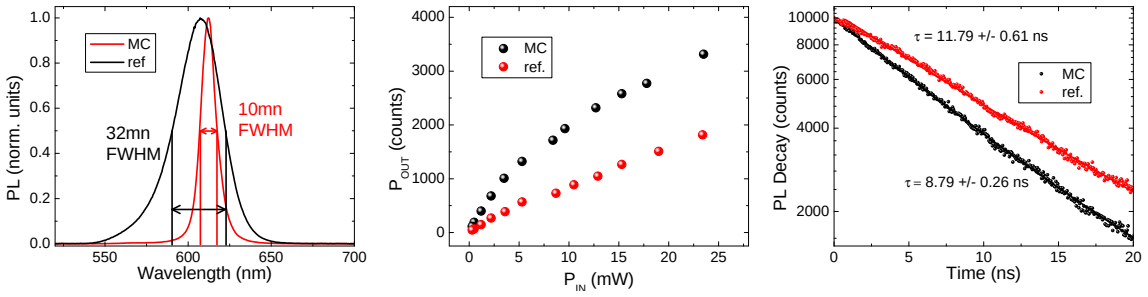

(a) (b) (c)

Figure 5.11: (a) Normalized PL from the MC and the control sample. The PL from the MC sample is narrower (10 nm FWHM) than the control (32 nm FWHM). The PL peak of the MC is red shifted and coincides with the cavity resonance of the structure. (b) CW power dependent PL peak intensities show the enhanced spontaneous emission intensity from the MC structure. However, no threshold behavior is observed under CW pumping with Argon ion laser. (c) Results of time-resolved PL measurement for the control (red) and MC (black) sample with lifetimes of 11.8 ± 0.6 ns and 8.9 ± 0.3 ns. The decrease in lifetime in the MC provides further evidence of enhancement of spontaneous emission in the MC structure.

respect to the single exciton emission and corresponds to the biexciton energy which is lower than the single exciton energy due to the exciton-exciton attraction which decreases the biexciton energy [79]. The ASE peak shows a clear threshold behavior and a large increase in output intensity with increasing pump power (figure 5.12b).

The effect of the MC on the ASE is demonstrated via angle resolved emission experiments. We use the angular dispersion of the cavity mode to tune the resonant wavelength of the cavity. As the cavity mode is tuned into resonance with the ASE peak of the QDs ($\sim 5^\circ$), we observe a large increase in ASE intensity when compared to off resonant angles (for example, 25°) owing to the photon field increase in the MC at the resonant wavelength. The enhancement of the gain of the biexcitons is clearly

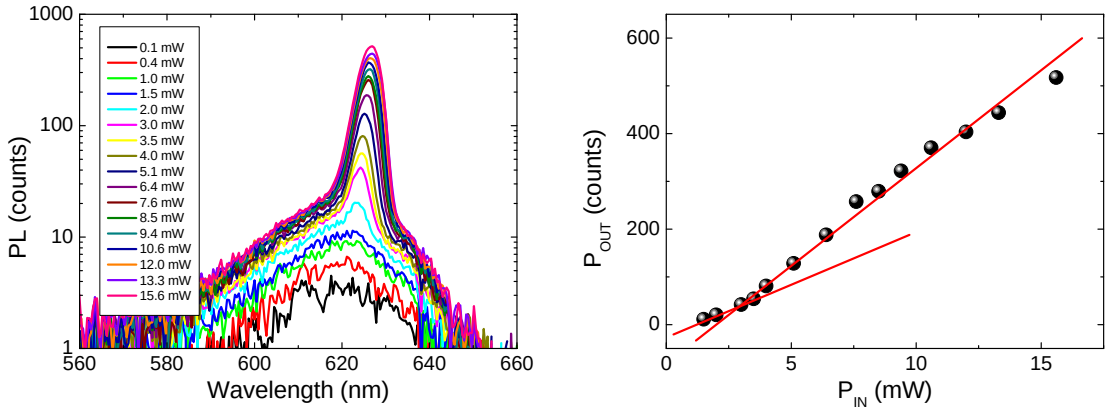

(a) (b)

Figure 5.12: (a) Power dependent photoluminescence under high power pulsed excitation showing the development of amplified spontaneous emission (ASE). Narrow ASE peak at the biexciton energy start to appear at 2.0 mW pump power. (b) The ASE peak power is plotted against the time-averaged input power showing a clear threshold behavior and large increase in emission intensity.

seen from the increase in ASE intensity at resonance as shown in figure 5.13a. This modification in ASE due to the MC results in strong emission from the cavity at the resonant angles, yielding highly direction emission. The result of the angle resolved ASE measurements from the cavity showing highly directional emission is shown in figure 5.13b. For comparison, the emission pattern of a Lambertian source is also plotted.

5.5.4 Conclusions

In summary we have demonstrated enhancement of gain in a monolithically fabricated all-dielectric MC. An increase of 33% in the radiative rate of the QDs was observed inside the MC. Spectroscopic measurements show the enhanced PL power

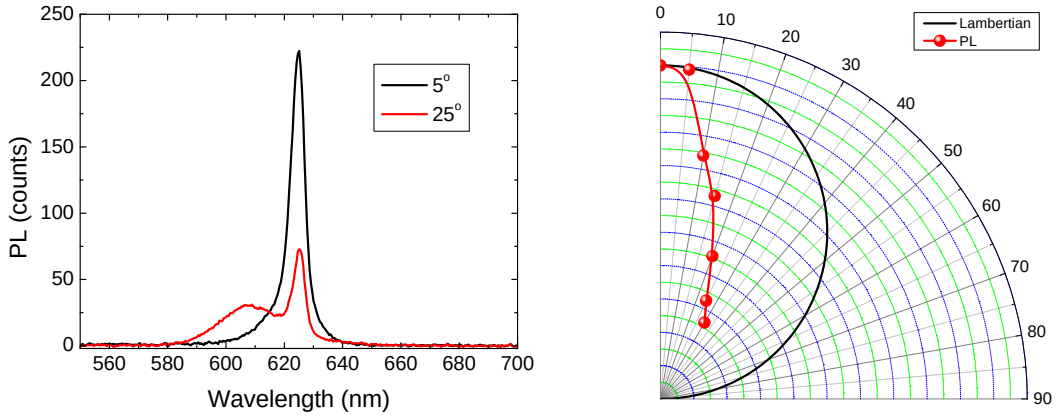

(a) (b)

Figure 5.13: (a) ASE from the MC structure at two different angles corresponding to on-resonance (5°) and off-resonance (25°) conditions. The peak emission intensity increases by a factor of three when the ASE peak is in resonance with the cavity mode. (b) Angular emission characteristics of the MC structure showing highly directional emission. The emission patern of a Lambertian source is also shown for comparison. Here 0° corresponds to direction noral to the microcavity structure.

of the QDs in the MC compared to the control sample. Pumping the sample at higher intensities yields modal gain enhancement of the biexcitons. By using QDs with a lower gain threshold similar to those used in the work of Dang, *et. al.* [72], one could use the approach presented here to realize monolithically integrated all-dielectric vertical cavity surface emitting lasers. The approach presented here can be easily extended to wide spectral range by changing the type of quantum dots. Furthermore, the MC structure demonstrated here can also be realized on silicon substrate allowing integration of CMOS electronics with such light emitters.

5.5.5 Lasing and Auger Recombination

Lasing in colloidal quantum dot (QD) systems has been a major challenge due to nonradiative Auger recombination [58, 64, 80–84]. Auger recombination is a multiparticle process that occurs in atomic, semiconductor bulk , and quantum confined systems [80, 85, 86]. There are different types of Auger processes [87]. For the purposes of this discussion, the most simplistic case will be considered. When two excitons exists in the system, they can interact through coulomb interaction, and one of the excitons recombine nonradiatively and a carrier in the second exciton is excited to a higher energy level. The re-excited carrier eventually returns to its originally excited state nonradiatively by phonon scattering. This process is shown schematically in figure 5.14.

Since Auger recombination is a multiparticle scattering process, it is important to be able to characterize the average number, $\langle N \rangle$, of exciton per QD. Experimentally, this can be carried out when noting the relation:

$$\frac{I_i - I_t - I_r}{f} = \langle N \rangle \frac{ATd}{V_{QD}} E_{ph} \tag{5.2}$$

where I_i, I_t, and I_r are the incident, transmitted, and reflected time-averaged intensities. f, is the pulse repetition rate, A, and T, the excitation area and QD film thickness, d, the fill fraction of QDs, V_{QD}, the estimated volume of a QD, and E_{ph} is the photon energy.

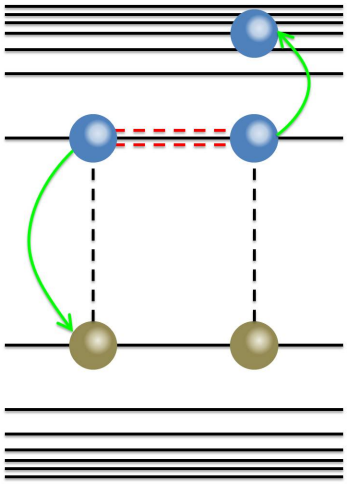

Figure 5.14: Two excitons (spheres connected by black dashed lines) can interact through coulomb interaction (red dashed double line), and one of the excitons recombine nonradiatively (green downward arrow) and a carrier in the second exciton is excited to a higher energy level (green upward arrow). The re-excited carrier eventually returns to its originally excited state nonradiatively by phonon scattering (not shown).

The emission intensity per QD can be modeled using a simple model given by [72]:

$$I\left(\langle N\rangle\right) = P(1)\beta_1 + P(2)(\beta_1+\beta_2) + P(3)(\beta_1+\beta_2+\beta_3) + \cdots \tag{5.3}$$

where $P(n)$ is the probability of having n excitons in the QD, which is taken as a Poisson distribution $P(n) = \langle N\rangle^n e^{-\langle N\rangle}/n!$, and β_n is the quantum efficiency of the n^{th} exciton. This can be rewritten to a more convenient form:

$$I\left(\langle N\rangle\right) = \sum_{i=1}^{\infty} \beta_i P\left(n \geq i\right) = \sum_{i=1}^{\infty} \beta_i \left[1 - \sum_{n=0}^{i-1} P(n)\right] \tag{5.4}$$

The quantum efficiency of biexcitons, β_2, can be written in terms of the single exciton quantum efficiency β_1 and the single exciton radiative lifetime τ_1 and the biexciton

Auger nonradiative lifetime τ_2:

$$\beta_2 = \beta_1 \frac{\tau_1^{-1}}{\tau_1^{-1} + \tau_2^{-1}} \tag{5.5}$$

In colloidal QD systems, $\tau_1 \sim 10$ ns, and $\tau_2 \sim 100$ ps. Which means in these systems, β_2 is approximately two orders of magnitude smaller than β_1, this will be even smaller for a greater number of excitons. Therefore, the QDs with more than two excitons can be omitted in 5.4 and written by the following:

$$I\left(\langle N \rangle\right) = \beta_1 \left[1 - P(0)\right] + \beta_2 \left[1 - P(0) - P(1)\right] \tag{5.6}$$

A plot of the for realistic β values is shown in figure 5.15.

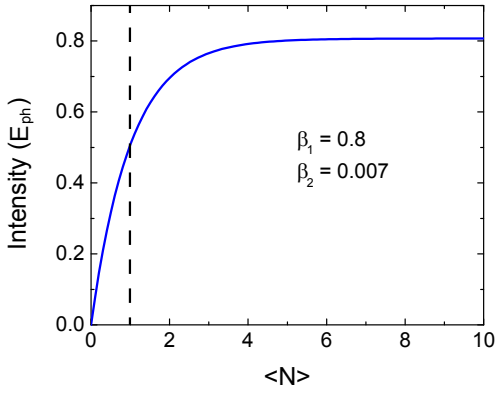

Figure 5.15: Intensity as a function of average number of exciton per QD. The vertical dashed line indicates the average number of one exciton per QD. The onset of biexciton ASE (biection gain) with average number of excitons greater than one is the regime where lasing is unlikely due to Auger recombination.

For the case of an ideal, type I, colloidal QD, the condition for amplification is $\langle N \rangle > 1$. However, when taking more realistic electronic and biexcitonic considera-

tion, the condition becomes $\langle N \rangle \approx 1.5$ [88–90]. In type II materials, Auger recombination is not present due to the energy shift of the biexciton energy [79, 91, 92]. These systems however, are not a viable alternative to their small oscillator strength. Engineering the shape of the QD has lead to values lower than the theoretical limit for spherical excitons [93] and have been observed in pyramid-like shaped QD to observe gain as low as $\langle N \rangle = 0.83$ [72]. The effects of Auger recombination are still present at these values owing to the percentage of multiexcitons; for $\langle N \rangle = 0.83$, $P(n > 1) \approx 20\%$, and in order to get the multi excitons below 10%, $\langle N \rangle < 0.54$.

Colloidal QDs have been of great interest in recent years due to their simple and inexpensive fabrication process. Lasing, however has only very recently been observed [72], and that with engineering the shape of the QDs. In order to make colloidal QD a more viable lasing gain medium, Auger recombination needs to be further inhibited to reduce the lasing threshold in these systems.

5.6 Gain in Colloidal Quantum Dots

In realizing active photonic devices incorporating QDs, it is important to characterize the gain of the medium since they are often designed to enhance the light-matter interaction, where enhanced emission and lasing are desired [80, 94]. What is presented in this section is modal gain measurements for CdSe/ZnS (core/shell) QDs.

5.6.1 Variable Stripe Length Method

The technique used in this work is known as the variable stripe length method (VSLM), and was developed for measuring gain in bulk semiconductor crystals [95, 96]. The technique involves exciting a thin stripe of known length of the material and collecting the emission from the side. A schematic of this is shown in figure 5.16.

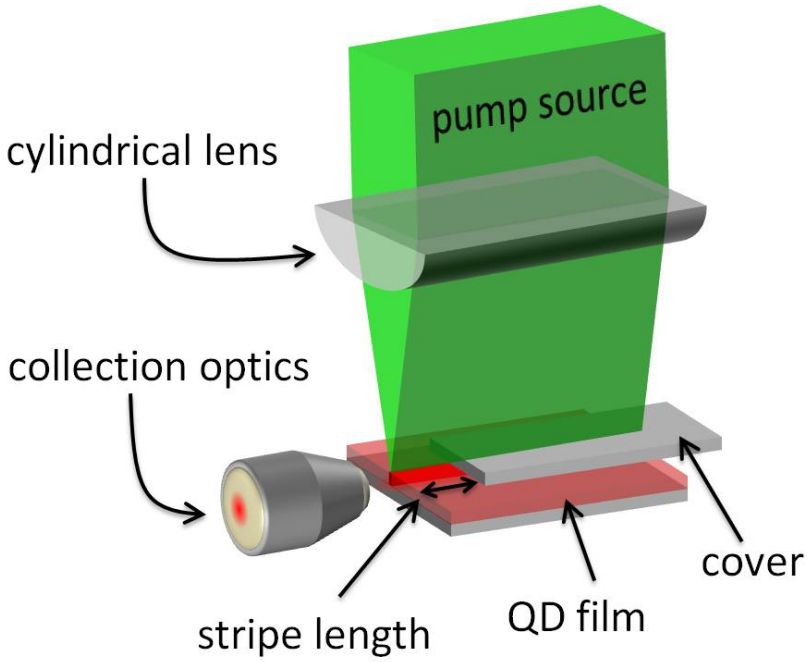

Figure 5.16: Schematic of the VSLM setup showing the excitation beam passing through a cylindrical lens where it focuses to a line. A movable cover blocks the sample from excitation allowing only a specific length exposed to the beam.

The emission is waveguided along the strip due to the photo induced refractive index change of the excited region. The model for the intensity can be described by a simple model:

$$\frac{dI(\lambda,x)}{dx} = g(\lambda,x)I(\lambda,x) + J_{spon}\Omega \tag{5.7}$$

where $I(\lambda, x)$ is the intensity observed at wavelength λ from exciting a length x of the active medium. $g(\lambda, x)$, J_{spon}, and Ω are the modal gain, spontaneous emission density, and solid angle along the waveguide, respectively. If the modal gain is taken to be constant, i.e., ignoring gain saturation, equation 5.7 can be solved analytically, giving the following expression for the measured intensity:

$$I(\lambda, x) = \frac{J_{spon}\Omega}{g(\lambda)} e^{(g(\lambda)x-1)} \tag{5.8}$$

Using equation 5.8, it is possible to fit experimental data to estimate the modal gain of the system [58, 97]. One of the major disadvantages of this approach is that it neglects gain saturation effects [98]. A modified version of equation 5.8 to include gain saturation has also been used where the intensity is of the form [99]:

$$I(\lambda, x) \propto e^{\left[g(\lambda)l\left(1-e^{-x/l}\right)\right]} \tag{5.9}$$

where l is a characteristic length of the gain. This will work for systems where the intensity versus stripe length curve tapers off exponentially. However, this need not be the case for complex systems such as colloidal quantum dots which will be shown to have a nontrivial gain spectrum. Using either equations 5.8 or 5.9, the experimental data needs to be fitted at each wavelength in order to obtain the complete gain spectrum. This process is computationally expensive and the fitting parameters are not always physical. For this reason most VSLM measurement analyses use equation 5.7 to calculate the gain spectrum directly from the intensity data where the gain will

have the form [100–105]:

$$g(\lambda, x) = \frac{dI(\lambda, x)/dx}{I(\lambda, x)} - \frac{J_{spon}\Omega}{I(\lambda, x)} \tag{5.10}$$

where the numerator in the second term, $J_{spon}\Omega$, is found by solving equation 5.7 for low excitation intensities where the gain is zero.

To characterize the CdSe/ZnS (core/shell) colloidal QDs used in this work, a sample of the QDs was prepared by drop coating on a glass substrate. The resulting film thickness is estimated to be on the order of tens of microns. The choice of substrate is not arbitrary for the VSLM experiment. In order for the QD emission to be guided properly through the photo-induced waveguide, the substrate needs to be of lesser refractive index than the QD film.

An argon-ion CW laser was used as the excitation source. The beam was sent through a cylindrical lens to create a thin stripe to excite the QDs, where a movable cover was used to expose a length of the sample. The emission was collected with a microscope objective lens and was sent to a fiber coupled CCD based spectrometer. The experimental setup is schematically shown in figure 5.16.

The emission was collected for stripe length from 5 μm to 500 μm in increments of 5 μm. The small increment is necessary for the numerical gain calculation in equation 5.10 due to the evaluation of a derivative. The photoluminescence (PL) spectra at various stripe length excitation is shown in figure 5.17a, where the biexciton emission peak begins to appear at 100 μm excitation length. Although the biexciton

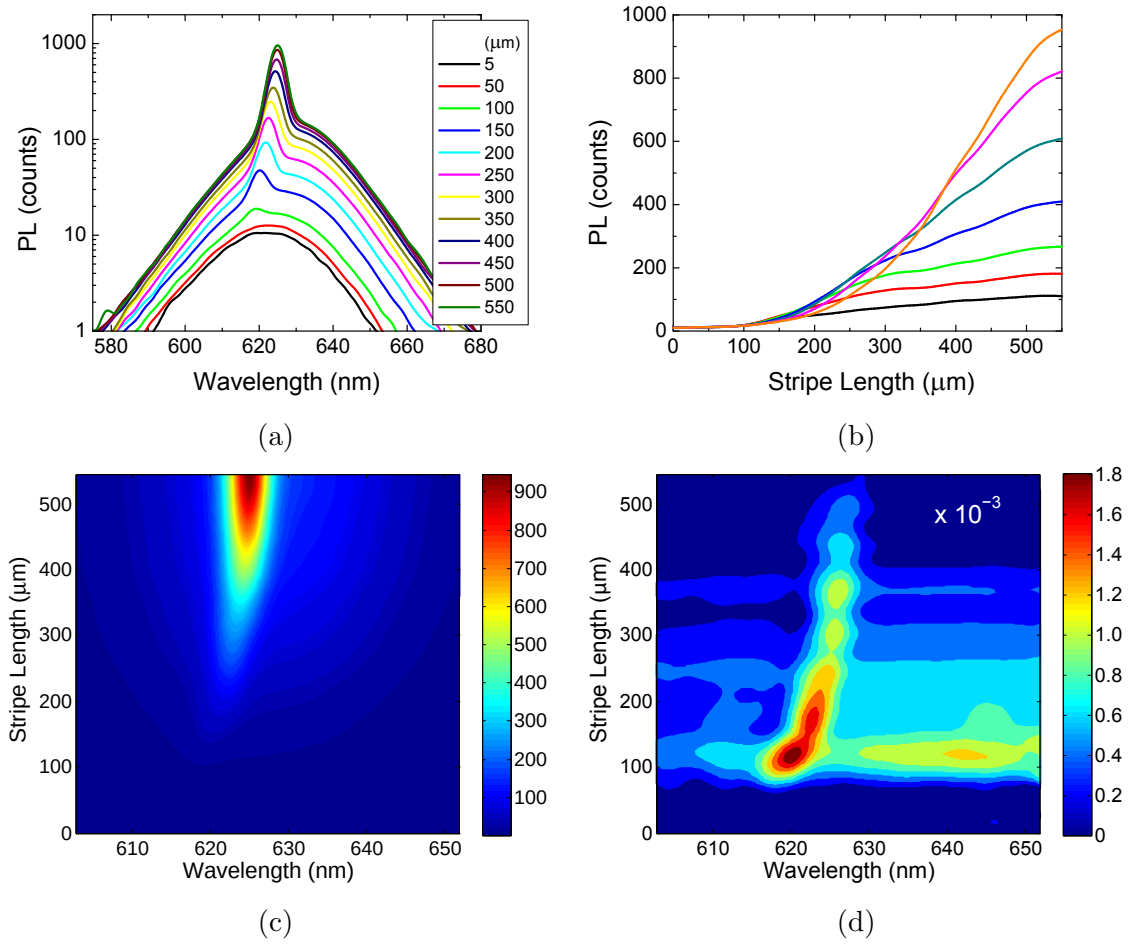

Figure 5.17: (a) PL spectra for excitation length ranging from 5 μm to 500 μm plotted on a logarithmic scale showing the biexction emission peak. (b) PL intensity at wavelengths near the biexciton emission peak as a function of excitation stripe length. The PL clearly shows gain saturation at long lengths. (c) The entire range of PL needed for the numerical calculation of gain. (d) Gain (μm^{-1}) for the QD sample showing a maximum value of 1.8×10^{-3} μm^{-1} which occurs nearly after the appearance of the biexciton peak.

peak continues to grow with increased excitation length, gain saturation is clearly visible in figure 5.17b, reconfirming the limitations of using equation 5.8 in such systems. The PL used for the gain calculation is shown in figure 5.17c, and the

results of which are shown in figure 5.17d. The gain plot shows a maximum value of 1.8×10^{-3} μm^{-1} at ~ 110 μm. It is interesting to note that the maximum gain occurs nearly after the appearance of the biexciton emission peak rather than the maximum PL intensity. This can be understood by noticing that the expression for gain in equation 5.10 depends on the relative change in intensity rather than the intensity itself. At the onset of biexciton emission peak, there is a large change relative to before the appearance of the biexciton emission peak.

5.7 Conclusions

Resonant photonic structures in the form of microcavity systems were used to investigate the enhancement of light-matter interaction with colloidal quantum dots. The investigation can be categorized in two regimes: Low-concentration, and high concentration of colloidal quantum dots.

1. Low concentration of quantum dots were incorporated in the cavity layers by spin coating. In these structures, steady-state photoluminescence spectroscopic measurements showed the quantum dots to emit through the cavity resonance in a narrow emission line.

    (a) Power dependent photoluminescence measurements were carried out and show a strictly linear dependence of peak emission intensity to the input power and no change in the emission linewidth, indicating a no threshold

behavior in this system due to the low concentration of quantum dots where the system is below the gain threshold.

(b) Although microcavity structure with low concentrations of quantum dots in the cavity layer are undesirable for observing gain, ultra-low concentrations are desirable micorcavity enhanced single-photon sources. To this end, the second-order coherence function was measured using a Hanbury Brow-Twiss interferometer which measures the temporal correlations of photons. Areas of single quantum dots were isolated using a fluorescence confocal imaging setup where the fluorescence time trace of the quantum dots show poor photostability. Although the coincidence histograms of single quantum dots were too noisy to observe antibunching, the sum of six single quantum dot histograms show a clear antibunching behavior through the still considerable noise level.

2. Microcavity structures with high concentrations quantum dots were realized by the dip coating deposition technique.

(a) Time-resolved photoluminescence measurements show a Purcell enhancement factor of $\sim$1.3. Steady-stead power dependent photoluminescence using a continuous-wave laser excitation source indicate enhanced emission intensity of the microcavity structure when compared to the reference sample. However, when using a high power pulsed excitation source,

threshold behavior of photoluminescence intensity is observed at the onset of gain in the biexcitons. Furthermore, angle resolve photoluminescence measurements indicated enhancement of gain due to the microcavity and highly directional emission. Although gain is observed in this structure, there is no evidence of lasing due to nonradiative Auger recombination.

(b) The variable stripe length method was implemented in order to characterize the gain profile of a dip coated film of quantum dots. Steady-state photoluminescence spectroscopic measurements were performed by acquiring the intensity of emission from a photo-induced waveguide. The emission intensity was used to directly determine the modal gain profile of the quantum dot film. The direct calculation approach has multiple benefits. It provides a means to calculating the modal gain spectrum for an entire wavelength range without the need for numerical fitting at each wavelength. It also allows for calculating nonuniform modal gain even beyond the threshold of gain saturation where numerical models are poor at describing the gain over the full range of excitation lengths.

Chapter 6

Coupled-Cavity Structures

6.1 Introduction

Optical microcavities continue to play an important role in photonics, owing to their wide range of applications [106]. A recent application of microcavities is the all-optical effects that have similar behavior to electromagnetically induced transparency (EIT), which is observed in atomic systems, for which coupled ring cavities have been applied [107–111]. EIT is an example of the response of an atomic medium to coherent electromagnetic fields as it prevents absorption of light that is resonant to atomic transitions. This behavior arises as a result of coherence between atomic states, obtained by coupling atomic states to coherent light sources [112]. Optical analogs of EIT effects can be used for realizing chip scale coherent photonic systems that operate at room temperature. In initial experiments exploring optical analogs

of EIT, light was coupled to a pair of interacting resonant ring cavities. Within each cavity, the resonant modes circulate in two-dimensional ring-like orbits and destructive interference between circulating light fields of a high and a low quality factor (Q) microcavity results in optical analog of EIT. In earlier research on interacting ring cavities, controlled coupling between the microcavities is found to be vital for attaining EIT-like photonic resonances [107, 108]. In order to study these systems properly, precise control of interaction between two appropriately designed microcavities is required. Although theoretical investigations of 1D coupled microcavities (CMC) have been carried out in the past, optical analogs of EIT effects have not been discussed in this context [113–115].

6.2 Passive Structures

6.2.1 Design and Optical Modes

For the investigation of EIT-like features in CMC systems, two $\lambda/2$ SiO_2 microcavities that are embedded in a 1D photonic crystal consisting of a SiO_2/Si_3N_4 distributed Bragg reflector (DBR) were fabricated using a plasma enhanced chemical vapor deposition (PECVD) system (see section 2.1.3 for details). The incident light is coupled to the first cavity through the top or input DBR mirror. Light is then coupled to the adjacent cavity through the portion of DBR mirror that interlinks the

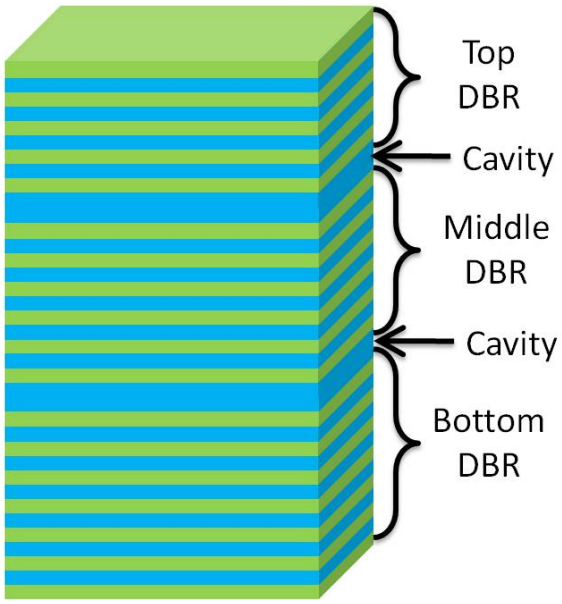

Figure 6.1: A schematic of a CMC structure showing three DBRs (bottom DBR middle DBR, and top DBR) separated by cavity layers.

two microcavities. The middle DBR mirror thus allows optical interaction between the two microcavities. A schematic of the CMC is shown in figure 6.1. By varying the number of SiO_2/Si_3N_4 bilayers of the middle DBR, coupling between the two cavities can be controlled precisely, as the mirror reflectivity may be increased with the incorporation of additional bilayers.

The CMC samples are realized using a plasma enhanced chemical vapor deposition. The three fabricated CMC samples have similar structures except the middle DBR mirror. The DBR structures are of the general form $N_b/C_2/N_m/C_1/N_t$, where N_b, N_m, and N_t, indicate DBRs with N number of pairs (or bilayers) in the bottom, middle and top DBRs, respectively. Each pair consists of a Si_3N_4 ($n = 1.77$) and SiO_2 ($n = 1.45$) layer, each of $\lambda/4$ optical thickness. The cavity layers, C_1, and

Sample	SiO_2 (nm)	Si_3N_4 (nm)
$\mathcal{S}_1$	103.5	82.0
$\mathcal{S}_2$	104.0	83.0
$\mathcal{S}_3$	104.5	83.5

Table 6.1: Thickness of the layers in the CMC structures obtained from fitting with simulated reflectivity spectra. The fitted thickness show only a slight variation ($< 1\%$) between the three samples.

C_2, are fabricated from lower refractive index material SiO_2. For the three samples studied, $N_b = 5.5$, and $N_t = 9.5$, whereas N_m for the samples $\mathcal{S}_1$, $\mathcal{S}_2$, $\mathcal{S}_3$ is 14.5, 10.5, and 3.5, respectively. The half integer number of pairs indicate an additional single layer of Si_3N_4.

6.2.2 EIT–Like Features

The spectral characterization of the samples is carried out with a fiber coupled CCD based spectrometer (see section 2.2.1 and 2.2.3). Figure 6.2 shows the measured and calculated reflection spectra. Here, we note an important distinction between atomic EIT and its optical analog in 1D CMC system. In atomic systems, EIT results in enhanced transmission whereas photonic EIT in 1D CMCs results in increased reflection. By fitting the measured reflectance spectra using transfer-matrix method (TMM) calculations (see section 2.2.2), the layer thickness and refractive indices are obtained for each sample. These parameters are listed in table 6.1 and show only minor variations ($< 1\%$) from sample to sample and intended layer thickness, and indicate good control over the fabrication process.

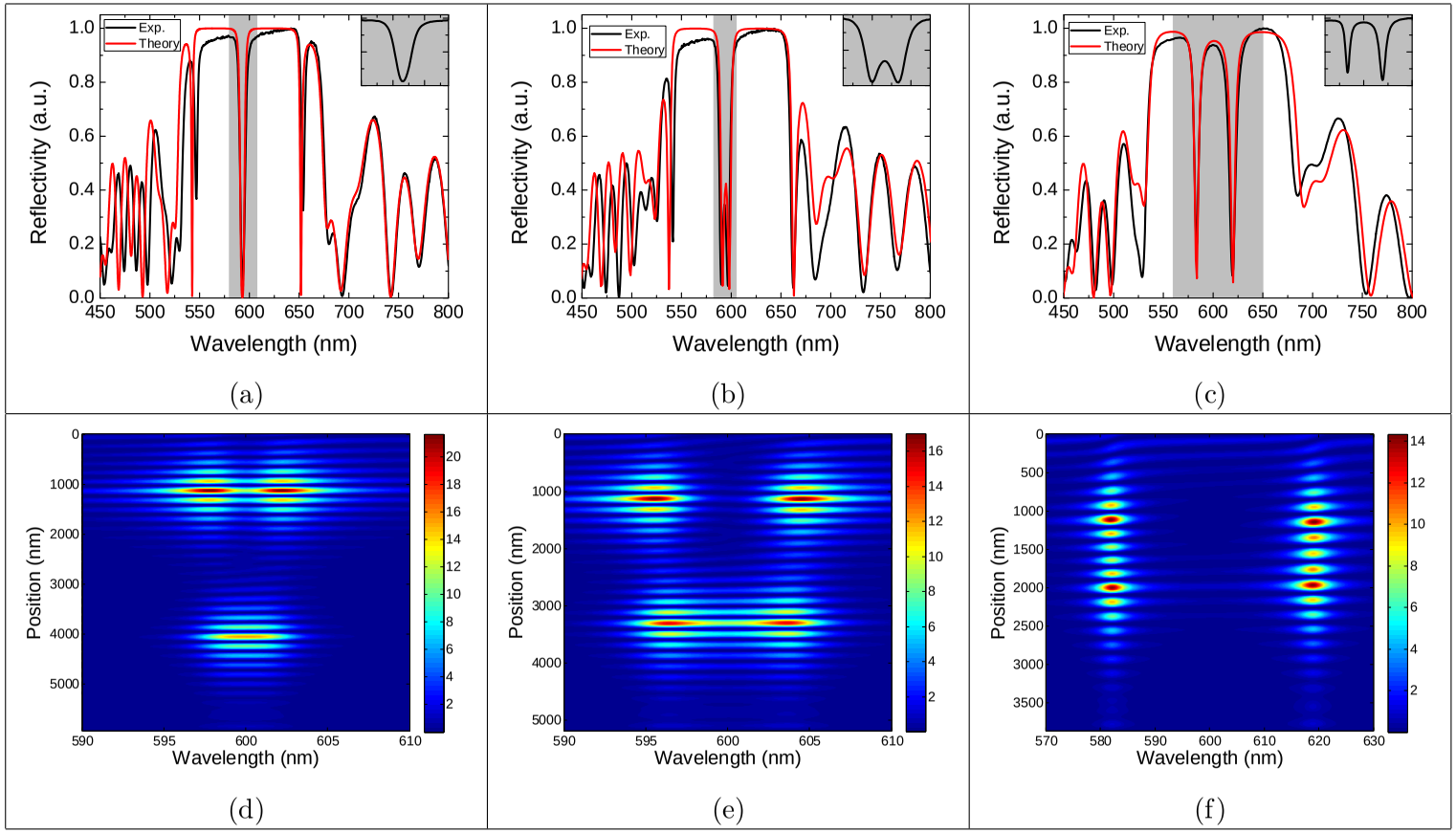

Figure 6.2: (a)-(c) Measured and fitted reflectance for samples $\mathcal{S}_1$, $\mathcal{S}_2$, and $\mathcal{S}_3$, respectively. For $\mathcal{S}_1$, the SiO_2, and Si_3N_4 layers were fitted at 103.5 nm, and 82.0 nm, respectively. For $\mathcal{S}_2$, the SiO_2, and Si_3N_4 layers were fitted at 104.0 nm, and 83.0 nm, respectively. For $\mathcal{S}_3$, the SiO_2, and Si_3N_4 layers were fitted at 104.5 nm, and 83.5 nm, respectively. The insets in (a) - (c) magnify the spectral regions where the resonances are located (shaded regions). (d)-(f) shows the field intensity inside the structures in the spectral vicinity of the resonances.

The reflection spectrum of sample $\mathcal{S}_1$ demonstrates a single resonance near 593 nm. The spectrum corresponding to sample $\mathcal{S}_2$, where the intercavity separation is decreased in comparison to $\mathcal{S}_1$, shows appearance of a sharp peak within the resonance dip, a spectral feature that resembles to the EIT phenomenon in atomic systems. In case of sample $\mathcal{S}_3$, where the intercavity separation is least among the three investigated samples, the resonance is split into two dips, each having a Q factor that exceeds the initial CMC Q-factors in the weakly coupled case (figure 6.2a).

To further investigate the experimental observations, we consider electromagnetic field intensity distribution maps (figures 6.2d-6.2f). The steady-state distributions of incident field are based on TMM simulations and suggest the following description for modes of the CMC structures.

For the large separation between the two cavities, sample $\mathcal{S}_1$, at resonance, the field is localized in the second cavity (closer to the substrate). The first cavity, however, shows two-lobe maxima off-resonance with a minima on-resonance. As the separation between the two cavities decreases, sample $\mathcal{S}_2$, the coupling increases, and field in each cavity begin to further split. Finally, when the spacing is sufficiently small, $\mathcal{S}_3$, the modes completely split and the field is delocalized at each of the resonances.

At large cavity separations, the field is at a minima in the first cavity while it is at a maxima in the second cavity. Therefore, it is convienient to refer to the first cavcity as the *dark* cavity, and the second cavity, the *bright* cavity. This terminology will be useful in section 6.3 where this will be discussed in further detail in the context of

active structures where quantum dots embedded in the cavities.

6.3 Active Structures

6.3.1 Introduction

In section 6.2, coupled microcavity structures (CMCs) were discussed in the context of similarities to electromagnetically induced transparency (EIT). The field distributions in three different CMCs were considered which had varying degrees of coupling. In this section, a similar structure will be considered, where the *bright* and *dark* cavities are embedded with quantum dots (QDs). The reflectivity spectra, field intensity profiles, and photoluminescence spectra will be discussed.

6.3.2 Design and Optical Modes

A CMC systems consisting of two $\lambda/2$ SiO_2 microcavities that are separated by a set of SiO_2/Si_3N_4 distributed Bragg reflector (DBR). The dielectric layers were fabricated using a plasma enhanced chemical vapor deposition (PECVD) system (see section 2.1.3 for details). The incident light is coupled to the first cavity through the top or input DBR mirror. Light is then coupled to the adjacent cavity through the portion of DBR mirror that interlinks the two microcavities. The middle DBR mirror thus allows optical interaction between the two microcavities. By varying the number

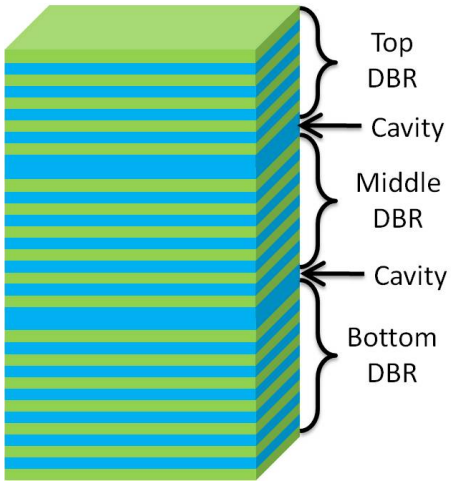

Figure 6.3: A schematic of a CMC structure showing three DBRs (bottom DBR middle DBR, and top DBR) separated by cavity layers.

of SiO_2/Si_3N_4 bilayers of the middle DBR, coupling between the two cavities can be controlled precisely, as the mirror reflectivity may be increased with the incorporation of additional bilayers.

The CMC was fabricated using a plasma enhanced chemical vapor deposition. The structure is of the general form $N_b/C_2/N_m/C_1/N_t$, where N_b, N_m, and N_t, indicate DBRs with N number of pairs (or bilayers) in the bottom, middle and top DBRs, respectively. Each pair consists of a Si_3N_4 ($n = 1.77$) and SiO_2 ($n = 1.45$) layer, each of $\lambda/4$ optical thickness. The cavity layers, C_1, and C_2, are fabricated from lower refractive index material SiO_2. For the sample studied, $N_b = 20.5$, $N_m = 12.5$, and $N_t = 3.5$. The half integer number of pairs indicate an additional single layer of Si_3N_4. A schematic of the structure is shown in figure 6.3.

The reflectivity of the CMC structure shows a single resonance in a broad bandgap.

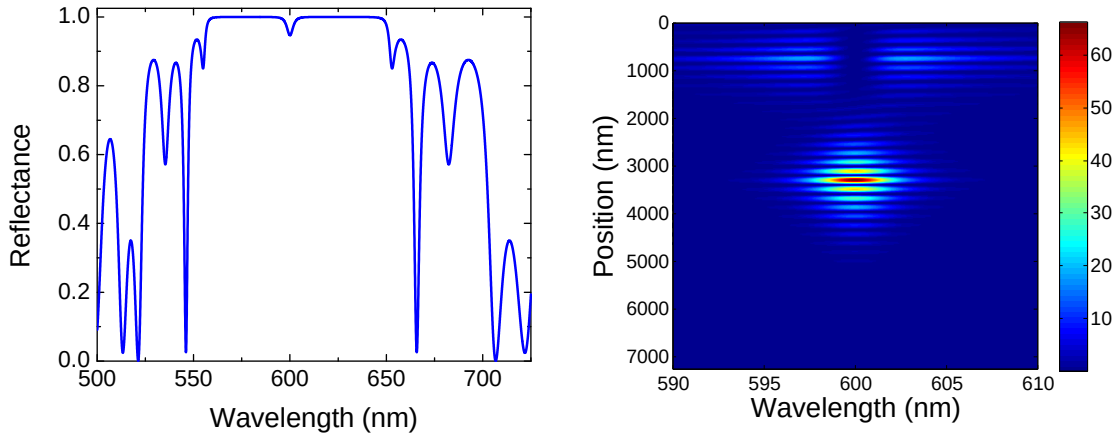

(a) (b)

Figure 6.4: (a) Reflectivity spectrum of the CMC structure showing a shallow dip at resonance. The reason for the dip being shallow is the large number of periods in the bottom DBR compared to the top DBR. (b) Intensity profile of the CMCs showing the field highly localized in the second cavity. The first cavity shows a split field distribution where two distinct lobes are at either side of the resonance. The field in the first cavity is *dark* at resonance.

The dip in reflection at resonance is shallow (figure 6.4a) due to the large number of layers in the bottom DBR. Although the dip is shallow, the field is still localized in the cavity. Figure 6.4b shows the field concentrated in the second cavity, while the field pattern in the first cavity is split into two distinct lobes on each side of the resonance.

The intensity profile cross section at resonance is plotted in figure 6.5a, and show the field to be peaked at the center of the second cavity, and minimal field in the first cavity, as expected from figure 6.4a. However, the area in the vicinity of the first cavity shaded in gray is magnified in figure 6.5b, showing zero field in the center of the cavity.

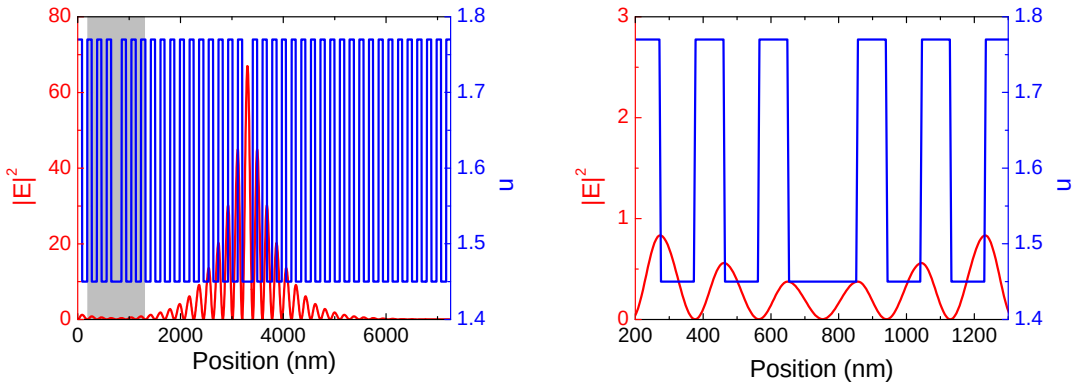

(a) (b)

Figure 6.5: (a) Field intensity profile (red curve) cross section at resonance, drawn on the same plot as the refractive index profile (blue curve). The plot shows the field peaked in the second cavity, whereas the first cavity, the field intensity is low. The region in the vicinity of the first cavity shaded in gray is magnified in (b) showing zero field and the center of first cavity.

6.3.3 Photoluminescence

CdSe/ZnS (core/shell) colloidal QDs were incorporated into the bright and dark cavities by interrupting the PECVD deposition and spin coating 0.1 mg/ml solution in toluene. (see section 2.1.1 for details). Two samples were fabricated, one with QDs in the bright cavity, and the other with QDs in the dark cavity. The modes of the passive CMC was described in section 6.3.2, and we expect QDs placed in the bright cavity (bright cavity loaded) to emit through the resonance.

The normal incidence reflection and photoluminescence (PL) for the loaded bright cavity is shown in figure 6.6a. The reflectivity shows a narrow dip at resonance superimposed on a broad dip. The narrow dip is due to the cavity resonance, however, the broad dip is due to the broad absorption of the QDs. The PL for this structure

shows a narrow emission through the resonance of the cavity, and uncoupled QD emission is not observed.

For a loaded dark cavity, however, since the field is zero in the cavity, the QDs emission is not expected to emit through the resonant mode. The normal incidence reflection and PL for the loaded bright cavity is shown in figure 6.6b. The reflectivity shows a narrow dip at resonance and a broad dip associated with the QD absorption at a longer wavelength. The narrow dip is due to the cavity resonance, which can be atributed to the second cavity, while the broad dip is due to the broad absorption of the QDs, as with the loaded bright cavity (figure 6.6a). The PL is not completely dark as one may have expected from the field intensity profile plotted in figure 6.5. The PL for this structure shows a broad emission at the same spectral region as the absorption dip due to the QDs. This indicates emission from QDs that are uncoupled to the cavity. There is no significant emission at the cavity resonance. It is difficult to determine if the CMC has any effect on the QDs in the dark cavity due to the large uncoupled emission. If there any effects, they are negligible in comparison to the uncoupled emission, where in the case of the bright cavity there was no uncoupled emission observed at all.

Experiment realizations of CMC structures require precise fabrication control. In addition to the structure design which controls the coupling between the two cavities, the cavities themselves need to be in resonance with each other. The coherence effects described in section 6.2 is contingent on the two cavities being in resonance.

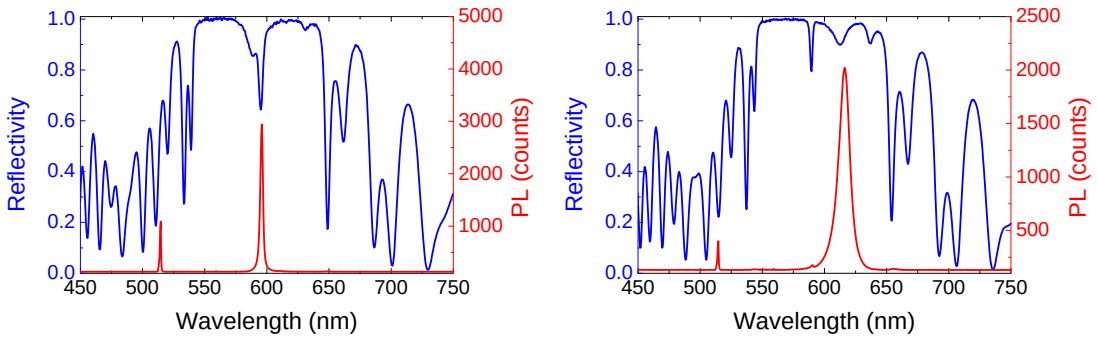

(a) (b)

Figure 6.6: (a) Normal incidence reflectivity and PL for the bright cavity loaded with QDs. The Reflectivity shows a narrow cavity resonance superimposed on a broader dip which is caused by the QD absorption. The PL shows a narrow emission of the QDs through the cavity resonance. No broad emission due to uncoupled QDs is observed. (b) Normal incidence reflectivity and PL for the dark cavity loaded with QDs. The Reflectivity shows a narrow cavity resonance in addition to a broader dip which is caused by the QD absorption. The PL shows a broad emission of uncoupled QDs. No significant narrow emission through the cavity mode is observed.

These structures are very sensitive to slight deviation in cavity thickness. The fabrication process is based on PECVD deposition (see section 2.1.3), spin coating (see section 2.1.1) combination. PECVD deposition is carried out based on growth rate calibrations, which can fluctuate slightly. When fabricating large stuctures such as CMCs, these fluctuation can become significant. The spin coating method for depositing QDs yield films which can have thickness variations of a few nanometers. These variations can often be advantageous where one may find a region on a given sample where the film has the desired thickness. Even when these fluctuations are considered, there are still sample to sample thickness variations which can often detune the cavity from the desired thickness across the entire sample. With all parameters considered,

great care needs to be take when fabricating 1D CMC structures in order to ensure the cavities are in resonance with each other, and often typical fabrication error can adversely affect the performance of the device.

6.4 Conclusions

A quantitative investigation of EM field distribution in a CMC was carried out followed by exp realization of such structures. These results suggest that by adjusting the coupling between the two cavities, a desired distribution of the incident field may be achieved. The photonic EIT-like resonances of 1D CMCs may be used to implement photonic applications which resemble atomic systems.

Chapter 7

Summary and Outlook for Future Research

7.1 Summary

In this work, resonant photonic structures were investigated as a means to control light-matter interaction. One aspect of this was to study systems where the collective behavior of excitons in quantum confined structures can be realized.

1. Collective phenomena of quantum confined excitons:

   (a) Resonant photonic crystals is one such system that was studied. As a realization of this system, a $GaAs/AlGaAs$ multiple-quantum-well structure was studied where the aluminum concentration introduced a non-negligible

refractive index contrast between the well and barrier materials. The interaction of the Bloch modes of the photonic crystal and the collective behavior of each of the two material excitations (light and heavy hole excitons) formed a new kind of hybrid state called Bloch-polaritons. The angular dispersion of the three polariton branches were found to be in good agreement with transfer-matrix method calculations, based on rigorous theory that takes into account the coherent coupling between the quantum well layers. The polariton branches were also fitted to a three-coupled oscillator model which gave insight into the mixing coefficients of the photons, light-hole and heavy-hole excitons. Applying an electrical bias across the structure yielded large changes in the reflectivity spectra by transitioning the system between strong and weak coupling regimes. The unique dispersion properties of the polaritons can be implemented for slow-light enhanced nonlinear optics owing to its shallow dispersion.

(b) Further investigation of coherent interaction of quantum confined excitons were carried out in clusters of DNA linked colloidal quantum dots. In this system, coherent interaction is expected to manifest in the form of superradiant emission. Time-resolved photoluminescence measurements were carried out to determine if the system exhibits an enhancement in radiative rate. Statistical analysis of the measured radiative rates showed there

is no observable enhancement. Analysis of steady-state photoluminescence spectroscopic measurements suggest the lack of radiative enhancement is due to the large degree of inhomogeneous broadening of the QDs. Large inhomogeneous broadening decreases the probability of having two or more co-resonant quantum dots to be in in close proximity.

2. Resonant photonic structures in the form of microcavity systems were used to investigate the enhancement of light-matter interaction with colloidal quantum dots.

   (a) Low concentration of quantum dots were incorporated in the cavity layers by spin coating.

      i. Analysis of steady-state photoluminescence spectroscopic measurements showed the quantum dots to emit through the cavity resonance in a narrow emission spectrum. Power dependent photoluminescence measurements show a strictly linear dependence of peak emission intensity on the input power, and a lack of change in the emission linewidth. This lack of threshold behavior in the system is due to the low concentration of quantum dots, keeping the system below the gain threshold.

      ii. Although microcavity structures with low concentrations of quantum dots in the cavity layer were shown to be undesirable for observing gain, ultra-low concentrations can act as ideal microcavity enhanced

single-photon sources. To this end, the second-order coherence function of emitted photons from a ultra-low concentration microcavity was measured using a Hanbury Brown-Twiss interferometer to determine the temporal correlations of the emitted photons. Areas of single quantum dots were isolated using a fluorescence confocal imaging system. The fluorescence time trace of the quantum dots showed poor photostability. Although the coincidence histograms of single quantum dots were too noisy to observe antibunching, the sum of six different single quantum dot histograms showed a clear antibunching behavior.

(b) Microcavity structures with high concentrations of quantum dots were realized by the dip coating deposition technique.

   i. Time-resolved photoluminescence measurements performed on a microcavity incorporating a high concentration of quantum dots showed a Purcell enhancement factor of $\sim$1.3. Steady-stead power dependent photoluminescence measurements using a CW laser excitation source indicate enhanced emission intensity from quantum dots in the microcavity. However, when using a high power pulsed excitation source, threshold behavior of photoluminescence intensity is observed, indicating gain. The gain was observed at the biexciton energy. Furthermore, angle resolved photoluminescence measurements demonstrate the en-

hancement of gain due to the microcavity and highly directional emission. Although gain is observed in this structure, there is no evidence of lasing due to presence of fast nonradiative Auger recombination.

ii. The VSLM technique was implemented to characterize the gain profile of a drop coated film of quantum dots. The technique is robust, not being very sensitive to thickness variations, however it is rather sensitive to surface roughness where light propagating inside the photoinduced waveguide can be lost through scattering. Furthermore, direct calculations from the experimentally observed emission intensity provide a powerful means to determine modal gain beyond the gain saturation limit without the need for computationally expensive numerical fitting.

iii. Finally, coupled-cavity structures were utilized to investigate an all-optical analog of EIT-like features. Three different coupled-cavity structures with different degrees of coupling were realized where the resonances of the coupled system were measured spectroscopically. The intensity profiles were investigated through transfer-matrix method based calculations. The analysis determined the existance of a *bright* and *dark* cavity at the resonant wavelength. Incorporating quantum dots into each of these cavities resulted in resonant emission when the

quantum dots are placed in the *bright* cavity, however only uncoupled quantum dot emission was observed from quantum dots placed in the *dark* cavity. Such structures provide an all-optical method to investigate EIT-like behavior at room temperature using photons.

7.2 Outlook for Future Research

7.2.1 Bloch-Polaritons

Bloch-polaritons exhibit nonparabolic dispersion, making them a good candidate for nonlinear polariton-polariton scattering measurements. This kind of scattering experiment is carried out by sending a pump beam at an angle corresponding to the k_p (the parallel component of the wavevector). If the pump beam has enough power, two polaritons at k_p may scatter into a polariton at $k_{//} = 0$ (signal) and $2k_p$ (idler), where a probe beam at normal incidence can detect the signal polariton. A schematic of this scattering process is shown in figure 7.1. Such an investigation is yet to be carried out on Bloch-polaritons.

7.2.2 Quantum Dot Clusters

Quantum dot clusters provide an elegant means to investigate Dicke superradiance in semiconductor nanocrystals. The lack of superradiant emission in the work is

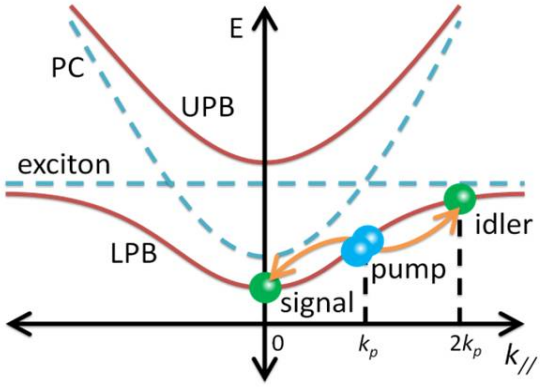

Figure 7.1: A schematic of polariton-polariton scattering where a pump beam is incident on the sample with $k_{//} = k_p$, create two polaritons in the lower polariton branch (LPB) which scatter to $k_{//} = 0$ and $k_{//} = 2k_p$.

attributed to the large inhomogeneous broadening of the quantum dots used. The large size distribution in colloidal quantum dots is a result of their synthesis, where the nanocrystal size increases with reaction time. The reason why colloidal quantum dots are very attractive is due to the ease with which different size (spectral emission) can be synthesized. There is a different variety of quantum dots know as magic-sized quantum dots. These nanocrystals are very stable and have a narrow size distribution (spectral linewidth) due to their "magic number" of atoms [116, 117]. These *magic dots* are a good candidate to observe superradiance in clusters due to their narrow size distribution.

7.2.3 Microcavity systems

The microcavity systems investigated in the work may be improved in two ways: increasing the Q factor of the cavities, and lowering the gain threshold of the quantum dots. A natural approach to accomplish this is to increase confinement in the cavity structures. This can be done by etching the one-dimensional planar cavity structures into pillars microcavities, greatly increasing the mode confinement and the Q factor. Spherical quantum dots do not seem to be a good choice for lasing applications due to the onset of nonradiative Auger recombination before gain occurs. Non-spherically shaped quantum dots which can significantly lower the gain threshold may be a better medium for implementation of lasing applications.

7.2.4 Coupled-Cavity Systems

Coupled-cavity structures have further potential in nonlinear scattering applications. It was shown recently that a triple cavity semiconductor system can undergo parametric oscillations [118]. This approach is yet to be explored in all-dielectric cavity systems.

Appendix

A Single Layer Films

```
%% Scattering calculations of a single layer on a substrate at ...
   normal incidence
% R = single_layer_thin_film(n1,n2,n3,t,lambda)
%   calculates reflectance
% [R,T] = single_layer_thin_film(n1,n2,n3,t,lambda)
%   calculates reflectance, and transmittance
% [R,T,A] = single_layer_thin_film(n1,n2,n3,t,lambda)
%   calculates reflectance, transmittance, and absorbance
% [R,...] = single_layer_thin_film(n1,...,lambda,angle)
% [R,...] = single_layer_thin_film(n1,...,lambda,angle,polarization)

%% input parameters:
% lambda = [1,n] vector of wavelengths
% n1 = refractive index above layer (typically air)
%   can be a scalar (dispersionless) or [1,n] vector where
%   n1(i) = refractive index at lambda(i)
% n2 = refractive index of layer
%   can be a scalar (dispersionless) or [1,n] vector
% n3 = refractive index of substrate
%   can be a scalar (dispersionless) or [1,n] vector
% t = thickness of n2 layer. Units must be the same as lambda
%%% OPTIONAL %%%
% angle = angle of incidence in degrees
% polarization = 'TE', 'S', 'TM', and 'P' are valid inputs

%%
function [R,varargout] = ...
   single_layer_thin_film(n1,n2,n3,t,lambda,varargin)

```

```
28 %
29 if nargin > 5
30     angle = varargin{1}*pi/180;
31     if nargin > 6
32         switch lower(varargin{2})
33             case {'s','te'}
34                 % defines terms used in coefficients
35                 q1=sqrt(n1.^2-(n1.^2)*(sin(angle))^2);
36                 q2=sqrt(n2.^2-(n1.^2)*(sin(angle))^2);
37                 q3=sqrt(n3.^2-(n1.^2)*(sin(angle))^2);
38                 % reflection and transmission coefficients
39                 r12=(q1-q2)./(q1+q2);
40                 r21=-r12;
41                 r23=(q2-q3)./(q2+q3);
42                 t12=2*q1./(q2+q1);
43                 t21=2*q2./(q1+q2);
44                 t23=2*q2./(q2+q3);
45                 k = 2*pi*q2./lambda;
46             case {'p','tm'}
47                 % defines terms used in coefficients
48                 q12=n1./n2.*sqrt(n2.^2-(n1.^2)*(sin(angle))^2);
49                 q21=n2./n1.*sqrt(n1.^2-(n1.^2)*(sin(angle))^2);
50                 q23=n2./n3.*sqrt(n3.^2-(n1.^2)*(sin(angle))^2);
51                 q32=n3./n2.*sqrt(n2.^2-(n1.^2)*(sin(angle))^2);
52                 % reflection and transmission coefficients
53                 r12=(q12-q21)./(q12+q21);
54                 r21=-r12;
55                 r23=(q23-q32)./(q23+q32);
56                 t12=2*(n1./n2.*q21)./(q21+q12);
57                 t21=2*(n2./n1.*q12)./(q12+q21);
58                 t23=2*(n2./n3.*q32)./(q32+q23);
59                 k = 2*pi*(n2./n1.*q12)./lambda;
60             otherwise
61                 % if polarization is unknown, display error message
62                 error(['''', varargin{2},''''', ' is not a valid ...
                       polarization. ',...
63                        'Valid input arguments are ''TE'', ''S'', ...
                          ''TM'', and ''P''.'])
64         end
65     else
66         % defines terms used in coefficients
67         q1=sqrt(n1.^2-(n1.^2)*(sin(angle))^2);
68         q2=sqrt(n2.^2-(n1.^2)*(sin(angle))^2);
69         q3=sqrt(n3.^2-(n1.^2)*(sin(angle))^2);
70         % reflection and transmission coefficients
71         r12=(q1-q2)./(q1+q2);
72         r21=-r12;
73         r23=(q2-q3)./(q2+q3);
74         t12=2*q1./(q2+q1);
```

```
        t21=2*q2./(q1+q2);
        t23=2*q2./(q2+q3);
        k = 2*pi*q2./lambda;
    end
else
    angle = 0;
    r12 = (n1-n2)./(n1+n2);
    r21 = -r12;
    t12 = 1+r12;
    t21 = 1+r21;

    r23 = (n2-n3)./(n2+n3);
%     r32 = -r23;
    t23 = 1+r23;
%     t32 = 1+r32;

    k = 2*pi*n2./lambda;
end

R = abs(r12 + (t12.*t21.*r23.*exp(2*i*k*t))./...
    (1-r21.*r23.*exp(2*i*k*t))).^2;

% R = abs((r12 + r23.*exp(2*i*k*t))./...
%     (1-r21.*r23.*exp(2*i*k*t))).^2;

if nargout > 1
    T = real(sqrt(n3.^2-(n1.^2)*(sin(angle))^2) ./ ...
        sqrt(n1.^2-(n1.^2)*(sin(angle))^2)).* ...
        abs(t23.*t12.*exp(i*k*t)./(1-r21.*r23.*exp(2*i*k*t))).^2;
    varargout{1} = T;
    if nargout > 2
        A = 1-(R+T);
        varargout{2} = A;
    end
end
```

B Multi-Layer Structures

```
%% Calculates the reflectance (R), transmittance (T), and absorbance (A)

%% Input parameters:
% lambda = [1,n] vector of wavelength
% width = [1,m] vector containing the width of each layer
%   width(1) = top layer, width(end) = bottom layer
%   units must be the same as lambda
% index = [m+1,n] matrix of the refractive indices of each layer
%   index(i,j) = index of the ith layer at lambda(j)
```

```
%   index(m+1,:) = refractive index of the substrate
% angles = [1,k] vector containing angles of incidence in degrees
% varargin = optional parameter for polarization
%   valid inputs are 'TE', 'TM', 'S', or 'P' default value = 'TE'
%
% Uses functions: propagator, and transfer_matrix
%%
function [R, T, A] = multi_layer(width, index, lambda, angles, varargin)

% check if polarization is specified
if nargin > 4
    % set polarization
    polarization = varargin{1};
else
    % set default polarization
    polarization = 'TE';
end

% defind nair
nair=1*ones(1,length(lambda));

% declare spectral variables
R = zeros(length(angles),length(lambda));
T = zeros(length(angles),length(lambda));
A = zeros(length(angles),length(lambda));

%%%% start calculations %%%%

% loop for each angle of incidence
for p=1:length(angles)
    % convert to radians
    angle = angles(p)*pi/180;

    % from air to first layer
    S = transfer_matrix([nair;index(1,:)],angle,nair,polarization);

    % all other layers
    for j=1:length(width)
        % propagation matrix jth layer
        Lj = propagator(lambda,width(j),index(j,:), nair, angle);
        % tranfer matrix from layer j to (j+1)
        Ijk = transfer_matrix([index(j,:);index(j+1,:)], angle, ...
            nair, polarization);

        % for each lambda
        for k=1:length(lambda)
            % transfer through layer j and into layer j+1
            S(:,:,k)=Ijk(:,:,k)*Lj(:,:,k)*S(:,:,k);
        end
```

```
58      end
59
60      % calculates R and T
61      R(p,:)=abs((S(2,1,:)./S(2,2,:))).^2;
62      % T = (n_subs*cos(theta_subs)/(n_1*cos(theta_1))*abs(t)^2
63      T(p,:)=real(reshape(...
64          abs(S(1,1,:)+S(1,2,:) .* (-S(2,1,:)./S(2,2,:))).^2, ...
                size(nair)).*...
65          sqrt(index(end,:).^2-(nair*sin(angle)).^2) ./ ...
                (nair*cos(angle)));
66
67      % absorbance
68      A(p,:)=1-R(p,:)-T(p,:);
69  end
```

```
1   function P = propagator(lambda,width,index,nair,angle)
2   % creates propagator matrix
3   % input argumants: wavelength (lambda) width of layer (width), index of
4   % current layer (index), index of air (nair), angle of incidence (angle)
5
6   % n_i*cos(theta_i)
7   q=sqrt(index.^2-(nair.^2)*(sin(angle))^2);
8   % perpendicular component of k
9   b=2*pi*q./lambda;
10
11  % creates propagator matrix P
12  P(1,1,:)=exp(i*b.*width);
13  P(1,2,:)=0;
14  P(2,1,:)=0;
15  P(2,2,:)=exp(-i*b.*width);
```

```
1   function S = transfer_matrix(index,angle,nair,varargin)
2   % returns transfer matrix for current interface
3   % inupt arguments: index matrix (containing index of currenr and next
4   % layer), angle of incidence, and index of air
5
6   % check is polarization is defined
7   if nargin > 3
8       switch lower(varargin{1})
9           case {'s','te'}
10              % defines terms used in transfer matrix
11              qj=sqrt(index(1,:).^2-(nair.^2)*(sin(angle))^2);
12              qk=sqrt(index(2,:).^2-(nair.^2)*(sin(angle))^2);
13              % reflection and transmission coefficients
14              rjk=(qj-qk)./(qj+qk);
15              tkj=2*qk./(qj+qk);
16          case {'p','tm'}
```

```
17              % defines terms used in transfer matrix
18              qj=index(1,:)./index(2,:).*sqrt(index(2,:).^2 - ...
                    (nair.^2)*(sin(angle))^2);
19              qk=index(2,:)./index(1,:).*sqrt(index(1,:).^2 - ...
                    (nair.^2)*(sin(angle))^2);
20              % reflection and transmission coefficients
21              rjk=(qj-qk)./(qj+qk);
22              tkj=2*qj./(qj+qk).*index(2,:)./index(1,:);
23          otherwise
24              % if polarization is unknown, display error message
25              error(['''', varargin{1},'''', ' is not a valid ...
                    polarization. ',...
26                  'Valid input arguments are ''TE'', ''S'', ''TM'', ...
                        and ''P''.'])
27      end
28  else
29      % if polarization is undefined, use defualt (TE)
30      % defines terms used in transfer matrix
31      qj=sqrt(index(1,:).^2-(nair.^2)*(sin(angle))^2);
32      qk=sqrt(index(2,:).^2-(nair.^2)*(sin(angle))^2);
33      % reflection and transmission coefficients
34      rjk=(qj-qk)./(qj+qk);
35      tkj=2*qk./(qj+qk);
36  end
37
38
39  % creates transfer matrix
40  S(1,1,:)=1./tkj;
41  S(1,2,:)=-rjk./tkj;
42  S(2,1,:)=S(1,2,:);
43  S(2,2,:)=S(1,1,:);
```

C Electric Field Intensity Profile MATLAB Codes

```
1  function [pos, Efield, nval] = ...
       Efield_func(index,width,lambda,angle,steps,varargin)
2
3  % check if polarization is specified
4  if nargin > 5
5      % set polarization
6      polarization = varargin{1};
7  else
8      % set default polarization
9      polarization = 'TE';
10 end
11
12 lambda_res = length(lambda);
```

```
13 nair = ones(size(index(1,:)));
14
15 S = transfer_matrix([nair;index(1,:)], angle, nair, polarization);
16
17 Sright = zeros(2,2,length(width),length(lambda));
18
19 bj = zeros(length(width),length(lambda));
20
21 for j=1:length(width)
22     % n_j*cos(theta_j)
23     qj=sqrt(index(j,:).^2-(nair.^2)*(sin(angle))^2);
24     % k for jth layer
25     bj(j,:)=2*pi*qj./lambda;
26     % propagator for jth layer
27     Lj = propagator(lambda,width(j),index(j,:), nair, angle);
28     % transfer matrix from layer j to layer j+1
29     Ijk = transfer_matrix([index(j,:);index(j+1,:)], angle, nair, ...
           polarization);
30     % total transfer matrix from the first to the jth layer
31     Sright(:,:,j,:) = S(:,:,:);
32     % for each wavelength
33     for k=1:length(lambda)
34         % transfer through the jth layer and into layer j+1
35         S(:,:,k)=Ijk(:,:,k)*Lj(:,:,k)*S(:,:,k);
36     end
37 end
38
39 % declare vector
40 % layerpos(k) is the position of the top of the kth layer
41 layerpos = zeros(1,length(width)+1);
42 for k=1:length(width)
43     % postion of layer k+1 is the postion of kth + width of kth layer
44     layerpos(k+1)=layerpos(k)+width(k);
45 end
46
47 % declare variables
48 % [1,steps] vector of the position along the entire structure
49 pos=linspace(0,layerpos(end),steps);
50 % nval(i,j) = refactive index at pos(i) and lambda(j)
51 nval = zeros(steps,lambda_res);
52 % reflection coefficient the entire structure for each lambda
53 r(1,1,1,:) = -S(2,1,:)./S(2,2,:);
54 % declare variable: Efield(i,j) = e-filed intensity at pos(i) and ...
       lambda(j)
55 Efield = zeros(steps,lambda_res);
56
57 % for each position
58 for k=1:steps
59     % find the layer corresponding to pos(k)
```

```
60      for j=1:length(width)
61          % find layer in which pos(k) is located
62          if pos(k)<layerpos(j+1)
63              % j points to current layer
64              break;
65          end
66      end
67      %dj=width(j);
68      % sets nval to the index of the layer
69      nval(k,:) = index(j,:);
70      % defines the depth from the beginning of the layer
71      x=pos(k)-layerpos(j);
72      % the amplitude of the forward traveling wave
73      tpos = Sright(1,1,j,:)+r.*Sright(1,2,j,:);
74      % the amplitude of the backward traveling wave
75      tneg = Sright(2,1,j,:)+r.*Sright(2,2,j,:);
76      % reshape them to have dimensions [1,lambda_res]
77      tpos = reshape(tpos,1,lambda_res);
78      tneg = reshape(tneg,1,lambda_res);
79      % calculates the intensity
80      Efield(k,:)=(abs(tpos.*exp(i*bj(j,:)*x) + ...
            tneg.*exp(-i*bj(j,:)*x))).^2;
81  end
```

D Coupled Oscillator Model

```
1  % Computes the the error of a coupled oscillator model
2  % to data points
3  %
4  % Designed to be used as input function handle
5  % for MATLAB function lsqnonlin, which find finds the input vector 'x',
6  % for which returns the least-squared error (output of this function)
7
8  function error = bragg_fit_func(x)
9
10 V1 = x(1);% Eph-E1 coupling
11 V2 = x(2);% Eph-E2 coupling
12 E0 = x(3);% Eph at angle=0
13 n = x(4); % effective refractive index for disperion model
14 E1 = x(5);% uncoupled E1
15 E2 = x(6);% uncoupled E2
16
17 % loads dispersion data from file disp_data.mat
18 % can be done directly with .txt or .dat file, but
19 % MATLAB imports .mat files significantly fast
20
21 load('disp_data');
```

```
% loads variables:
% angles - column vector of length N - number of angle (in degrees)
% vals - N-by-3 matrix of the branch energies in descending order
%   vals(i,1) > vals(i,2) > vals(i,3), for i = 1:N
%   vals may have NaN elements


% define theta in radians
theta=angles*pi/180;
% model for photon energy dipersion
Eph=E0./sqrt(1-(sin(theta)/n).^2);
% declares variable for calculated energies
result = zeros(length(Eph),3);

% loop for each angle
for i=1:length(Eph)
    % define Hamiltonian
    H=[Eph(i),V1,V2;V1,E1,0;V2,0,E2];
    % find eigenvlues H, flips to sort in descending order
    result(i,:)=fliplr(eig(H)');
end

% find indices of non-NaN elements
ind = find(~isnan(vals));
% computes error/deviation at each non-NaN element
% function lsqnonlin will minimize sum(error.^2)
error = result(ind)-vals(ind);
```

```
% Plots the branch energies of a coupled oscillator model
% to data points
%
% Designed to be used with the output vector 'x'from function MATLAB
% function lsqnonlin, with input function handle @bragg_fit_func

function bragg_fit_plot(x)

V1 = x(1);% Eph-E1 coupling
V2 = x(2);% Eph-E2 coupling
E0 = x(3);% Eph at angle=0
n = x(4); % effective refractive index for disperion model
E1 = x(5);% uncoupled E1
E2 = x(6);% uncoupled E2

% loads dispersion data from file disp_data.mat
% can be done directly with .txt or .dat file, but
% MATLAB imports .mat files significantly fast

load('disp_data');
```

```
% loads variables:
% angles — column vector of length N — number of angle (in degrees)
% vals — N—by—3 matrix of the branch energies in descending order
%   vals(i,1) > vals(i,2) > vals(i,3), for i = 1:N
%   vals may have NaN elements
angles_data = angles;

% define angles for calculation
angles = [0:90]';

% define theta in radians
theta=angles*pi/180;
% model for photon energy dipersion
Eph=E0./sqrt(1—(sin(theta)/n).^2);
% declares variable for calculated mixing coefficients
% of the form coeff(angle,type,branch)
coeff=zeros(length(Eph),3,3);
% declares variable for calculated energies
result = zeros(length(Eph),3);

% loop for each angle
for i=1:length(Eph)
    % define Hamiltonian
    H=[Eph(i),V1,V2;V1,E1,0;V2,0,E2];
    % find eigenvlues D, and eigenvectors V
    [V,D]=eig(H);
    % transforms to vector from diagonal matrrix and
    % flips to sort in descending order of eigenvalue
    result(i,:)=fliplr((D*ones(3,1))');
    % squares the coeffs of unit eigenvectors and
    % flips to sort in descending order
    coeff(i,:,:)=fliplr(V.^2);
end

% plot uncoupled energies
subplot(3,2,[1,3,5])
plot(angles, [E1*ones(size(angles)), E2*ones(size(angles)), Eph],...
    '—-k',angles, result);
hold on
% plot data points
plot(angles_data, vals,'o');
hold off
% plot first branch (highest energy)
subplot(3,2,2);
plot(angles, coeff(:,:,1));
legend('\alpha^2', '\beta^2', '\gamma^2');
% plot second branch
subplot(3,2,4);
plot(angles, coeff(:,:,2));
```

```
70 legend('\alpha^2', '\beta^2', '\gamma^2');
71 % plot third branch
72 subplot(3,2,6);
73 plot(angles, coeff(:,:,3));
74 legend('\alpha^2', '\beta^2', '\gamma^2');
```

Bibliography

[1] Peter Y. Yu and Manuel Cardona. *Fundamentals of Semiconductors: Physics and Materials Properties*. Springer, 2010. ISBN 3642007090.

[2] J. Frenkel. On the transformation of light into heat in solids. i. *Phys. Rev.*, 37: 17–44, Jan 1931. doi: 10.1103/PhysRev.37.17. URL `http://link.aps.org/doi/10.1103/PhysRev.37.17`.

[3] J. Frenkel. On the transformation of light into heat in solids. ii. *Phys. Rev.*, 37:1276–1294, May 1931. doi: 10.1103/PhysRev.37.1276. URL `http://link.aps.org/doi/10.1103/PhysRev.37.1276`.

[4] Gregory H. Wannier. The structure of electronic excitation levels in insulating crystals. *Phys. Rev.*, 52:191–197, Aug 1937. doi: 10.1103/PhysRev.52.191. URL `http://link.aps.org/doi/10.1103/PhysRev.52.191`.

[5] N. F. Mott. Conduction in polar crystals. ii. the conduction band and ultra-violet absorption of alkali-halide crystals. *Trans. Faraday Soc.*, 34:500–506, 1938. doi: 10.1039/TF9383400500. URL `http://dx.doi.org/10.1039/TF9383400500`.

[6] Eli Yablonovitch. Inhibited spontaneous emission in solid-state physics and electronics. *Phys. Rev. Lett.*, 58:2059–2062, May 1987. doi: 10.1103/PhysRevLett.58.2059. URL `http://link.aps.org/doi/10.1103/PhysRevLett.58.2059`.

[7] Sajeev John. Strong localization of photons in certain disordered dielectric superlattices. *Phys. Rev. Lett.*, 58:2486–2489, Jun 1987. doi:

10.1103/PhysRevLett.58.2486. URL http://link.aps.org/doi/10.1103/PhysRevLett.58.2486.

[8] Lord Rayleigh. Xxv. on the reflexion of light at a twin plane of a crystal. *Philosophical Magazine Series 5*, 26(160):241–255, 1888. doi: 10.1080/14786448808628258. URL http://www.tandfonline.com/doi/abs/10.1080/14786448808628258.

[9] Vladimir P Bykov. Spontaneous emission in a periodic structure. *Soviet Journal of Experimental and Theoretical Physics*, 35:269–273, 1972.

[10] Vladimir P Bykov. Spontaneous emission from a medium with a band spectrum. *Sov. J. Quantum Electron.*, 4:861–871, 1975.

[11] T. Baba, T. Hamano, F. Koyama, and K. Iga. Spontaneous emission factor of a microcavity dbr surface-emitting laser. *Quantum Electronics, IEEE Journal of*, 27(6):1347 –1358, jun 1991. doi: 10.1109/3.89951.

[12] D. G. Deppe and C. Lei. Spontaneous emission and optical gain in a fabry–perot microcavity. *Appl. Phys. Lett.*, 60(5):527–529, 1992. doi: 10.1063/1.106596. URL http://link.aip.org/link/?APL/60/527/1.

[13] Desmond V. O'Connor and David Phillips. *Time-Correlated Single Photon Counting*. Academic Press, 1984. ISBN 0125241402.

[14] Joseph R. Lakowicz. *Principles of Fluorescence Spectroscopy*. Springer, 2006. ISBN 0387312781.

[15] Priscilla E. Greenwood and Michael S. Nikulin. *A Guide to Chi-Squared Testing*. Wiley, 1996. ISBN 047155779X.

[16] R H Dicke. Coherence in Spontaneous Radiation Processes. *Phys. Rev.*, 93(1): 99–110, January 1954. doi: 10.1103/PhysRev.93.99.

[17] E L Ivchenko, A I Nesvizhskii, and S Jorda. Bragg reflection of light from quantum well structures. *Phys. Solid State*, 36:1156–1161, 1994.

[18] M. Hübner, J. P. Prineas, C. Ell, P. Brick, E. S. Lee, G. Khitrova, H. M. Gibbs, and S. W. Koch. Optical lattices achieved by excitons in periodic quantum well structures. *Phys. Rev. Lett.*, 83:2841–2844, Oct 1999. doi: 10.1103/PhysRevLett.83.2841. URL `http://link.aps.org/doi/10.1103/PhysRevLett.83.2841`.

[19] L. I. Deych and A. A. Lisyansky. Polariton dispersion law in periodic-bragg and near-bragg multiple quantum well structures. *Phys. Rev. B*, 62:4242–4244, Aug 2000. doi: 10.1103/PhysRevB.62.4242. URL `http://link.aps.org/doi/10.1103/PhysRevB.62.4242`.

[20] J P Prineas, C Ell, E S Lee, G Khitrova, H M Gibbs, and S W Koch. multiple-quantum-well periodic structures. *Phys. Rev. B*, 61(20):863–872, 2000.

[21] M. V. Erementchouk, L. I. Deych, and a. a. Lisyansky. Optical properties of one-dimensional photonic crystals based on multiple-quantum-well structures. *Phys. Rev. B*, 71(23):1–11, June 2005. ISSN 1098-0121. doi: 10.1103/PhysRevB.71.235335. URL `http://link.aps.org/doi/10.1103/PhysRevB.71.235335`.

[22] E. L. Ivchenko. *Fiz. Tverd. Tela (Leningrad)*, 33:2388, 1991.

[23] E. L. Ivchenko and M. Willander. Exciton polaritons in periodic nanostructures. *Physica Status Solidi (b)*, 215(1):199–209, 1999. ISSN 1521-3951.

[24] E. L. Ivchenko, M. M. Voronov, M. V. Erementchouk, L. I. Deych, and A. A. Lisyansky. Multiple-quantum-well-based photonic crystals with simple and compound elementary supercells. *Phys. Rev. B*, 70:195106, Nov 2004. doi: 10.1103/PhysRevB.70.195106. URL `http://link.aps.org/doi/10.1103/PhysRevB.70.195106`.

[25] G. Birkl, M. Gatzke, I. H. Deutsch, S. L. Rolston, and W. D. Phillips. Bragg scattering from atoms in optical lattices. *Phys. Rev. Lett.*, 75:2823–2826, Oct 1995. doi: 10.1103/PhysRevLett.75.2823. URL `http://link.aps.org/doi/10.1103/PhysRevLett.75.2823`.

[26] T. Ikawa and K. Cho. Fate of the superradiant mode in a resonant bragg reflector. *Phys. Rev. B*, 66:085338, 2002.

[27] M. Werchner, M. Schafer, M. Kira, S. W. Koch, J. Sweet, J. D. Olitzky, J. Hendrickson, B. C. Richards, G. Khitrova, H. M. Gibbs, A. N. Poddubny, E. L. Ivchenko, M. Voronov, and M. Wegener. One dimensional resonant fibonacci quasicrystals: noncanonical linear andcanonical nonlinear effects. *Opt. Express*, 17(8):6813–6828, 2009.

[28] E. L. Ivchenko, V. P. Kochereshko, A. V. Platonov, D. R. Yakovlev, A. Waag, W. Ossau, and G. Landwehr. Resonance optical spectroscopy of long-period quantum-well structures. *Phys. Solid State*, 39:1852–1858, Nov. 1997.

[29] M. V. Erementchouk, L. I. Deych, and A. A. Lisyansky. Spectral properties of exciton polaritons in one-dimensional resonant photonic crystals. *Phys. Rev. B*, 73(11):115321, 2006.

[30] Fabio Biancalana, Leonidas Mouchliadis, Celestino Creatore, Simon Osborne, and Wolfgang Langbein. Microcavity polaritonlike dispersion doublet in resonant bragg gratings. *Phys. Rev. B*, 80:121306, Sep 2009. doi: 10.1103/PhysRevB.80.121306. URL `http://link.aps.org/doi/10.1103/PhysRevB.80.121306`.

[31] Alexey V. Kavokin and Mikhail A. Kaliteevski. Light-absorption effect on bragg interference in multilayer semiconductor heterostructures. *J. Appl. Phys.*, 79: 595–598, 1996.

[32] D. Ammerlahn, B. Grote, S. W. Koch, J. Kuhl, M. Hübner, R. Hey, and

K. Ploog. Influence of the dielectric environment on the radiative lifetime of quantum-well excitons. *Phys. Rev. B*, 61:4801–4805, 2000.

[33] Kazuhiro Sumioka, Hiroyuki Nagahama, and Tetsuo Tsutsui. Strong coupling of exciton and photon modes in photonic crystal infiltrated with organic–inorganic layered perovskite. *Appl. Phys. Lett.*, 78(10):1328–1330, 2001.

[34] J. Kasprzak, M. Richard, S. Kundermann, A. Baas, P. Jeambrun, J. M. J. Keeling, F. M. Marchetti, M. H. Szymanska, R. André, J. L. Staehli, V. Savona, P. B. Littlewood, B. Deveaud, and L. S. Dang. Bose–einstein condensation of exciton polaritons. *Nature*, 443:409–414, 2006.

[35] A. Amo, D. Sanvitto, F. P. Laussy, D. Ballarini, E. del Valle, M. D. Martin, A. Lemaitre, J. Bloch, D. N. Krizhanovskii, M. S. Skolnick, C. Tejedor, and L. Vina. Collective fluid dynamics of a polariton condensate in a semiconductor microcavity. *Nature*, 457:291–296, 2009.

[36] D. Gerace, H. E. Türeci, A. Imamoglu, V. Giovannetti, and R. Fazio. The quantum-optical josephson interferometer. *Nature Phys.*, 5:281–284, 2009.

[37] R. Balili, V. Hartwell, D. Snoke, L. Pfeiffer, and K. West. Bose-Einstein Condensation of Microcavity Polaritons in a Trap. *Science*, 316(5827):1007–1010, 2007. doi: 10.1126/science.1140990. URL `http://www.sciencemag.org/cgi/content/abstract/316/5827/1007`.

[38] M. Saba, C. Ciuti, J. Bloch, V. Thierry-Mieg, R. André, L. S. Dang, S. Kundermann, A. Mura, G. Bongiovanni, J. L. Staehli, and B. Deveaud. High-temperature ultrafast polariton parametric amplification in semiconductor microcavities. *Nature*, 414:731–735, 2001.

[39] David G. Lidzey, Donal D. C. Bradley, Adam Armitage, Steve Walker, and Maurice S. Skolnick. Photon-mediated hybridization of frenkel excitons in organic semiconductor microcavities. *Science*, 288(5471):1620–1623, June 2000.

[40] T. Westgaard, Q. X. Zhao, B. O. Fimland, K. Johannessen, and L. Johnsen. Optical properties of excitons in gaas/$al0.3ga0.7$as symmetric double quantum wells. *Phys. Rev. B*, 45(4):1784–1792, Jan 1992. doi: 10.1103/PhysRevB.45.1784.

[41] I. Linnerud and K. A. Chao. Exciton binding energies and oscillator strengths in a symmetric al_xga_{1-x}as/gaas double quantum well. *Phys. Rev. B*, 49(12):8487–8490, Mar 1994. doi: 10.1103/PhysRevB.49.8487.

[42] J. Soubusta, R. Grill, P. Hlídek, M. Zvára, L. Smrčka, S. Malzer, W. Geißelbrecht, and G. H. Döhler. Excitonic photoluminescence in symmetric coupled double quantum wells subject to an external electric field. *Phys. Rev. B*, 60(11):7740–7743, Sep 1999. doi: 10.1103/PhysRevB.60.7740.

[43] Mathew M Maye, Mudalige Thilak Kumara, Dmytro Nykypanchuk, William B Sherman, and Oleg Gang. Switching binary states of nanoparticle superlattices and dimer clusters by DNA strands. *Nat Nano*, 5(2):116–20, February 2010. ISSN 1748-3395. doi: 10.1038/nnano.2009.378. URL `http://www.ncbi.nlm.nih.gov/pubmed/20023646`.

[44] C. Knorowski, S. Burleigh, and A. Travesset. Dynamics and statics of dna-programmable nanoparticle self-assembly and crystallization. *Phys. Rev. Lett.*, 106:215501, May 2011. doi: 10.1103/PhysRevLett.106.215501. URL `http://link.aps.org/doi/10.1103/PhysRevLett.106.215501`.

[45] Francisco J. Martinez-Veracoechea, Bianca M. Mladek, Alexei V. Tkachenko, and Daan Frenkel. Design rule for colloidal crystals of dna-functionalized particles. *Phys. Rev. Lett.*, 107:045902, Jul 2011. doi: 10.1103/PhysRevLett.107.045902. URL `http://link.aps.org/doi/10.1103/PhysRevLett.107.045902`.

[46] Yugang Zhang, Fang Lu, Daniel van der Lelie, and Oleg Gang. Continuous phase transformation in nanocube assemblies. *Phys. Rev. Lett.*, 107:135701, Sep 2011.

doi: 10.1103/PhysRevLett.107.135701. URL http://link.aps.org/doi/10.1103/PhysRevLett.107.135701.

[47] Dazhi Sun and Oleg Gang. Binary heterogeneous superlattices assembled from quantum dots and gold nanoparticles with dna. *Journal of the American Chemical Society*, 133(14):5252–5254, 2011. doi: 10.1021/ja111542t. URL http://pubs.acs.org/doi/abs/10.1021/ja111542t.

[48] C. Knorowski and A. Travesset. Materials design by dna programmed self-assembly. *Current Opinion in Solid State and Materials Science*, 15(6):262 – 270, 2011. ISSN 1359-0286. doi: 10.1016/j.cossms.2011.07.002. URL http://www.sciencedirect.com/science/article/pii/S1359028611000556. ¡ce:title¿Functional Gels and Membranes¡/ce:title¿.

[49] Oleg Gang and Yugang Zhang. Shaping phases by phasing shapes. *ACS nano*, 5(11):8459–8465, November 2011. ISSN 1936-086X. doi: 10.1021/nn2041363. URL http://www.ncbi.nlm.nih.gov/pubmed/22103256.

[50] Trung Dac Nguyen, Eric Jankowski, and Sharon C Glotzer. Self-assembly and reconfigurability of shape-shifting particles. *ACS nano*, 5(11):8892–903, November 2011. ISSN 1936-086X. doi: 10.1021/nn203067y. URL http://www.ncbi.nlm.nih.gov/pubmed/21950837.

[51] Alex Travesset. Self-Assembly Enters the Design Era. *Science*, 334(October): 183–184, 2011.

[52] MathewM. Maye, Dmytro Nykypanchuk, Daniel vanderLelie, and Oleg Gang. Dna-regulated micro- and nanoparticle assembly. *Small*, 3(10):1678–1682, 2007. ISSN 1613-6829. doi: 10.1002/smll.200700357. URL http://dx.doi.org/10.1002/smll.200700357.

[53] Huiming Xiong, Daniel van der Lelie, and Oleg Gang. Phase Behavior of Nanoparticles Assembled by DNA Linkers. *Phys. Rev. Lett.*, 102(1):12–15,

January 2009. ISSN 0031-9007. doi: 10.1103/PhysRevLett.102.015504. URL http://link.aps.org/doi/10.1103/PhysRevLett.102.015504.

[54] Mathew M Maye, Dmytro Nykypanchuk, Marine Cuisinier, Daniel van der Lelie, and Oleg Gang. Stepwise surface encoding for high-throughput assembly of nanoclusters. *Nat Mater*, 8(5):388–91, May 2009. ISSN 1476-1122. doi: 10.1038/nmat2421. URL http://www.ncbi.nlm.nih.gov/pubmed/19329992.

[55] M. D. Leistikow, J. Johansen, A. J. Kettelarij, P. Lodahl, and W. L. Vos. Size-dependent oscillator strength and quantum efficiency of cdse quantum dots controlled via the local density of states. *Phys. Rev. B*, 79:045301, Jan 2009. doi: 10.1103/PhysRevB.79.045301. URL http://link.aps.org/doi/10.1103/PhysRevB.79.045301.

[56] E. M. Purcell. Spontaneous Emission Probabilities at Radio Frequencies. *Phys. Rev.*, 69:681, 1946.

[57] Daniel Kleppner. Inhibited spontaneous emission. *Phys. Rev. Lett.*, 47:233–236, Jul 1981. doi: 10.1103/PhysRevLett.47.233. URL http://link.aps.org/doi/10.1103/PhysRevLett.47.233.

[58] A. V. Malko, A. A. Mikhailovsky, M. A. Petruska, J. A. Hollingsworth, H. Htoon, M. G. Bawendi, and V. I. Klimov. From amplified spontaneous emission to microring lasing using nanocrystal quantum dot solids. *Applied Physics Letters*, 81(7):1303–1305, 2002. doi: 10.1063/1.1497708. URL http://link.aip.org/link/?APL/81/1303/1.

[59] Xudong Fan, Mark C. Lonergan, Yuzhong Zhang, and Hailin Wang. Enhanced spontaneous emission from semiconductor nanocrystals embedded in whispering gallery optical microcavities. *Phys. Rev. B*, 64:115310, Aug 2001. doi: 10.1103/PhysRevB.64.115310. URL http://link.aps.org/doi/10.1103/PhysRevB.64.115310.

[60] R. J. Horowicz, H. Heitmann, Y. Kadota, and Y. Yamamoto. Gaas microcavity quantum-well laser with enhanced coupling of spontaneous emission to the lasing mode. *Applied Physics Letters*, 61(4):393–395, 1992. doi: 10.1063/1.107893. URL http://link.aip.org/link/?APL/61/393/1.

[61] G. Bjork. On the spontaneous lifetime change in an ideal planar microcavity-transition from a mode continuum to quantized modes. *IEEE Journal of Quantum Electronics*, 30(10):2314–2318, 1994. ISSN 00189197. doi: 10.1109/3.328610. URL http://ieeexplore.ieee.org/lpdocs/epic03/wrapper.htm?arnumber=328610.

[62] Fumio Koyama, Susumu Kinoshita, and Kenichi Iga. Room-temperature continuous wave lasing characteristics of a gaas vertical cavity surface-emitting laser. *Applied Physics Letters*, 55(3):221–222, 1989. doi: 10.1063/1.101913. URL http://link.aip.org/link/?APL/55/221/1.

[63] J. L. Jewell, K. F. Huang, K. Tai, Y. H. Lee, R. J. Fischer, S. L. McCall, and A. Y. Cho. Vertical cavity single quantum well laser. *Applied Physics Letters*, 55 (5):424–426, 1989. doi: 10.1063/1.101885. URL http://link.aip.org/link/?APL/55/424/1.

[64] Y. Chan, J.-Michel Caruge, P. T. Snee, and M. G. Bawendi. Multiexcitonic two-state lasing in a cdse nanocrystal laser. *Applied Physics Letters*, 85(13):2460–2462, 2004. doi: 10.1063/1.1795368. URL http://link.aip.org/link/?APL/85/2460/1.

[65] Bumki Min, Sungjee Kim, Koichi Okamoto, Lan Yang, Axel Scherer, Harry Atwater, and Kerry Vahala. Ultralow threshold on-chip microcavity nanocrystal quantum dot lasers. *Applied Physics Letters*, 89(19):191124, 2006. doi: 10.1063/1.2387966. URL http://link.aip.org/link/?APL/89/191124/1.

[66] Carl B. Poitras, Michal Lipson, Hui Du, Megan A. Hahn, and Todd D. Krauss. Photoluminescence enhancement of colloidal quantum dots embedded in a

monolithic microcavity. *Applied Physics Letters*, 82(23):4032–4034, 2003. doi: 10.1063/1.1581007. URL http://link.aip.org/link/?APL/82/4032/1.

[67] S. Rabaste, J. Bellessa, C. Bonnand, J. C. Plenet, and L. Spanhel. Microcavity strongly doped with CdSe nanocrystals. *Eur. Phys. J. B*, 42(1):47–50, November 2004. ISSN 1434-6028. doi: 10.1140/epjb/e2004-00356-9. URL http://www.springerlink.com/index/10.1140/epjb/e2004-00356-9.

[68] Xiaoyong Wang, Chih-Kang Shih, Jianfeng Xu, and Min Xiao. Enhanced dipole-dipole interaction of cdse/cds nanocrystal quantum dots inside a planar microcavity. *Applied Physics Letters*, 89(11):113114, 2006. doi: 10.1063/1.2352802. URL http://link.aip.org/link/?APL/89/113114/1.

[69] Matthias Kahl, Tim Thomay, Verena Kohnle, Katja Beha, Jrg Merlein, Matthias Hagner, Andreas Halm, Jan Ziegler, Thomas Nann, Yuri Fedutik, Ulrike Woggon, Mikhail Artemyev, Fabin Prez-Willard, Alfred Leitenstorfer, and Rudolf Bratschitsch. Colloidal quantum dots in all-dielectric high-q pillar microcavities. *Nano Letters*, 7(9):2897–2900, 2007. doi: 10.1021/nl071812x. URL http://pubs.acs.org/doi/abs/10.1021/nl071812x.

[70] Jacek Jasieniak, Cinzia Sada, Alessandro Chiasera, Maurizio Ferrari, Alessandro Martucci, and Paul Mulvaney. Sol-Gel Based Vertical Optical Microcavities with Quantum Dot Defect Layers. *Adv. Funct. Mater*, 18(23):3772–3779, December 2008. ISSN 1616301X. doi: 10.1002/adfm.200800784. URL http://doi.wiley.com/10.1002/adfm.200800784.

[71] V. M. Menon, M. Luberto, N. V. Valappil, and S. Chatterjee. Lasing from ingap quantum dots in aspin-coated flexible microcavity. *Opt. Express*, 16 (24):19535–19540, Nov 2008. doi: 10.1364/OE.16.019535. URL http://www.opticsexpress.org/abstract.cfm?URI=oe-16-24-19535.

[72] Cuong Dang, Joonhee Lee, Craig Breen, Jonathan S. Steckel, Seth Coe-Sullivan, and Arto Nurmikko. Red, green and blue lasing enabled by single-exciton gain

in colloidal quantum dot films. *Nat Nano*, 7:335–339. doi: 10.1038/nnano.2012.61. URL http://www.nature.com/nnano/journal/v7/n5/abs/nnano.2012.61.html.

[73] Christopher Gerry and Peter Knight. *Introductory Quantum Optics*. Cambridge University Press, 2004. ISBN 052152735X.

[74] R. Hanbury Brown and R. Q. Twiss. Correlation between photons in two coherent beams of light. *Nature*, 177:27–29, 1956. doi: 10.1038/177027a0. URL http://dx.doi.org/10.1038/177027a0.

[75] F. Davidson and L. Mandel. Photoelectric correlation measurements with time-to-amplitude converters. *Journal of Applied Physics*, 39(1):62–66, 1968. doi: 10.1063/1.1655781. URL http://link.aip.org/link/?JAP/39/62/1.

[76] S. Chopra and L. Mandel. An electronic correlator for photoelectric correlation measurements. *Review of Scientific Instruments*, 43(10):1489–1491, 1972. doi: 10.1063/1.1685472. URL http://link.aip.org/link/?RSI/43/1489/1.

[77] Svetlana G. Lukishova, Luke J. Bissell, Vinod M. Menon, Nikesh Valappil, Megan A. Hahn, Chris M. Evans, Brandon Zimmerman, Todd D. Krauss, C.R. Stroud, and Robert W. Boyd. Organic photonic bandgap microcavities doped with semiconductor nanocrystals for room-temperature on-demand single-photon sources. *Journal of Modern Optics*, 56(2-3):167–174, 2009. doi: 10.1080/09500340802410106. URL http://www.tandfonline.com/doi/abs/10.1080/09500340802410106.

[78] Luke J. Bissell. *Experimental Realization of Efficient, Room Temperature Single-Photon Sources with Definite Circular and Linear Polarizations*. PhD thesis, The Institute of Optics, University of Rochester, 2011.

[79] Victor I. Klimov, Sergei A. Ivanov, Jagjit Nanda, Marc Achermann, Ilya Bezel, John A. McGuire, and Andrei Piryatinski. Single-exciton optical gain

in semiconductor nanocrystals. *Nature*, 447(7143):441–446, May 2007. ISSN 1476-4687. doi: 10.1038/nature05839. URL http://www.ncbi.nlm.nih.gov/pubmed/17522678.

[80] V. I. Klimov, A. A. Mikhailovsky, Su Xu, A. Malko, J. A. Hollingsworth, C. A. Leatherdale, H.-J. Eisler, and M. G. Bawendi. Optical Gain and Stimulated Emission in Nanocrystal Quantum Dots. *Science*, 290(5490):314–317, October 2000. ISSN 00368075. doi: 10.1126/science.290.5490.314. URL http://www.sciencemag.org/cgi/doi/10.1126/science.290.5490.314.

[81] A. A. Mikhailovsky, A. V. Malko, J. A. Hollingsworth, M. G. Bawendi, and V. I. Klimov. Multiparticle interactions and stimulated emission in chemically synthesized quantum dots. *Applied Physics Letters*, 80(13):2380–2382, 2002. doi: 10.1063/1.1463704. URL http://link.aip.org/link/?APL/80/2380/1.

[82] Lin-Wang Wang, Marco Califano, Alex Zunger, and Alberto Franceschetti. Pseudopotential theory of auger processes in cdse quantum dots. *Phys. Rev. Lett.*, 91:056404, Jul 2003. doi: 10.1103/PhysRevLett.91.056404. URL http://link.aps.org/doi/10.1103/PhysRevLett.91.056404.

[83] J.-Michel Caruge, Yinthai Chan, V. Sundar, H. J. Eisler, and Moungi G. Bawendi. Transient photoluminescence and simultaneous amplified spontaneous emission from multiexciton states in CdSe quantum dots. *Phys. Rev. B*, 70:085316, Aug 2004. doi: 10.1103/PhysRevB.70.085316. URL http://link.aps.org/doi/10.1103/PhysRevB.70.085316.

[84] Multiexciton fluorescence from semiconductor nanocrystals. *Chemical Physics*, 318(1-2):71 – 81, 2005.

[85] Dipankar Chattarji. *The theory of Auger Transitions*. Academic Press, 1976. ISBN 0121698505.

[86] Peter T. Landsberg. *Recombination in Semiconductors*. Cambridge University Press, 2003. ISBN 0521543436.

[87] Feng Wang, Yang Wu, Mark S. Hybertsen, and Tony F. Heinz. Auger recombination of excitons in one-dimensional systems. *Phys. Rev. B*, 73:245424, Jun 2006. doi: 10.1103/PhysRevB.73.245424. URL `http://link.aps.org/doi/10.1103/PhysRevB.73.245424`.

[88] Samuel L. Sewall, Alberto Franceschetti, Ryan R. Cooney, Alex Zunger, and Patanjali Kambhampati. Direct observation of the structure of band-edge biexcitons in colloidal semiconductor cdse quantum dots. *Phys. Rev. B*, 80:081310, Aug 2009. doi: 10.1103/PhysRevB.80.081310. URL `http://link.aps.org/doi/10.1103/PhysRevB.80.081310`.

[89] Patanjali Kambhampati. Unraveling the structure and dynamics of excitons in semiconductor quantum dots. *Accounts of Chemical Research*, 44(1):1–13, 2011. doi: 10.1021/ar1000428. URL `http://pubs.acs.org/doi/abs/10.1021/ar1000428`.

[90] Samuel L. Sewall, Ryan R. Cooney, Eva A. Dias, Pooja Tyagi, and Patanjali Kambhampati. State-resolved observation in real time of the structural dynamics of multiexcitons in semiconductor nanocrystals. *Phys. Rev. B*, 84:235304, Dec 2011. doi: 10.1103/PhysRevB.84.235304. URL `http://link.aps.org/doi/10.1103/PhysRevB.84.235304`.

[91] Sergei A. Ivanov, Jagjit Nanda, Andrei Piryatinski, Marc Achermann, Laurent P. Balet, Ilia V. Bezel, Polina O. Anikeeva, Sergei Tretiak, and Victor I. Klimov. Light amplification using inverted core/shell nanocrystals: towards lasing in the single-exciton regime. *The Journal of Physical Chemistry B*, 108(30):10625–10630, 2004. doi: 10.1021/jp0483371. URL `http://pubs.acs.org/doi/abs/10.1021/jp0483371`.

[92] J. Nanda, S. A. Ivanov, H. Htoon, I. Bezel, A. Piryatinski, S. Tretiak, and V. I. Klimov. Absorption cross sections and auger recombination lifetimes in inverted core-shell nanocrystals: Implications for lasing performance. *Journal*

of Applied Physics, 99(3):034309, 2006. doi: 10.1063/1.2168032. URL http://link.aip.org/link/?JAP/99/034309/1.

[93] Michele Saba, Stefan Minniberger, Francesco Quochi, Juergen Roither, Marco Marceddu, Agnieszka Gocalinska, Maksym V. Kovalenko, Dmitri V. Talapin, Wolfgang Heiss, Andrea Mura, and Giovanni Bongiovanni. Excitonexciton interaction and optical gain in colloidal cdse/cds dot/rod nanocrystals. *Advanced Materials*, 21(48):4942–4946, 2009. ISSN 1521-4095. doi: 10.1002/adma.200901482. URL http://dx.doi.org/10.1002/adma.200901482.

[94] H. Htoon, J. a. Hollingworth, a. V. Malko, R. Dickerson, and V. I. Klimov. Light amplification in semiconductor nanocrystals: Quantum rods versus quantum dots. *Appl. Phys. Lett.*, 82(26):4776, 2003. ISSN 00036951. doi: 10.1063/1.1586460. URL http://link.aip.org/link/APPLAB/v82/i26/p4776/s1&Agg=doi.

[95] K. L. Shaklee and R. F. Leheny. DIRECT DETERMINATION OF OPTICAL GAIN IN SEMICONDUCTOR CRYSTALS. *Appl. Phys. Lett.*, 18(11):475–477, 1971.

[96] K. L. Shaklee, R. E. Nahory, and R. F. Leheny. Optical Gain In Semiconductors. *J. Lumin.*, 7:284–309, 1973.

[97] M. Kazes, D. Oron, I. Shweky, and U. Banin. Temperature Dependence of Optical Gain in CdSe/ZnS Quantum Rods. *Journal of Physical Chemistry C*, 111(22):7898–7905, June 2007. ISSN 1932-7447. doi: 10.1021/jp070075q. URL http://pubs.acs.org/cgi-bin/doilookup/?10.1021/jp070075q.

[98] Sangmin Kim, Rajesh Sharma, Bumjin Kim, Ho-Soon Yang, and Kwangseuk Kyhm. Modal gain enhancement by cylindrical waveguide and gain saturation in CdSe nanocrystal quantum dots. *Journal of Physics D: Applied Physics*, 42(9):095403, May 2009. ISSN 0022-3727. doi: 10.1088/0022-3727/42/9/

095403. URL http://stacks.iop.org/0022-3727/42/i=9/a=095403?key=crossref.a5c265ec69f6b7df43f8293318f06f98.

[99] Yinthai Chan, Jonathan S. Steckel, Preston T. Snee, J.-Michel Caruge, Justin M. Hodgkiss, Daniel G. Nocera, and Moungi G. Bawendi. Blue semiconductor nanocrystal laser. *Appl. Phys. Lett.*, 86(7):073102, 2005. ISSN 00036951. doi: 10.1063/1.1863445. URL http://link.aip.org/link/APPLAB/v86/i7/p073102/s1&Agg=doi.

[100] K. Kyhm, R. a. Taylor, J. F. Ryan, T. Someya, and Y. Arakawa. Analysis of gain saturation in In[sub 0.02]Ga[sub 0.98]N/In[sub 0.16]Ga[sub 0.84]N multiple quantum wells. *Appl. Phys. Lett.*, 79(21):3434, 2001. ISSN 00036951. doi: 10.1063/1.1421094. URL http://link.aip.org/link/APPLAB/v79/i21/p3434/s1&Agg=doi.

[101] K Kyhm, R A Taylor, J F Ryan, T Someya, and Y Arakawa. Saturation of gain in In0.02Ga0.98N/In0.16Ga0.84N MQW plasmas. *Physica Status Solidi (B)*, 314:47–51, 2002.

[102] R.a. Taylor, K. Kyhm, J.D. Smith, J.H. Rice, J.F. Ryan, T. Someya, and Y. Arakawa. Dynamics and gain in highly-excited InGaN MQWs. *Current Applied Physics*, 2(4):321–326, August 2002. ISSN 15671739. doi: 10.1016/S1567-1739(02)00118-9. URL http://linkinghub.elsevier.com/retrieve/pii/S1567173902001189.

[103] Rajesh Sharma, Bumjin Kim, Chaeryong Cho, and Kwangseuk Kyhm. Modal optical gain and cavity mode analysis of unstructured and optically structured ZnO nanocrystalline thin films. *Journal of Physics D: Applied Physics*, 42(13):135421, July 2009. ISSN 0022-3727. doi: 10.1088/0022-3727/42/13/135421. URL http://stacks.iop.org/0022-3727/42/i=13/a=135421?key=crossref.ee4ec3c4cc30f3e8e374adf5039a0d42.

[104] Bumjin Kim, Heedae Kim, Sungkyun Park, Kwangseuk Kyhm, and Chaeryong

Cho. Polarization asymmetry and optical modal gain saturation via carrier photon interaction in ZnO. *Appl. Phys. Lett.*, 97:041115, 2010. doi: 10.1063/1.3473729.

[105] Jihoon Kim, Jaebeom Lee, and Kwangseuk Kyhm. Surface-plasmon-assisted modal gain enhancement in Au-hybrid CdSe / ZnS nanocrystal quantum dots. *Appl. Phys. Lett.*, 99:213112, 2011. doi: 10.1063/1.3664114.

[106] Kerry J Vahala. Optical microcavities. *Nature*, 424(6950):839–846, August 2003. ISSN 1476-4687. doi: 10.1038/nature01939. URL http://www.pubmedcentral.nih.gov/articlerender.fcgi?artid=3076881&tool=pmcentrez&rendertype=abstract.

[107] Ahmer Naweed, G. Farca, S. I. Shopova, and A. T. Rosenberger. Induced transparency and absorption in coupled whispering-gallery microresonators. *Phys. Rev. A*, 71:043804, Apr 2005. doi: 10.1103/PhysRevA.71.043804. URL http://link.aps.org/doi/10.1103/PhysRevA.71.043804.

[108] Qianfan Xu, Sunil Sandhu, Michelle L. Povinelli, Jagat Shakya, Shanhui Fan, and Michal Lipson. Experimental realization of an on-chip all-optical analogue to electromagnetically induced transparency. *Phys. Rev. Lett.*, 96:123901, Mar 2006. doi: 10.1103/PhysRevLett.96.123901. URL http://link.aps.org/doi/10.1103/PhysRevLett.96.123901.

[109] Kouki Totsuka, Norihiko Kobayashi, and Makoto Tomita. Slow light in coupled-resonator-induced transparency. *Phys. Rev. Lett.*, 98:213904, May 2007. doi: 10.1103/PhysRevLett.98.213904. URL http://link.aps.org/doi/10.1103/PhysRevLett.98.213904.

[110] S. Preu, H. G. L. Schwefel, S. Malzer, G. H. Döhler, L. J. Wang, M. Hanson, J. D. Zimmerman, and A. C. Gossard. Coupled whispering gallery moderesonators in the terahertz frequency range. *Opt. Express*, 16(10):7336–7343, May

2008. doi: 10.1364/OE.16.007336. URL http://www.opticsexpress.org/abstract.cfm?URI=oe-16-10-7336.

[111] S. Darmawan, L. Y. M. Tobing, and D. H. Zhang. Experimental demonstration of coupled-resonator-induced-transparency in silicon-on-insulator based ring-bus-ring geometry. *Opt. Express*, 19(18):17813–17819, Aug 2011. doi: 10.1364/OE.19.017813. URL http://www.opticsexpress.org/abstract.cfm?URI=oe-19-18-17813.

[112] K.-J. Boller, A. Imamolu, and S. E. Harris. Observation of electromagnetically induced transparency. *Phys. Rev. Lett.*, 66:2593–2596, May 1991. doi: 10.1103/PhysRevLett.66.2593. URL http://link.aps.org/doi/10.1103/PhysRevLett.66.2593.

[113] D. M. Beggs, M. A. Kaliteevski, S. Brand, and R. A. Abram. Optimization of an optical filter with a square-shaped passband based on coupled microcavities. *Journal of Modern Optics*, 51(3):437–446, 2004. doi: 10.1080/09500340408235535. URL http://www.tandfonline.com/doi/abs/10.1080/09500340408235535.

[114] Sheng Lan, Satoshi Nishikawa, Yoshimasa Sugimoto, Naoki Ikeda, Kiyoshi Asakawa, and Hiroshi Ishikawa. Analysis of defect coupling in one- and two-dimensional photonic crystals. *Phys. Rev. B*, 65:165208, Apr 2002. doi: 10.1103/PhysRevB.65.165208. URL http://link.aps.org/doi/10.1103/PhysRevB.65.165208.

[115] D. W. L. Sprung, L. W. A. Vanderspek, W. van Dijk, J. Martorell, and C. Pacher. Biperiodic superlattices and the transparent state. *Phys. Rev. B*, 77:035333, Jan 2008. doi: 10.1103/PhysRevB.77.035333. URL http://link.aps.org/doi/10.1103/PhysRevB.77.035333.

[116] A. W. Castleman and K. H. Bowen. Clusters: structure, energetics, and dynamics of intermediate states of matter. *The Journal of Physical Chemistry*,

100(31):12911–12944, 1996. doi: 10.1021/jp961030k. URL http://pubs.acs.org/doi/abs/10.1021/jp961030k.

[117] Z. Adam Peng and Xiaogang Peng. Nearly monodisperse and shape-controlled cdse nanocrystals via alternative routes: nucleation and growth. *Journal of the American Chemical Society*, 124(13):3343–3353, 2002. doi: 10.1021/ja0173167. URL http://pubs.acs.org/doi/abs/10.1021/ja0173167.

[118] C. Diederichs, J. Tignon, C. Dasbach, G. Ciuti, A. Lemaitre, J. Bloch, Ph. Roussignol, and C. Delalande. Parametric oscillation in vertical triple microcavities. *Nature*, 440(7086):904–907. URL http://dx.doi.org/10.1038/nature04602.